Charge Carrier Dynamics in Lead Sulfide Quantum Dot Solids

by

Rachel Hoffman Gilmore

Bachelor of Chemical Engineering
Cornell University, 2011

Master of Science in Chemical Engineering Practice
Massachusetts Institute of Technology, 2013

Submitted to the Department of Chemical Engineering in Partial Fulfillment of the Requirements for the Degree of

Doctor of Philosophy in Chemical Engineering

at the
Massachusetts Institute of Technology

February 2018 [September 2017]

© 2018 Massachusetts Institute of Technology. All rights reserved.

Signature of Author: Signature redacted
Department of Chemical Engineering
August 29th, 2017

Certified by: Signature redacted
William A. Tisdale
Charles and Hilda Roddey Career Development Professor in Chemical Engineering
Thesis Supervisor

Accepted by: Signature redacted
Patrick Doyle
Robert T. Haslam (1911) Professor of Chemical Engineering
Chairman, Committee for Graduate Students

ARCHIVES
MASSACHUSETTS INSTITUTE OF TECHNOLOGY
DEC 13 2017
LIBRARIES

Charge Carrier Dynamics in Lead Sulfide Quantum Dot Solids

by

Rachel Hoffman Gilmore

Submitted to the Department of Chemical Engineering on August 29th, 2017 in partial fulfillment of the requirements for the degree of Doctor of Philosophy in Chemical Engineering

Abstract

Quantum dots, also called semiconductor nanocrystals, are an interesting class of materials because their band gap is a function of the quantum dot size. Their optical properties are not determined solely by the atomic composition, but may be engineered. Advances in quantum dot synthesis have enabled control of the ensemble size dispersity and the creation of monodisperse quantum dot ensembles with size variations of less than one atomic layer. Quantum dots have been used in a variety of applications including solar cells, light-emitting diodes, photodetectors, and thermoelectrics. In many of these applications, understanding charge transport in quantum dot solids is crucial to optimizing efficient devices. We examine charge transport in monodisperse, coupled quantum dot solids using spectroscopic techniques explained by hopping transport models that provide a complementary picture to device measurements.

In our monodisperse quantum dot solids, the site-to-site energetic disorder that comes from size dispersity and the size-dependent band gap is very small and spatial disorder in the quantum dot superlattice often has a greater impact on charge transport. In Chapter 2, we show that improved structural order from self-assembly in monodisperse quantum dots reduces the interparticle spacing and has a greater impact than reduced energetic disorder on increasing charge carrier hopping rates. In Chapter 3, we present temperature-dependent transport measurements that demonstrate again that when energetic disorder is very low, structural changes will dominate the dynamics. We find increasing mobility with decreasing temperature that can be explained by a 1-2 Å contraction in the edge-to-edge nearest neighbor quantum dot spacing. In Chapter 4, we study optical states that are 100-200 meV lower in energy than the band gap. Because we work with monodisperse quantum dots, we are able to resolve this trap state separately from the band edge state and study its optical properties. We identify the trap state as dimers that form during synthesis and ligand exchange when two bare quantum dot surfaces fuse. The findings of this thesis point to the importance of minimizing the structural disorder of the coupled quantum dot solid in addition to the energetic disorder to optimize charge carrier transport.

Thesis Supervisor: William A. Tisdale
Title: Associate Professor of Chemical Engineering

Acknowledgements

There are many people I would like to thank for their contributions this thesis and my time in graduate school at MIT. First, I would like to thank the National Science Foundation Graduate Research Fellowship Program and the Department of Energy for funding my graduate studies. I would also like to acknowledge the Center for Functional Nanomaterials at Brookhaven National Laboratory where I collected a large fraction of the experimental data presented in this thesis.

I would not have come to graduate school without the support and encouragement of my professors at Cornell University, particularly Professors T. Michael Duncan, Susan Daniel, and Tobias Hanrath. I would also like to thank the graduate student I worked with during my undergraduate research, Joshua Choi, and the rest of the Hanrath Lab for making undergraduate research such a great experience that I wanted to continue in graduate school.

I am extremely grateful to my thesis advisor, Will. I have been privileged to be part of founding this welcoming, fun-loving, and supportive group while doing great science, and I cannot thank Will enough for creating this atmosphere. Will has been a source of boundless enthusiasm and optimism and it has been a real pleasure to be able to work with him.

I would like thank my thesis committee members, Moungi Bawendi and Bill Green for their advice and input throughout my PhD. It has been extremely helpful to have the perspective of Moungi's decades of experience in the quantum dot field, and I am consistently impressed by Bill's insightful questions.

I would like to thank my many collaborators. First, endless thanks for Matt Sfeir at the Center for Functional Nanomaterials at Brookhaven National Lab. A majority of the experimental work in this thesis was conducted in his optics lab, and this would not have been possible without his time and dedication and willingness to help me set up any and all experiments I needed. I would like to thank Adam Willard for his advice and input on theoretical simulations and model to explain my spectroscopy data and for granting me access to his computer cluster to run kinetic Monte Carlo simulations. I would also like to thank Yun Liu, Huashan Li, and Jeff Grossman for collaborating on atomistic calculations of the energy structure of QD dimers. I am grateful to Detlef Smilgies at the Cornell High Energy Synchrotron Source and Kevin Yager at the National Synchrotron Light Source II at Brookhaven National Lab for collecting GISAXS measurements to complement my transport measurements, sometimes at very short notice.

I would like to extend a big thank you to the members of the Tisdale Lab. In particular, thank you to Liza Lee for collaborating with me on kinetic Monte Carlo and Pauli maser equation simulations to fit my experimental work. I am thankful for her endless patience in explaining the theory and simulation techniques to me and I learned so much from her in this process. This thesis would not have been possible without the excellent work done by Mark Weidman, developing the PbS QD synthesis and making all the QDs I used in my thesis, as well as conducting extensive studies of superlattice formation and ordering that informed the interpretation of my transport measurements. Thanks to Matt Ashner for being my laser lab buddy, building the transient absorption setup in our lab, and helping collect data on my PbS QDs. I greatly appreciate the many hours Nabeel Dahod spent searching for the needle in a haystack that is HR-TEM of QD dimers as well as his other TEM and synthetic work to support my thesis. I would also like to thank Wenbi Wu for helping to collect and analyze data this summer as I worked to wrap up my thesis and I am excited for her to build on some of my work in her thesis. I am grateful to Sam Winslow for analyzing GISAXS data this summer to complement my temperature-dependent transport measurements on a very short timeline this summer. I would like extend my thanks to all the other members of the Tisdale Lab for creating such a great working environment – Ferry, Jolene, Aaron, Lisa, Pooja, Yunan, Dan, Oat, SK, Kris, Katie, Robert, Michael, Leo, Deepankur, and Barb.

I want to thank the friends with whom I went through the ups and downs of the ChemE first year classes and Practice School – Lea, Rosanna, Renee, Aanchal, Adam, Kendele, Katie, Ray, Ben, Sakul, Mariah, Anashuya, Yuqing, and Lucas. I am also grateful for the friends from the Bulovic lab that I met in the solid state physics course I took second semester – Joel, Farnaz and Wendi – as well as those in the Bawendi lab – Justin, Michel, Lea, and Igor. I would also like to thank Libby Mahaffy, Jean Belbin, Suzanne Maguire, Joel Dashnaw, Sydney Greenley-Kois, Sharece Corner, Eileen Demarkles, and Suzanne Ronkin for their encouragement and support during my graduate studies.

The MIT Science Policy Initiative has been an important part of my graduate experience over the past three years. I thank Bill Bonvillian and Kate Stoll at the MIT Washington Office for all their time and effort to support our many programs. I am very grateful to the many members of the MIT administration who financially support SPI and encourage us as we develop our programming including Deans Waitz, Sipser, Ortiz, and Staton, and VP of Research Zuber. I also want to express my thanks to the other members of the SPI Exec boards with whom I had the opportunity and pleasure of working as well as the many friends I have made through SPI – Lisa, Abigail, Shelby, Jack, Peter, Angela, Lilia, Georgia, Kenny, Jen, Eli, Max, Daniel, Alec, Sarah, Hannah, Scott, Daniel and many others. I cannot wait to see what the new leadership has in store for the upcoming year.

I also thank my high school friends, Izzy and Jennie, and college friends, Andrea and Dayna, for their encouragement, advice, and friendship throughout graduate school.

I am grateful to my Mom and Dad for their support and encouragement to pursue this path and keep persisting even when I had doubts, and to my sister and brother, Abby and Henry, for being there for me and believing in me.

Finally, I would like to thank my wonderful husband and best friend, Daniel, for his support, encouragement, and unshakeable faith in my ability to achieve anything I set my mind to. I appreciate all the times he has cooked me dinner and cleaned the apartment so I could work to complete this thesis. He has kept me grounded and motivated, and for him I am forever grateful.

Table of Contents

Abstract 3

Acknowledgements 5

Table of Contents 9

List of Figures 11

List of Tables 19

Chapter 1 Introduction 21

1.1 Nanocrystal Quantum Dots 21

1.2 Lead Sulfide Quantum Dot Synthesis 22

1.3 Quantum Dot Electronic Structure 23

1.4 QD Solids: Self-assembly and Ligand Exchange 25

1.5 Transport in Quantum Dot Solids 26

1.5.1 Excitons versus free carriers 26

1.5.2 Charge carrier hopping mechanisms 26

1.5.3 Temperature dependence of charge carrier hopping 27

1.5.4 Experimental transport measurement techniques 28

1.5.5 Charge carrier delocalization and band-like transport 29

1.5.6 Trap states 30

1.6 Transient Absorption Spectroscopy 31

1.7 Thesis Overview 36

Chapter 2 Charge Carrier Hopping Dynamics in PbS Quantum Dot Solids of Varying Size and Size Dispersity 37

2.1 Introduction 37

2.2 Fabricate Samples of Varying Size and Size Dispersity 38

2.3 Transient Absorption of Coupled QD Solids 40

2.4 Kinetic Monte Carlo Model to Fit Dynamics 41

2.5 Single QD Linewidth 44

2.6 Impact of Size Dispersity on Transport 49

2.7 Size-dependent Hopping Rate 52

2.8 Conclusions 54
2.9 Experimental Methods 55
2.10 Appendix A: Fitting Absorption Spectra to Determine Peak and Linewidth 57
2.11 Appendix B: Experimental Data for All QD Sizes 58
2.12 Appendix C: Comments on Energetic Alignment in the KMC model 60
2.13 Appendix D: Discussion of Assumptions about the Superlattice Structure 63
Chapter 3 Temperature-Dependent Charge Transport 67
3.1 Introduction 67
3.2 Temperature-Dependent Transient Absorption 67
3.3 Pauli Master Equation Approach to Data Fitting 70
3.4 Temperature-Dependent Hopping Rates Based on Previous Model 71
3.5 Global Fitting Model Predicts Superlattice Contraction 74
3.6 GISAXS Reveals Superlattice Distortion with Decreasing Temperature 76
3.7 Increasing Mobility with Decreasing Temperature 78
3.8 Conclusions 80
3.9 Experimental Methods 80
3.10 Appendix A: Effect of QD shape on minimum center-to-edge distance. 82
3.11 Appendix B: Lattice Distortion from GISAXS 83
Chapter 4 Origin of Trap States 85
4.1 Introduction 85
4.2 Photoluminescence from Band Edge and Trap States 86
4.3 Transient Absorption Directly Excites Trap States and Monitors De-trapping. 87
4.4 Trap State Dynamics are Similar to that of Large QDs 90
4.5 Trap States are QD Dimers 91
4.6 Expected Electronic Structure of a QD Dimer 95
4.7 Comparison to Trap State Literature 97
4.8 Conclusions 100
4.9 Experimental Methods 100
Chapter 5 Outlook 103
References 105

List of Figures

Figure 1.1. The ruby red and yellow colors in stained glass windows, such as those in the iconic north rose window of Notre-Dame de Paris pictured here, are a result of gold and silver nanoparticles in the glass. 21

Figure 1.2. Schematic showing the size-dependent band structure. 24

Figure 1.3. Absorption spectrum of PbS QDs in tetrachloroethylene. 25

Figure 1.4. Normalized photoluminescence intensity as a function of temperature. PL is low near room temperature when excitons rapidly dissociate, and high at low temperatures when charge carriers remain as excitons. 26

Figure 1.5. Schematic of a transient absorption experiment. 32

Figure 1.6. (a-c) Schematics of possible TA signals. (d) Sample TA spectrum of 5.8 nm PbS QDs in tetrachloroethylene showing typical features for a QD with an exciton in the band edge state. 32

Figure 1.7. Transient absorption signatures of hot electron relaxation in 5.8 nm QDs in tetrachloroethylene. (a) 2D colorplot showing spectral changes as a function of time. (b) TA spectra at selected time delays. 33

Figure 1.8. Photoluminescence and transient absorption lifetimes from PbS QDs in tetrachloroethylene. 34

Figure 1.9. Transient absorption signatures of Auger recombination and calculation of the absorption cross section. (a) Increasing the pump fluence increases the number of absorbed photons per QD. Excitons on QDs with more than 1 exciton undergo Auger recombination, reducing the TA bleach signal in a few hundred picoseconds. (b-c) The absorption cross section can be estimated from a plot of the bleach intensity at 1 ns, after Auger recombination is complete but before appreciable single exciton recombination, versus the excitation fluence. This is shown for 5.8 nm QDs in (b) and 4.9 nm QDs in (c). 35

Figure 2.1. Tuning size dispersity in PbS quantum dot solids. (a) Solution phase absorption (solid lines) and emission (dashed lines) spectra for the ten PbS quantum dot batches used in this study. (b) Ensemble absorption linewidth (standard deviation) as a function of first absorption peak energy, with small QDs with $\delta \lesssim 5\%$ in blue, large QDs with $\delta \lesssim 4\%$ in orange and large QDs with $\delta \lesssim 3.3\%$ in red. The dashed lines show the calculated size dispersity of the ensemble assuming a delta function homogeneous linewidth. (c) HR-SEM image of a PbS QD solid (~100 nm thick, 0.92 eV absorption peak, $d = 5.8$ nm, $\delta < 4.1\%$) at ambient temperature following ethanethiol ligand exchange. (d) Grazing incidence small angle X-ray scattering (GISAXS) pattern of a similar film (1.17 eV absorption peak, $d = 4.9$ nm, $\delta < 3.5\%$), showing some retention of body-centered cubic (BCC) ordering following ligand exchange. 38

Figure 2.2. Absorption spectra of quantum dot solids with ethanethiol ligands. The colors are consistent with those in Figure 2.1a.......... 39

Figure 2.3. Transient absorption tracks the average energy of QDs containing excited charge carriers. (a, b) TA data collected from ethanethiol treated solids made from PbS QDs with $\delta < 5.4\%$ (a) and $\delta < 3.5\%$ (b). Solid white lines are the ground state linear absorption spectra. Dashed lines show the TA bleach peak position as a function of time. (c, d) Spectral slices at selected times showing the redshift of bleach peak in the $\delta < 5.4\%$ sample (c) but not in the $\delta < 3.5\%$ sample (d). Dots represent data and lines show Gaussian fits to the peaks. (e, f) Bleach peak energy as a function of time for the $\delta < 5.4\%$ (e) and $\delta < 3.5\%$ (f) samples.......... 41

Figure 2.4. Kinetic Monte Carlo fits to transient absorption data. (a) KMC fit for a representative solid of small quantum dots with $\delta \lesssim 5\%$ (same sample as shown in Figure 2.3a). (b) KMC fit for a representative QD solid with $\delta \lesssim 3.3\%$ (same sample as shown in Figure 2.3b). (c) KMC fit for a representative QD solid with $\delta \lesssim 4\%$. Colored points are the data (same colors as Figure 2.1a), and black lines are the KMC fits with the gray shaded area showing one standard deviation error in the fitting parameters. 44

Figure 2.5. Fundamental parameters extracted from KMC fitting. (a) Inhomogeneous linewidths (standard deviation) of the ten PbS QD samples as found from the fitted energy redshift in the KMC simulations. (b) Homogeneous linewidth (standard deviation) for the absorption (circles) and emission (points) spectra, calculated from the ensemble linewidth and the fitted inhomogeneous linewidth. The solid (absorption) and dashed (emission) lines show the $1/R^2$ scaling expected for homogeneous broadening dominated by deformation-potential coupling to acoustic phonons.[128] (c) Characteristic hopping time, defined as the inverse hopping rate pre-factor adjusted for the number of nearest neighbors in the lattice. Symbol colors are consistent with Figure 2.1b.......... 46

Figure 2.6. Kinetic Monte Carlo fits for the small samples with size dispersity $\delta \lesssim 5\%$ with two time constants representing different hopping rates for electrons and holes.......... 48

Figure 2.7. Grazing-incidence small-angle (left) and wide-angle (right) X-ray scattering (GISAXS and GIWAXS) patterns for quantum dot solids with $\delta < 3.5\%$ (top) and $\delta < 4.9\%$ (bottom) with native oleic acid ligands. The $\delta < 3.5\%$ solid shows a highly ordered superlattice with individual QDs all oriented in the same way with the atomic planes aligned. In contrast, the $\delta < 4.9\%$ sample shows much less order, both for the superlattice and the individual QD orientation. The poorer self-assembly in the $\delta < 4.9\%$ solid results in an average edge-to-edge QD spacing of 3.1 nm, which is 0.8 nm larger than that of the $\delta < 3.5\%$ sample (a 35% increase). 50

Figure 2.8. Intrinsic charge carrier hopping rates as a function of center-to-center QD spacing (a) Hopping times from Figure 2.5 plotted vs center-to-center QD spacing, rather than QD diameter. (b) The hopping rate decreases with increasing center-to-center spacing. Dashed line shows an exponential fit. (c) Even after accounting for a greater distance travelled per hop, mobility and diffusivity decrease with increasing center-to-center QD spacing. Dashed line shows $d_{cc}^{-4.9}$ fit. 51

Figure 2.9. (a) The percentage of the hopping time that is attributed to energetic disorder, as given by $(1/k_{tot}-1/8k')/(1/k_{tot})$. (b) Calculated intrinsic charge carrier mobility and diffusivity as a function of QD size. 52

Figure 2.10. Schematic showing a homogeneously broadened QD solid with an inhomoeneous linewidth much less than both the single QD (homogeneous) linewidth and the available thermal energy at room temperature. 52

Figure 2.11. (a) Mean squared displacement as a function of time from the KMC simulation. The dashed line shows an example of a linear fit at long times to get the diffusivity from the KMC simulation. (b) Simulated charge carrier diffusion length as a function of carrier lifetime 53

Figure 2.12. Fitting absorption spectra to determine peak energy and linewidth. (a) Sample fit (black solid line) to absorption spectrum (purple) with E^4 Rayleigh scattering and three Gaussian peaks for the defined features (dotted lines, band edge peak in gray). (b) Sample absorption spectra fits for monodisperse (top) and polydisperse (bottom) samples near the first absorption peak, showing the fitted peak position in dark gray. (c) Comparison of the absorption linewidth for the fit (open circles) to that determined by measuring the half-width at half-maximum (HWHM, triangles) on the low energy side of the peak. (d) Comparison of the calculated homogeneous linewidth for the absorption spectra fits (open circles), absorption spectra HWHM (triangles), and PL (closed circles). 57

Figure 2.13. (a-j) GISAXS data for all samples, labelled with the center-to-center spacing, d_{cc}, QD diameter, d, and size dispersity, δ. Because QDs are actually faceted, not spherical, very close packing with aligned crystal facets can result in $d_{cc} < d$.[136] (k) Azimuthally integrated GISAXS intensity. (l) Center-to-center spacing, with dashed line showing expected spacing based on sizing curve and 0.5 nm edge-to-edge spacing for ethanethiol.[50] 58

Figure 2.14. (a-j) Transient absorption data for all samples with peak bleach (dashed) and linear absorption spectrum (solid line). Border colors are the same as the spectra in (k). 59

Figure 2.15. (a-j) Kinetic Monte Carlo fits (solid lines) for all samples assuming symmetric conduction and valence bands, with error bounds (shaded gray) and data points shown in same colors as in the solution absorption (solid) and photoluminescence (dashed) spectra in (k) 61

Figure 2.16. (a-j) Kinetic Monte Carlo fits (solid lines) assuming all energetic variation is in one band (could be either conduction band or valence band) for all samples, with error bounds (shaded gray) and data points shown in same colors as in the solution absorption (solid) and photoluminescence (dashed) spectra in (k). 62

Figure 2.17. The equivalent of Figure 2.5 for fundamental parameters extracted from KMC simulations assuming all energetic variation in one band (conduction or valence band). (a) Inhomogeneous linewidths (standard deviation) of the ten PbS QD samples as found from the fitted energy redshift in the KMC simulations. (b) Homogeneous linewidth (standard deviation) for the absorption (circles) and emission (points) spectra, calculated from the ensemble linewidth and the fitted inhomogeneous linewidth. The solid (absorption) and dashed (emission) lines show the $1/R^2$ scaling expected for homogeneous broadening dominated by deformation-potential coupling to acoustic phonons. (c) Characteristic hopping time, defined as the inverse hopping rate pre-factor adjusted for the number of nearest neighbors in the lattice. 63

Figure 2.18. (a) KMC simulation with a BCC lattice considering hopping to the 8 nearest neighbors only (black), and with a distance-dependent hopping rate, allowing hopping as far as 10 times the nearest neighbor distance (green). (b) Comparison of KMC simulation with BCC (black) and FCC (blue) lattices. Dashed lines give the standard deviation of 10 simulations. (c) Comparison of KMC simulation with BCC (black) and disordered (red) lattices. A tunneling constant of $\beta = 1$ Å is used to calculate the tunneling rate as a function of edge-to-edge spacing for the disordered lattice.[64] Dashed lines give the standard deviation of 10 simulations. (inset) Zoom in on the fit in the first 140 ps. (d) Distribution of center-to-center spacing for the BCC lattice and the disordered lattice that is derived from a BCC lattice. 65

Figure 3.1. Transient absorption peak bleach redshifts for as a function of sample temperatures. (a) Linear absorbance spectra of the three QD ensembles used in this study. (b) Transient absorption color plot for 4.2 nm QDs at 300 K (c) Bleach peak energy as a function of time for several temperatures (labeled on graph) for the 5.0 nm QDs. (d) The data in panel (c) plotted as a change in peak energy relative to the energy at zero delay time. The colors used for each temperature are consistent with panel (c). 68

Figure 3.2. Transient absorption peak bleach redshifts for 4.2 nm (a) and 5.8 nm (b) QDs as a function of temperature. The data in panel (b) is plotted as a change in peak energy relative to the energy at zero delay time in (c). The colors used for each temperature are consistent across the panels. 69

Figure 3.3. Linear absorption spectra as a function of temperature for 4.2 nm and 4.9 nm QDs. 69

Figure 3.4. Fits based on model from Chapter 2. (a) Normalized photoluminescence intensity is used to estimate the fraction of dissociated excitons as a function of temperature. (b-d) Model fit to data at each temperature for the 4.2 nm (b) 5.0 nm (c), and 5.8 nm (d) QD solids. The colors used for each temperature are consistent throughout the figure. (e-f) Fitted hopping rates as a function of temperature for the 5.0 nm QD solids. 73

Figure 3.5. Fits with the global hopping model for the 4.2nm (a), 5.0 nm (b), and 5.8 nm (c) QD solids. (d) Predicted change in edge to edge spacing based on the model. (e-j) Fitted hopping rate prefactors (open symbols) and per QD pair total hopping rates (closed symbols) for the 4.2 nm (e-f), 5.0 nm (g-h), and 5.8 nm (i-j) QDs. 75

Figure 3.6. The effect of QD shape on the relevant QD diameter for charge transfer................. 76

Figure 3.7. Temperature-dependent lattice distortion of an ordered superlattice of 5.7 nm QDs with oleic acid ligands. (a) GISAXS patterns at 298 K showing a face-centered cubic lattice and (b) 133 K showing a body-centered tetragonal lattice. (c) Change in neighbor center-to-center spacings with temperature for *a* and *b* axes (black, open circles), *c* axis (blue, open squares), d_{110} direction (red, open triangles), and nearest neighbors (purple crosses). (d, e) Schematics showing the superlattice distortion as a function of temperature with FCC unit cell (blue) and BCT unit cell (red). 77

Figure 3.8. Temperature-dependent lattice distortion of an ordered superlattice of 5.0 nm QDs with ethanethiol ligands. (a) GISAXS patterns at 298 K with expected FCC diffraction peak positions and (b) 160 K with expected BCT peak positions based on the lattice distortion model described in the text. (c) Change in neighbor center-to-center spacings with temperature for *a* and *b* axes (black, open circles), *c* axis (blue, open squares), d_{110} direction (red, open triangles), and nearest neighbors (purple crosses). 78

Figure 3.9. Calculated mobility from KMC simulations based on the global hopping model fit for the fast (a) and slow (b) hopping rates........ 78

Figure 4.1. Emission from band edge and trap states in ethanethiol-treated PbS QD solids. (a) Photoluminescence spectra as a function of temperature showing PL from the band edge state at room temperature and from the trap state at lower temperatures. (b) Schematic showing much higher density of states at the band edge than at the trap state energy, so that at room temperature, charge carriers are thermalized into the band edge states. (c) Ratio of band edge to trap state PL as a function of temperature (filled circles). A fit (dashed line) gives the energetic barrier between QDs and the density of trap states........ 86

Figure 4.2. Excite trap states in PbS QD solids and observe de-trapping in coupled films. (a) Schematic showing population of the trap state followed by upconversion to the band edge state. (b-f) Color plots showing excitation of the mid-gap trap state QD solids ($d = 4.2$ nm, $\delta = 2.1$-3.0%) with varying ligand lengths. The pump spectra and QD solution absorption spectra are shown overlaid for reference. (g) Spectra at early and late times for the ethanethiol treated solid (b), with peak position and fwhm for the trap state and band edge peaks. (h) Integrated peak intensities as a function of delay time for the ethanethiol treated solid (b). (i-j) Color plots showing dynamics following mixed excitation of the trap and band edge state. (k-l) Excitation of the mid-gap state and band edge state in larger, monodisperse QD solids ($d = 4.9$ nm, $\delta = 0.6$-0.8%). 87

Figure 4.3. Transient absorption exciting at the band edge peak for QD solids with thiol ligands of varying lengths. A transient redshift indicating charge transport in the observed time window is present for ethanethiol and butanethiol QD solids, but not for octanethiol, dodecanethiol, or oleic acid. 88

Figure 4.4. Transient absorption spectroscopy showing excitation of the trap state and upconversion to the band edge state in QD solids with ethanethiol ligands. (top row) Color plots repeated from Figure 4.2. (middle row) Spectra at 1 ps and 400 ps for the QD solids in the row above. (bottom row) Population dynamics of the band edge and trap states for the QD solids shown in the top row. 89

Figure 4.5. PbS QDs with mercaptopropionic acid (top row) and tetrabutylamonium iodide (bottom row) ligands also show trap state excitation and upconversion to the band edge state... 89

Figure 4.6. Trap state bleach dynamics. (a) Trap state bleach intensity in QD solid with oleic acid ligands as a function of delay time and excitation power showing dynamics characteristic of Auger recombination. (b) Decay time constant as a function of number of excitons absorbed per QD for the trap state and various sizes of QD band edge states. (c) Bleach intensity at 1ns as a function of excitation fluence with experimental data shown with open circles and a fit to the data to determine the absorption cross section shown with a dashed line. (d) Trap state and band edge bleach dynamics in ethanethiol-treated QD solid excited at the trap state energy with varying excitation powers at 300 K. Fitted time constants are 39 ± 5 ps ($0.8\text{x}10^{15}$ photons/cm^2), 35 ± 3 ps ($1.6\text{x}10^{15}$ photons/cm^2), 34 ± 2 ps ($3.6\text{x}10^{15}$ photons/cm^2), and 520 ± 40 ps (all). The contribution from the fast component increases with increasing fluence. (e) Dynamics at 80 K. (f) Schematic showing proposed de-trapping mechanism. 90

Figure 4.7. (a) TEM micrograph of monodisperse 4.9 nm QDs with oleic acid ligands showing an absence of large QDs, but the presence of a QD dimer. (b) HR-TEM micrograph of a dimer with FFT of the entire dimer and the left and right QD within the dimer, all identical and showing (100) planes oriented to the surface, indicating attachment on the (100) facet. (c) HR-TEM micrograph of a dimer with a twinning boundary at the attachment interface. FFT shows the left side of the dimer has (100) planes oriented to the surface while the right side has (111) planes, but the radially aligned peaks indicate aligned lattice planes across the dimer confirming fused attachment. 92

Figure 4.8. FFT analysis of HR-TEM images. (a) FFT analysis of a monolayer of unattached, randomly oriented QDs shows many FFT spots at different azimuthal positions. (b) FFT analysis for the dimer shown in Figure 4.7 shows two different lattice planes aligned and epitaxially attached. 93

Figure 4.9. Trap state excitation of oleic acid-capped QDs in solution, oleic acid-capped QD solids, and following ligand exchange for ethanethiol. The optical density at the band edge peak absorption was 0.2 for the solution sample, 0.1 for the oleic acid sample, and 0.08 for the EMT sample. Thus, the concentration of trap states seems to be the same in solution and in a QD solid with oleic acid ligands, but is higher for ethanethiol-treated solids, even after accounting for an increase in absorption cross section for the shorter ligands.[47] 94

Figure 4.10. Trap state excitation in QDs synthesized with PbO (a-b) or $PbAc_2$ (c). (b) has a longer wavelength pump pulse than (a) 94

Figure 4.11. Calculated trap state depth for different QD shapes (truncated octahedron, cuboctahedron, truncated cube) and attached facets ((100), (111)) based on effective mass and tight binding approximations.[120, 162] Calculations with a confining potential barrier of 1.0 eV[162] are shown with solid lines and of 1.6 eV[93] with dashed lines. Trap state depth extracted from transient absorption measurements are shown in red circles. 95

Figure 4.12. Sideview of the 2 nm diameter PbS QD. The black and yellow atoms represent Pb and S respectively. The colored boxes represent increasing degree of fusing in the QD dimers, from 4 to 12, 16, and 24 atoms. The fusing occurs along the (100) facet. The absorption spectra and (c) band edge states of fused dimers, compared with single isolated QD. (d) The wavefunction of the conduction band minimum of a single dot, and that of the fused dimer with 12 atoms in the fused plane. Significant localization of the states along the fused region compared to the delocalized states in the QD core for the single dot. 96

Figure 4.13. Sideview of the 2.5 nm diameter PbS QD. The black and yellow atoms represent Pb and S respectively. The colored boxes represent increasing degree of fusing in the QD dimers, from 4 to 12, 16, 24, and 32 atoms. The fusing occurs along the (100) facet. The absorption spectra and (c) band edge states of fused dimers, compared with single isolated QD. 97

Figure 4.14. Temperature-dependent photoluminescence spectra for (a) ethanethiol-treated and (b) benzoquinone and ethanethiol-treated PbS QD solids. Normalized spectra are shown in (b) and (e) respectively. Integrated PL intensity as a function of temperature are shown in (c) and (f). 98

Figure 4.15. Optically exciting the trap states in QD solids with and without benzoquinone treatment. 99

Figure 4.16. Exciting QD solids with and without benzoquinone treatment at the band edge state. 99

List of Tables

Table 2.1. Key parameters from experiment and simulations: fitted absorption peak maximum; fitted total absorption linewidth (standard deviation, σ_{tot}); calculated QD diameter based on our sizing curve (*d*);[20] calculated size dispersity assuming delta-function homogeneous linewidth, expressed as standard deviation of the mean diameter (δ); the fitted hopping time constant, which is the reciprocal of the hopping rate prefactor, $t_{hop} = 1/k'$; fitted inhomogeneous linewidth from TA experiments (σ_{inh}); inferred homogeneous linewidth (σ_{hom} from eq (2.4) using σ_{tot} from column 2 and σ_{inh} from column 6); and the "actual" size dispersity calculated from the fitted inhomogeneous linewidth, σ_{inh}, from the KMC model 45

Chapter 1 Introduction

1.1 Nanocrystal Quantum Dots

The unique optical properties of nanostructured materials have been employed for centuries, since long before their science was understood. For example, the vivid reds and yellows in stained glass windows found in European cathedrals from the 6th to 15th centuries are the result of gold and silver nanoparticles, respectively, that formed when gold chloride or silver nitrate was added during the glass-making process (Figure 1.1).[1]

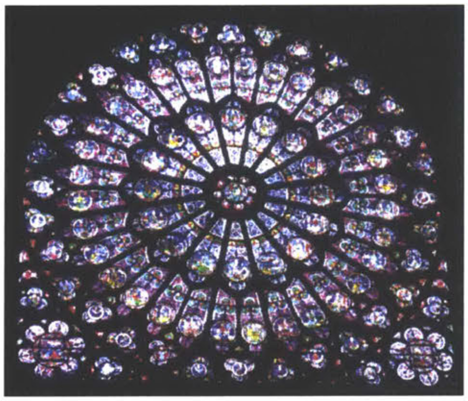

Figure 1.1. The ruby red and yellow colors in stained glass windows, such as those in the iconic north rose window of Notre-Dame de Paris pictured here, are a result of gold and silver nanoparticles in the glass.

The modern era of scientific research into semiconductor quantum dots (QDs), which are also called nanocrystals (NCs), began in 1981 when Alexei Ekimov of the USSR formed and studied the optical properties of semiconductor nanocrystals in a glass matrix.[2-3] A few years later, Louis Brus of Bell Labs synthesized and studied the first colloidal semiconductor QDs.[4-6] In 1993, Moungi Bawendi's new lab at MIT developed the first controlled, scalable synthesis for colloidal QDs, which they demonstrated with nearly monodisperse CdSe QDs.[7]

QDs are clusters of ~1000-10,000 atoms that are ~2-20 nanometers in diameter and exhibit optical properties that have both bulk and atomic character. A defining feature of semiconductor QDs is a size-dependent band gap, which determines what colors of light the QDs will absorb or emit. Synthetic methods have now been developed for a variety of semiconductor QDs, including Cd, Zn, Hg, and Pb chalcogenides (S, Se, Te), InP, InAs, and perovskites.[8-10] It is possible to engineer the shape of QDs[11-14] as well as make a variety of core-shell structures,[15-17] which show near-unity quantum yields. Their optical properties span the near ultra-violet to the mid-wavelength infrared, making different types of QDs attractive materials for a wide variety of applications[18] including display technologies,[19] light-emitting diodes,[20] solar cells,[21] photodetectors,[22] thermoelectrics,[23] biological imaging,[24] telecommunications,[25] thermal imaging sensors.[26] Lead sulfide (PbS) quantum dots are particularly promising for infrared applications because they are air stable and have a band gap that can be tuned across the near infrared (NIR) into the short-wave infrared (SWIR) from ~700nm to 2400nm (1.8eV to 0.5eV).[27-28] PbS QD photodetectors have figures of merit that outperform commercial technologies.[29] They have been used in IR LEDs,[30] and are the absorber in QD solar cells with efficiencies exceeding 11%.[21]

Thus, QDs are a promising designer semiconductor for next-generation optoelectronic devices, in which one can imagine precisely tuning the semiconductor properties to match the desired application. They are very good at absorbing and efficiently emitting narrow spectrum light, so their first commercial applications have been as color filters in display technologies such as televisions and monitors.[19] However, other applications, such as solar cells or LEDs, require better control of the charge carrier transport, and how changing QD properties impacts transport in QD solids.

1.2 Lead Sulfide Quantum Dot Synthesis

Initial colloidal synthesis for PbS QDs was published by Hines and Scholes in 2003,[9] a decade after CdSe QD synthesis was first reported. The synthesis was patterned on previous QD synthesis methods for cadmium chalcogenides[7] and PbSe,[31] using lead oxide in oleic acid (OA) to make lead oleate, and injecting bis(trimethylsilyl)sulfide (TMS) in octadecene (ODE) at elevated temperatures of 80-140°C. Varying the OA:Pb:S ratios and the injection temperature adjusts the kinetics of the nucleation and growth rates to control the QD size. This synthesis has since been adapted to use either lead oleate or lead acetate,[32] and is widely used in a variety of devices.[33-34]

Another hot-injection synthesis method developed by Cademartiri *et al.*,[35] and improved by Moreels *et al.*[36] and Weidman *et al.*[27] uses lead chloride and elemental sulfur precursors in oleylamine, which acts as both the stabilizing ligand and the solvent. This synthesis follows a diffusion-limited growth mechanism, and creates highly monodisperse PbS QDs that are lead-rich with both chlorine ions (from $PbCl_2$) and oleylamine ligands on the surface. Size dispersity, or the variation in QD sizes within an ensemble, determines the total linewidth of the ensemble absorption and emission spectra (inhomogeneous broadening is convolved with homogeneous broadening to give the total linewidth) and the energetic disorder in a QD solid. It is thus a key parameter to optimize in synthesis, with monodisperse QDs (all QDs the same size), rather than polydisperse QDs (a range of QD sizes present), desired for most applications. The oleylamine ligands are weakly bound to the QD surface, and rapidly detach and reattach, in equilibrium with free oleylamine in solution.[36] Following synthesis, the oleylamine ligands are replaced with more strongly bound oleate ligands at a density of about 3 per nm^2 to ensure long-term colloidal stability.[36] The surface chlorine ions are believed to stabilize the QDs, making them air-stable for at least several months.[27] The oleate and chloride ions also ensure charge neutrality of the lead-rich QDs.[36] While this synthesis is very successful for making QDs with band gaps lower in energy than 1.2 eV (1000 nm), it does not make the smallest QDs that are often used in photovoltaics. Zhang *et al.*[37] have adapted this synthesis to use TMS in place of elemental sulfur to extend the size range to these smaller QDs.

Additional synthetic methods to make monodisperse PbS QDs have been developed in recent years. Hendricks *et al.*[38] developed a library of substituted thiourea precursors to precisely tune the nucleation rate kinetics with lead oleate and prepare monodisperse PbS QDs across a range of sizes at nearly full reaction conversion. Taking advantage of the excellent synthetic methods available for CdS and CdSe QDs, Beard and co-workers[39] use a cation exchange process to convert highly monodisperse CdS or CdSe QDs to PbS or PbSe QDs. $PbCl_2$ is used for the cation exchange, so these QDs have the chloride passivation that improves air stability. Larger PbS QDs can be made through the sequential addition of smaller QDs, which dissolve to create additional monomers in solution and grow the size of the original QDs through an Ostwald ripening process.[40]

1.3 Quantum Dot Electronic Structure

The size-dependent band gap in semiconductor QDs arises when the size of the QD approaches and becomes smaller than the characteristic length scale of a charge carrier in the material. The charge carrier can be an electron, hole, or electron-hole pair, which is known as an exciton. The characteristic length scale is given by the Bohr radius:

$$a_B = \varepsilon \frac{m}{m^*} a_0 \tag{1.1}$$

where ε is the dielectric constant of the material, m is the rest mass of an electron, m^* is the effective mass of the charge carrier (electron, hole, or exciton), and a_0 is the Bohr radius of the hydrogen atom. The Bohr radius for the exciton in PbS is ~18 nm, so strong quantum confinement is expected for typical quantum dot sizes (2-12 nm).[41] Additionally, the effective masses of the electron and hole in PbS are small and approximately equal ($m_e^* = 0.12m$, $m_h^* = 0.11m$), so both the electron and hole of dissociated excitons are strongly quantum confined.

To a first approximation, the band gap of a QD can be calculated using the particle-in-a-sphere model,

$$E_g(r) = E_g^{bulk} + \frac{\hbar^2 \pi^2}{2 m_{eh} r^2} \tag{1.2}$$

where E_g is the band gap as a function of the QD radius, r, and m_{eh} is the exciton reduced mass. Because the electron and hole effective masses are approximately equal in lead chalcogenides, the conduction and valence bands are expected to be symmetric in this model. This is in contrast to the well-studied CdSe QDs, which have a heavier hole mass and thus much more closely spaced valence band states than conduction band states. While the band structure for lead chalcogenide (PbS, PbSe) QDs is nearly symmetric, atomistic simulations and experimental measurements suggest the valence band states are more densely populated and shift less with QD size as compared to the conduction band states.[42-44] A schematic of the size-dependent band structure is shown in Figure 1.2.

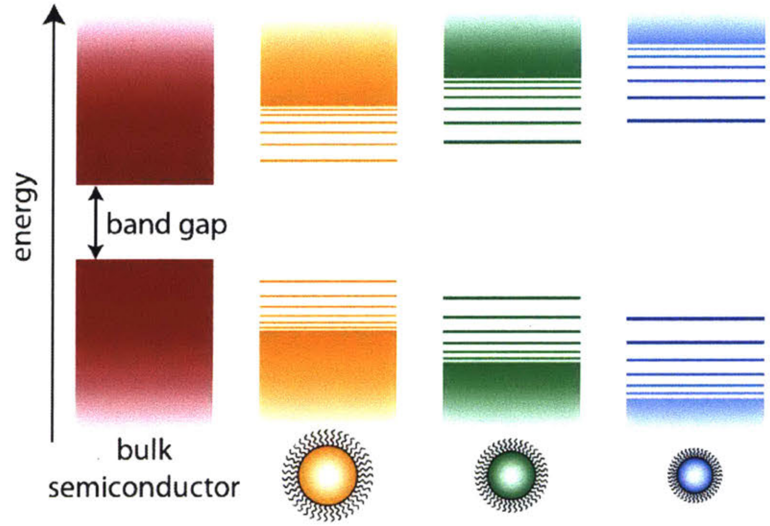

Figure 1.2. Schematic showing the size-dependent band structure.

A typical absorption spectrum for PbS QDs is shown in Figure 1.3. The discrete transitions in a QD are labeled based on analogy to molecular transitions. The lowest energy transition, which is the band gap, is labeled $1S_h$-$1S_e$. The $1S_h$ and $1S_e$ bands are the valence and conduction bands and are 8-fold degenerate, including spin, in PbS QDs. The second large peak is the $1P_h$-$1P_e$ transition.[45] The small peak observed between these two peaks in highly monodisperse QDs is from the spin-forbidden $1S_h$-$1P_e$ and $1P_h$-$1S_e$ transitions.[46] Higher energy transitions have been assigned to $1D_h$-$1D_e$ transitions and other forbidden transitions.[47] The broad peak at ~500-600 nm has been assigned to a high energy saddle point along the Σ direction in the Brillouin zone, which acts as a phonon bottleneck, slowing hot carrier cooling to ~$1 ps^{-1}$ and allowing competing processes such as multi-exciton generation or hot electron transfer to proceed. These excitonic absorption features are sharpest for monodisperse QD ensembles in which the ensemble spectra approach the single QD spectra. In polydisperse ensembles with higher size dispersity, the size-dependent band gap results in QDs with different excitonic energy transitions and blurring of features in the absorption spectrum. By 400 nm, the electronic states are a continuum of bulk-like states,[48] which enable the absorption at 400 nm to be used to accurately measure the QD concentration in mg/mL regardless of the QD size and size dispersity.[49]

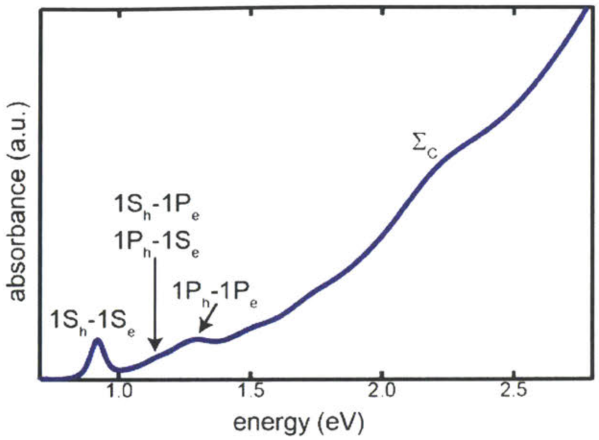

Figure 1.3. Absorption spectrum of PbS QDs in tetrachloroethylene.

1.4 QD Solids: Self-assembly and Ligand Exchange

Several fabrication techniques have been uses to deposit QD solids of varying size and film thickness including drop casting, spin coating, dip coating, spray coating, and assembly at liquid-air interfaces. Many nanomaterials self-assemble into superlattices given sufficient time in a mobile environment such as at a liquid-air interface, but monodisperse PbS QDs self-assemble even in more rapid deposition environments like spin coating.[50] Highly monodisperse PbS QDs even self-assemble into superlattices in which all the PbS crystal planes in each QD are aligned throughout the superlattice.[50-51]

To improve charge carrier transport in QD solids, the long, insulating ligands that provide good colloidal stability during synthesis and storage must be replaced with shorter ligands that reduce the interparticle spacing between QDs. Traditionally, this has been done using a solid-state ligand exchange process in which the spin cast or dip coated solid is immersed in a solution containing the new ligand in a solvent, typically acetonitrile or methanol. Commonly used ligands include short chain organics like 1,2-ethanedithiol (EDT), 1,3-benzenedithiol (BDT), 3-mercaptopropionic acid (MPA), or 1,2-ethanediamine (EDA), or inorganic ions such as atomic halide ions (Br^-, Cl^-, I^-) or thiocyanate (SCN^-) . Ligands with lowest unoccupied molecular orbitals (LUMOs) near the conduction band energy have also been used to improve transport.[52] Additionally, ligands can shift the energy levels of the QD solid relative to vacuum, enabling band alignment engineering when integrating QD solids into devices.[33]

Following ligand exchange, the volume of the QD solid contracts, reducing the long-range order and creating cracks in large area films.[50] To compensate, devices are usually fabricated using a layer-by-layer deposition approach in which subsequent layers fill in the cracks in previous layers, but these solids have reduced long-range order as compared to films made from a single deposition step.[50] To reduce the number of processing steps and improve the superlattice order, solution phase ligand exchanges are being developed by the quantum dot research community.[53]

1.5 Transport in Quantum Dot Solids

1.5.1 Excitons versus free carriers

In studying transport in QD solids, one must consider the nature of the charge carriers. Whether they are excitons or dissociated free electrons and holes is determined by the exciton binding energy and the electronic coupling strength between neighboring QDs. In CdSe QDs, the exciton binding energy is large, ~0.2-1.0 eV, depending on the QD size, so charge carriers are excitons under typical experimental conditions.[54] In PbS and PbSe, the exciton binding energy is weak, and electronic coupling can be strong in QD solids with short ligands. As a result, photogenerated excitons rapidly dissociate into free carriers at room temperature. Rapid exciton dissociation results in low photoluminescence (PL) intensity in these solids because and electron and hole often do not remain on the same QD for a sufficiently long time for radiative recombination to occur. The PL intensity increases as temperature decreases (Figure 1.4), revealing that exciton dissociation is a thermally activated process with an activation energy of ~35-120meV.[55-56] The PL intensity also increases with ligand length, confirming that strong electronic coupling, which results in fast charge carrier tunneling, also assists in exciton dissociation. The ligand length dependence of the PL intensity is consistent with a tunneling barrier height (see Section 1.5.2) of $\beta \sim 1.1 Å^{-1}$, consistent with values determined for similar alkane ligands with electrical mobility measurements.[55] In device measurements, a charge separation interface, such as the interface with the electron acceptor zinc oxide, or an applied electric field can also assist in dissociating photogenerated excitons into free carriers.[56]

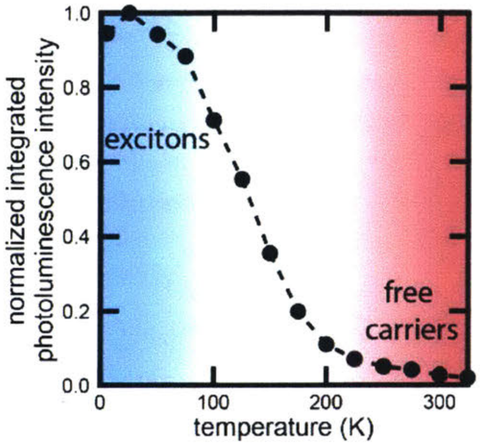

Figure 1.4. Normalized photoluminescence intensity as a function of temperature. PL is low near room temperature when excitons rapidly dissociate, and high at low temperatures when charge carriers remain as excitons.

1.5.2 Charge carrier hopping mechanisms

On the nanoscale, transport in QD solids proceeds *via* charge carrier hopping from QD to QD. If the charge carriers are excitons, the hopping mechanism is Förster resonance energy transfer, which is a non-radiative transfer of excitons though electromagnetic interactions between the transition dipoles of neighboring QDs. The per QD pair energy transfer rate, k_{FRET}, is inversely proportional to the donor lifetime (τ_{d}) and the center-to-center distance between QDs (d_{cc})

$$k_{\mathrm{ET}} = k_{\mathrm{FRET}} = \frac{1}{\tau_d}\left(\frac{R_0}{d_{\mathrm{cc}}}\right)^6 \tag{1.3}$$

where R_0 is the Förster radius and is given by

$$R_0{}^6 = \frac{9\eta_{PL}\kappa^2}{128\pi^5 n^4}\int F_D(\lambda)\sigma_A(\lambda)\lambda^4 d\lambda \tag{1.4}$$

where η_{PL} is the quantum efficiency of the donor, κ^2 is the dipole orientation factor, typically assumed to be 2/3 for randomly oriented dipoles, n is the refractive index, typically assumed to be the volume-weighted sum of the refractive indices of the inorganic cores and organic ligands, $F_{\mathrm{D}}(\lambda)$ is the donor emission spectrum, normalized to an integrated area of 1, and $\sigma_{\mathrm{A}}(\lambda)$ is the acceptor absorption spectrum in units of cross-sectional area. Typical values for the Förster radius are ~8-9 nm in PbS and CdSe QDs.[57-59] Exciton lifetimes in CdSe QDs are ~15 ns, so the time between hops ($1/k_{\mathrm{ET}}$) is ~2-20 ns in CdSe QD solids.[57] In contrast, the lifetime in PbS QDs is ~2 μs, so FRET rates are much slower and the time between hops is hundreds of nanoseconds with native oleic acid ligands, and would be expected to decrease only to several tens of nanoseconds for short ligands.[58]

If charge carriers are free carriers, the hopping mechanism follows electron tunneling, which has an inverse exponential dependence on the edge-to-edge QD spacing (d)

$$k_{\mathrm{ET}} = k_{tunn} \propto e^{-\beta d}. \tag{1.5}$$

The tunneling barrier height, β, is determined by the QD ligand, with typical values of ~2Å^{-1} in vacuum, 0.9-1.2Å^{-1} for conjugated hydrocarbons, 0.2-0.6Å^{-1} for highly conjugated chains.[60] Reported literature values for charge transport via tunneling in PbS and PbSe QD solids have varied widely from sub-picosecond[61] to a several nanoseconds,[62] depending on QD size, ligand treatment, and superlattice structure.

1.5.3 Temperature dependence of charge carrier hopping

A given QD in a QD solid will typically have neighboring QDs with larger and smaller band gaps as a result of size dispersity in the QD ensemble and the size-dependent band gap. Energy must be conserved in charge carrier hopping processes, so hops to higher energy QDs require additional energy which is provided by the environment in the form of thermal energy. Thus, charge carrier hopping is a thermally-activated process and downhill energy hops are more favorable than uphill energy hops. As charge carriers equilibrate in the solid, they approach a Boltzmann distribution convolved with the density of states, regardless of the initial distribution of excited states. So, following excitation of a random subset of QDs in the solid, the average energy of QDs containing charge carriers will shift to lower energy with time, and the magnitude and dynamics of this redshift, which can be monitored using PL or transient absorption spectroscopy,[21] gives information about the size dispersity and hopping rate (FRET for excitons, tunneling for free carriers) in the solid, as will be discussed further in Chapter 2. Even if all QDs are the same size, charge carrier hopping may still be thermally activated because the presence of a charge carrier changes the electronic structure of the QD, reducing the band gap by an amount equal to the charging energy, E_C.

The charge carrier hopping rate is strongly dependent on interparticle spacing, so at room temperature, when thermal energy is readily available, hopping is to nearest neighbors (NNH). As the temperature decreases, longer range hops to more energetically favorable QDs become more likely and transport shifts to variable range hopping (VRH). The relevant transport regime can be determined using the temperature dependence of the conductivity, which takes the form:

$$\sigma = \sigma_0 \exp\left[-\left(\frac{T^*}{T}\right)^z\right]. \tag{1.6}$$

where σ_0 is the conductivity pre-exponential factor, T^* is a fitting parameter with units of Kelvin, and z is a parameter that describes the power of the temperature dependence and can be determined from a log-log plot of $d(\ln\sigma)/d(\ln T)$ versus T. Temperature dependence of $z=1$ is an Arrhenius relation and is consistent with NNH with $T^* = E_A/k_B$. Efros-Shklovskii variable range hopping (ES-VRH), which arises from the soft Coulomb gap in the density of states created by Coulomb interactions between free electrons,[63] is characterized by $z=0.5$. Mott variable range hopping (M-VRH) is relevant at low density of states when electron correlations are not important, and is characterized by $z = 0.25$ for three-dimensional transport or $z = 0.33$ for two-dimensional transport.[64] M-VRH has been observed in electrochemically charged CdSe QDs,[64] and ES-VRH has been observed in both PbSe[65-66] and CdSe[64, 67] QDs. The transition from VRH to NNH occurs when the optimal hopping distance is equal to the center-to-center QD spacing. The transition from ES-VRH to NNH in PbSe QDs occurs at 70-100K, with increasing transition temperature for decreasing QD size.[66]

1.5.4 Experimental transport measurement techniques

Because it is challenging to make direct experimental observations on the nanoscale, macroscale devices and measurements are employed to measure transport properties in QD solids.[68] Field-effect transistors (FETs) have been frequently used to measure mobility in QD solids. In an FET, the gate electrode bias shifts the position of the Fermi energy, which can adjust the carrier concentration and fill mid-gap states. High FET mobilities in excess of 10 $cm^2\ V^{-1}\ s^{-1}$ have been measured in QD solids with inorganic ligands.[52, 69-70] The expected trend of increasing mobility with decreasing ligand length as a result of faster tunneling for shorter inter-particle spacing has been demonstrated through FET measurements.[71] They have also been used to measure the temperature dependence of the mobility to understand charge transport mechanisms.[66] FET measurements have shown either increasing mobility with increasing QD size or non-monotonic trends.[66, 71-72]

While FET devices have many advantages, they measure predominantly electron transport in the accumulation layer at the interface between the QD layer and the gate dielectric and may be impacted by traps at this interface[73] and thus may not reflect the three dimensional QD solid properties. Hall effect measurements can probe the mobility through the film thickness, but they can only be used for high mobility QD solids.[74-75] Time-of-flight photocurrent measurements provide reliable measurements in low-mobility solids, and are transient measurements that are not influenced by long-lived deep trap states.[76]

The time-resolved microwave conductivity technique offers a local probe that measures intrinsic charge carrier mobility.[77] Spectroscopic techniques such as ultrafast transient absorption or photoluminescence also offer a similar complementary view of spectrally resolved charge carrier dynamics in QD solids, and have previously been used to study charge carrier thermalization[18] and diffusion-assisted Auger recombination in quantum dot solids.[7] They can be used to monitor charge carrier dynamics in energetically resolved states on nanometer length scales, and information on charge carrier hopping can be extracted by fitting the data to a transport model.

1.5.5 Charge carrier delocalization and band-like transport

In an ideal QD solid, free from energetic and spatial disorder, strong coupling will result in mixing between the wavefunctions of neighboring QDs, analogous to atomic bonding in bulk crystalline semiconductors. This wavefunction mixing creates continuous energy bands across the QD solid. Delocalized charge carriers may experience band-like transport similar to bulk semiconductors, rather than incoherent site-to-site hopping via tunneling through insulating barriers between QDs. Claims of band-like transport have been made in CdSe[52, 69] and PbSe[78] QD solids with high mobilities of ≥ 1 cm^2 V^{-1} s^{-1}. As evidence, they cite the observation of increased mobility with decreasing temperature ($d\mu/dT < 0$) over some temperature range, rather than the thermally activated behavior expected for a hopping mechanism. However, whether this is sufficient evidence to support the conclusion of band-like transport is the subject of active debate among the community.[68, 79-80] The pre-exponential factor in hopping transport may increase with decreasing temperature. Einstein's relations between mobility and diffusion for a thermally activated hopping process give an expression for the mobility:

$$\mu_{hop} = \frac{ed^2}{6\tau_{hop} k_B T} = \frac{ed^2 E_a}{6hk_B T} e^{-\beta l - E_a/k_B T}, \tag{1.7}$$

where d is the center-to center spacing, E_a is the activation energy, l is the edge-to-edge spacing, and β is the tunneling constant. Thus, for temperatures above $T = E_a/k_B$, hopping transport can result in mobility that increases with decreasing temperature, and additional evidence is required to claim band-like transport.[79]

Band-like or metallic transport occurs in metal nanoparticle solids because of the high density of states near the band edge, but semiconductor QDs have much lower band-edge degeneracy (4-fold in PbS and PbSe, singly degenerate in CdSe, without spin).[79] When the degeneracy is high, as in metal nanoparticles, there are many possible conductance channels, so it does not matter if the transmission through each is relatively low. But for semiconductor QDs, band formation occurs only if the transmission is nearly unity, which requires that the coupling energy between QDs is larger than the energy detuning and the natural linewidths of the band-edge states.[79] This is unlikely in current QD solids because of variations in confinement energy (from size dispersity), disorder in coupling strengths (from variation in edge-to-edge spacing), electron-electron repulsion (charging energy), and thermal broadening. Thus, band-like transport in QD solids is unlikely because of the amount of disorder still present in these materials, and simply showing $d\mu/dT < 0$ over a limited temperature range is not sufficient evidence to prove band-like transport rather than hopping transport.

Additional evidence for the possibility of band-like transport is the formation of charge carriers that are delocalized across many QDs. If substantial mixing between wavefunctions of neighboring QDs is present, the charge carriers will be delocalized across several QDs, or even the whole QD solid in the ideal scenario of band-like transport. Thus, researchers measure the localization length of charge carriers using a variety of techniques. Cross-polarized transient grating spectroscopy of CdSe QDs with In_2Te_3 ligands suggests a localization length of about 2.2 times the QD diameter.[81] Low temperature resistance and magenetoresistance measurements of indium-doped CdSe QD field effect transistors suggested delocalization lengths of several times the QD diameter at high gate voltages.[82] Field effect transistors measurements on epitaxially connected PbSe superlattices also reveal a gate-voltage-dependent localization length of ~2-3 times the QD diameter for electrons and ~1-2 times for holes.[83] Transport in the present epitaxial QD solids follows hopping mechanisms, and reductions in the disorder from QD size dispersity, connectivity (presence of missing connections), and connection width (coupling energy) are needed to increase the localization length and enable band-like transport.[83]

1.5.6 Trap states

Electronic states that exist within the QD band gap are commonly referred to as trap states and have been the subject of substantial discussion in the literature over the past several years.[22, 28, 34, 47, 84-96] In particular, trap states have been identified as a limiting factor to improving PbS QD solar cell efficiencies. Charge carriers are extracted at the lower energy trap states within the band gap, reducing the open-circuit voltage.[93, 97] Additionally, charge carriers diffusing in QD solids become trapped in these low-energy states, which act as recombination centers in the solid, and are not extracted as current from the device. The diffusion length is determined not by the diffusivity and carrier lifetime, but by the distance to the nearest trap state.[93, 98] Thus, the density of trap states is the subject of much interest, and has been measured using a variety of techniques including thermal admittance spectroscopy,[34, 88, 93] field-effect transistor measurements,[85] and photoluminescence measurements,[86] and can vary by orders of magnitude from ~0.01 traps per QD for thiol ligands to as low as ~10^{-4} traps per QD for some halide ligands.[85]

The role of trap states in transport is also the subject of debate, with some authors claiming transport through trap states[96, 99] while others present evidence for trapping and release with transport occurring through band edge states.[87] The nature of trap states in QD solids has also been the subject of substantial study, and multiple types of traps may exist in QD solids. Some authors discuss an exponential tail of trap states near the band edge,[84, 100] while others observe states well below the band edge.[88, 96] Trap states are generally assumed to be surface states because their density changes with different ligand treatments, QD aging, or oxidation.[85-86, 90] Attempts to eliminate trap states typically involve surface treatments such as iodide ligand treatment,[86] capping the PbS QDs with a thin CdS shell[95] or treating the QD solid with oxidizing agents to remove undercharged Pb atoms that may be a source of traps.[94]

1.6 Transient Absorption Spectroscopy

Transient absorption (TA) spectroscopy is a pump-probe spectroscopy that monitors changes in the absorption spectrum in response to charge carriers in a material. A schematic of the TA experiment is shown in Figure 1.5. A pump laser pulse excites charge carriers in the sample. At some delay time later, a continuum probe laser pulse is transmitted through the sample to measure its absorption spectrum and is collected by a spectrometer. The pump laser pulse is chopped, so that the sample absorption spectrum is measured with and without the excitation source. These two spectra are compared to give the transient absorption signal,

$$\Delta OD = OD_{\text{pump on}} - OD_{\text{pump off}}. \tag{1.8}$$

The time delay between the pump and probe laser pulses is varied to monitor how the absorption spectrum changes as a function of time. Based on changes in the TA spectrum, we infer changes in the charge carrier dynamics and electronic structure of the material.

A sample transient absorption spectrum is shown in Figure 1.6 with the linear absorption spectrum for reference. When excited charge carriers are present in a given electronic state as a result of the pump laser pulse, that state is not able to absorb light from the probe laser pulse because of the Pauli exclusion principle. Thus, the absorption with the pump on is less than the absorption without, and we get a negative transient absorption signal for that transition feature, often called a bleach signal (Figure 1.6a). If instead of reducing the absorption peak, the absorption peak shifts in energy, a derivative feature appears in the TA spectrum (Figure 1.6b). This may occur when a higher energy peak shifts because of the bi-exciton binding energy with an exciton in a lower energy state. A peak shift and bleach can occur simultaneously, for example in probing the band edge peak of a QD with a band edge exciton, and this process results in a bleach with an induced absorption shoulder (Figure 1.6c). Examples of a peak shift and a peak bleach with a small shift are shown in Figure 1.6d for the $1P_h$-$1P_e$ and $1S_h$-$1S_e$ transitions respectively in 5.8 nm PbS QDs in tetrachloroethylene excited at the band edge excitonic transition.

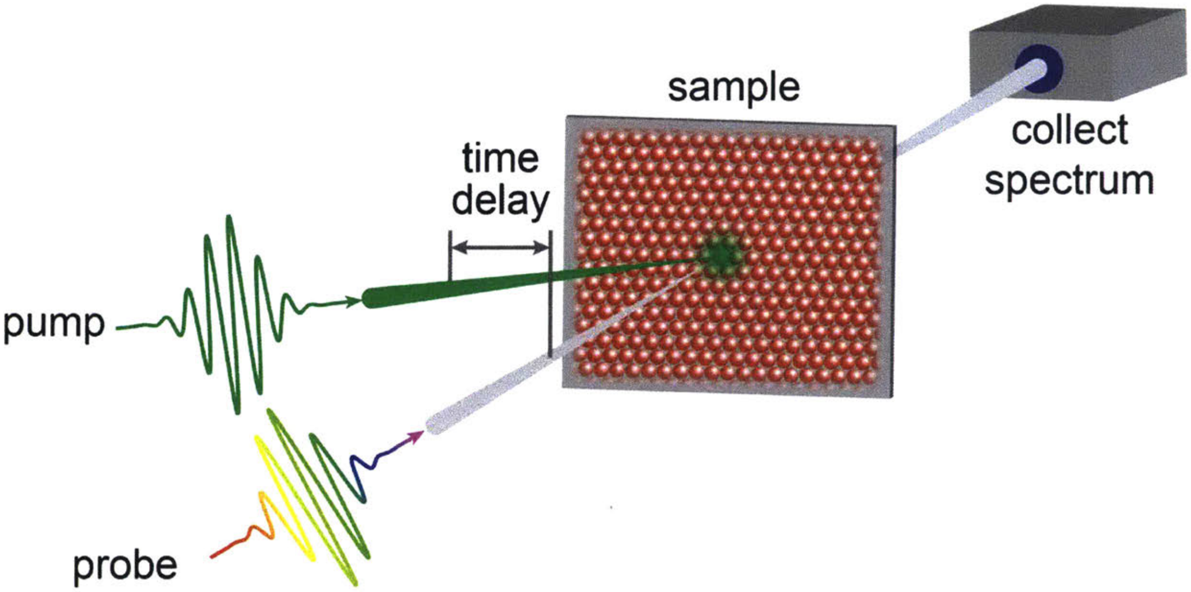

Figure 1.5. Schematic of a transient absorption experiment.

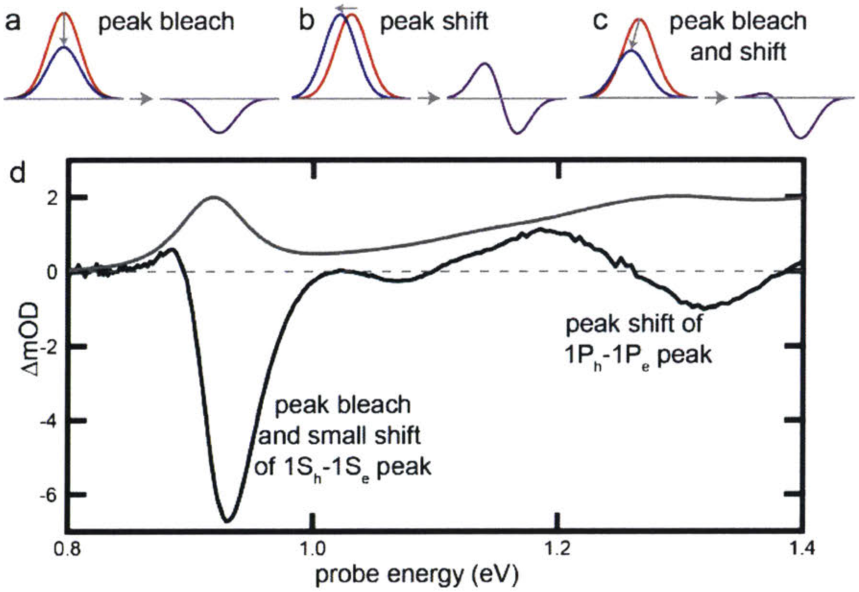

Figure 1.6. (a-c) Schematics of possible TA signals. (d) Sample TA spectrum of 5.8 nm PbS QDs in tetrachloroethylene showing typical features for a QD with an exciton in the band edge state.

When higher energy transitions in the QD sample are excited, it is possible to follow signatures of hot electron and hole relaxation as a function of time. Figure 1.7 shows typical transient absorption signatures of the $1S_h$-$1S_e$ and $1P_h$-$1P_e$ excitonic peaks in the first few picoseconds following excitation at 3.0 eV. The bleach of the $1S_h$-$1S_e$ feature grows in over the first 1-2 ps. The $1P_h$-$1P_e$ feature initially shows a bleach feature that becomes a peak shift signal over this same time scale. Schaller *et al.*[101] used TA to show that the hot electron relaxation rate from the $1P_h$-$1P_e$ to the $1S_h$-$1S_e$ transition becomes faster with decreasing PbSe QD size. Initially there is also a strong induced absorption on either side of the $1S_h$-$1S_e$ bleach which has been attributed to symmetry breaking by the hot electron-hole pair,[102] and which disappears with hot electron relaxation to the $1S_h$-$1S_e$ state.

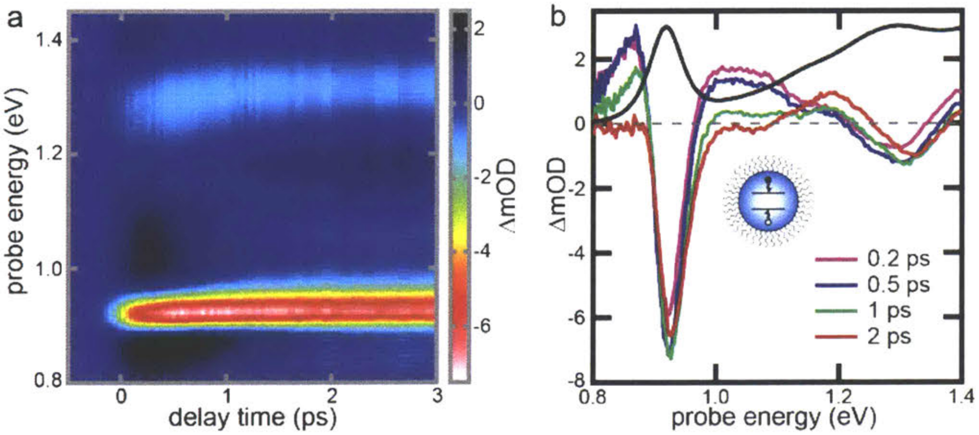

Figure 1.7. Transient absorption signatures of hot electron relaxation in 5.8 nm QDs in tetrachloroethylene. (a) 2D colorplot showing spectral changes as a function of time. (b) TA spectra at selected time delays.

Photoluminescence spectroscopy requires radiative recombination between an electron and a hole, and is therefore predominantly sensitive to excitons, which contain the electron and hole in close proximity. In contrast, transient absorption spectroscopy measures only changes in the absorption spectrum as a result of the occupation of excited electronic states, which can be from either excitons or free electrons and holes. If charge carriers are excitons, then the transient absorption and photoluminescence signals should have the same dynamics, as shown for the 1.6 μs lifetime for QDs in solution in Figure 1.8. However, in a coupled QD solid when charge carriers are predominantly free carriers, the TA and PL lifetimes will not necessarily be the same. It is also important to note that the sensitivity of the transient absorption signal to the occupation of a state by a charge carrier will depend on the degeneracy of that state. In CdSe QDs, the degeneracy of the valence band is much greater than the degeneracy of the conduction band, so the band edge bleach signal is sensitive only to the electron state.[103] In lead chalcogenide QDs, the conduction and valence bands are much closer to symmetric, and so the band edge TA bleach signal is equally sensitive to electrons and holes.

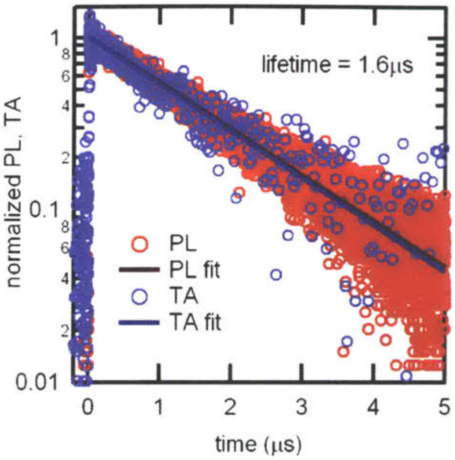

Figure 1.8. Photoluminescence and transient absorption lifetimes from PbS QDs in tetrachloroethylene.

Because transient absorption is sensitive to electronic state populations, not a specific recombination mechanism, it monitors both radiative and non-radiative recombination processes. At high excitation fluences where more than one photon is absorbed by a given QD, creating two or more excitons on that QD, an additional non-radiative recombination processes called Auger recombination occurs. In Auger recombination, one exciton recombines and transfers its energy to another charge carrier (electron or hole), which then relaxes back to the band edge by emitting phonons. The TA signatures of Auger recombination are shown in Figure 1.9a, which plots the area of the first absorption peak bleach of 5.8 nm QDs in tetrachloroethylene as a function of time and excitation density for band edge excitation at 0.92 eV.

The probability that a QD absorbs *m* photons follows a Poisson distribution:

$$P(m) = \frac{\langle N_{abs}\rangle^m e^{-\langle N_{abs}\rangle}}{m!} \tag{1.9}$$

where $\langle N_{abs}\rangle$ is the average number of absorbed photons per QD. $\langle N_{abs}\rangle$ can be expressed as

$$\langle N_{abs}\rangle = J(0)\sigma\frac{1-e^{-\alpha L}}{\alpha L} \tag{1.10}$$

where $J(0)$ is the incident photon fluence, σ is the absorption cross section, and $\alpha L = OD\ln 10$ is the absorption coefficient times the cuvette length measured for the linear absorption spectrum. At low excitation densities of $\langle N_{abs}\rangle < 0.2$, nearly all QDs have either 0 or 1 absorbed photon. The TA dynamics show a rise when the excitation pulse arrives and then flat dynamics because the exciton lifetime of 1.6 μs is much longer than the 1 ns time window in this experiment. As the excitation density increases, a fast decay component on a timescale of ~100 ps begins to appear. The increased initial bleach intensity reflects QDs with two or more excitons that undergo Auger recombination, reducing the transient bleach signal from those QDs. At high excitation densities of $\langle N_{abs}\rangle > 2$, nearly all QDs have at least one exciton initially, so following

Auger recombination all QDs contain exactly one exciton and the bleach intensity at 1 ns saturates. From the bleach intensity values at 1 ns as a function of incident fluence, we can estimate the absorption cross section from

$$N = N_0 \sum_{m=1} P(m) = N_0\left(1 - e^{-\langle N_{abs} \rangle}\right) \tag{1.11}$$

where N is the total number of excitons left at 1 ns and N_0 is the total number of QDs in the excitation beam path. By plugging equation (1.10) into equation (1.11) and plotting the bleach intensity at 1 ns as a function of fluence, we estimate the absorption cross section to be about 10^{-15} cm^2 (Figure 1.9b,c). Following low fluence excitation ($\langle N_{abs} \rangle < 0.2$) at high photon energies many times the band gap energy, signatures of Auger recombination are used as evidence for multiple exciton generation, also called carrier multiplication, which occurs when one high energy photon generates two or more band edge excitons.[104-109]

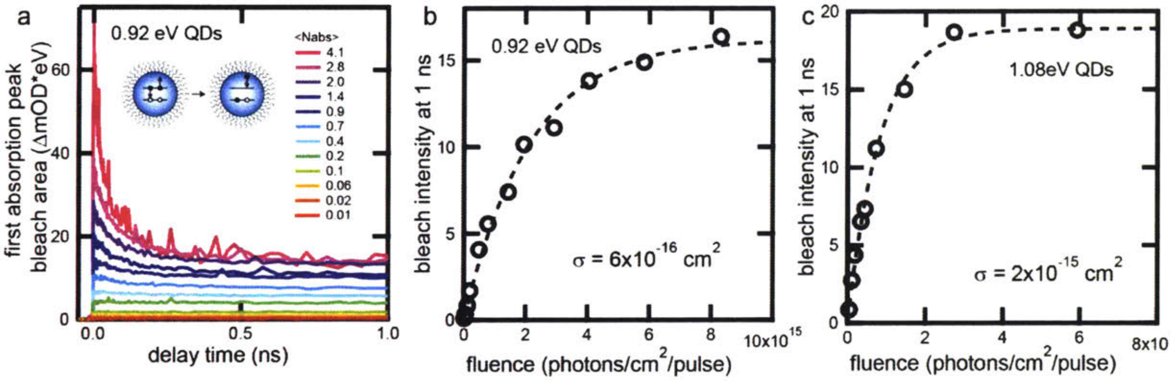

Figure 1.9. Transient absorption signatures of Auger recombination and calculation of the absorption cross section. (a) Increasing the pump fluence increases the number of absorbed photons per QD. Excitons on QDs with more than 1 exciton undergo Auger recombination, reducing the TA bleach signal in a few hundred picoseconds. (b-c) The absorption cross section can be estimated from a plot of the bleach intensity at 1 ns, after Auger recombination is complete but before appreciable single exciton recombination, versus the excitation fluence. This is shown for 5.8 nm QDs in (b) and 4.9 nm QDs in (c).

TA spectroscopy has historically been used to look at dynamics in isolated QDs in solution, and has been used extensively to study hot carrier relaxation,[101-103] Auger recombination,[16, 110-111] multiple exciton generation,[104-109] and trap state dynamics.[90] However, it can also be used to look at QD dynamics in solids, especially in cases when charge carriers dissociate and PL may not be a representative or feasible probe. TA spectroscopy on QD solids has been used to look at the effect of strong coupling on hot carrier relaxation,[61] fluence-dependent recombination mechanisms,[112] and trap state dynamics.[87] There is still a large parameter space that has been studied only with device-level measurements and has not been explored with optical techniques that are sensitive to nanoscale transport phenomena.

1.7 Thesis Overview

In this work, we monitor charge carrier hopping dynamics in monodisperse QD solids using transient absorption spectroscopy and examine the relative impacts of energetic and structural disorder on transport. In Chapter 2, we demonstrate homogeneously broadened QD solids made from monodisperse QD ensembles. Fitting our transient absorption data to a kinetic Monte Carlo model yields charge carrier hopping times ranging from 80 ps for the smallest QDs to over 1 ns for the largest, with the same ethanethiol ligand treatment. We make the surprising observation that in slightly polydisperse quantum dot solids, structural disorder has a greater impact than energetic disorder in inhibiting charge carrier transport. We also show that the homogeneous linewidth and the intrinsic charge carrier mobility increase with decreasing QD size. In Chapter 3, we extend the model developed in Chapter 2 to temperature-dependent measurements. We are surprised to observe increasing mobility with decreasing temperature when the transport mechanism is decidedly incoherent site-to-site hopping and not band-like transport. Once again, structural changes have a greater impact than energetic ones, and we adapt our model to include thermal expansion of the quantum dot superlattice. We find that a contraction of only 1-2 Å in the nearest neighbor distance is sufficient to overcome the Arrhenius dependence on charging energy and site-to-site disorder in our monodisperse QD solids. In Chapter 4, we show that the photophysical properties of a trap state ~100-200 meV below the band edge are consistent with that of strongly coupled QD dimers or small aggregates. Uncoupled QD solids with oleic acid ligands show trap-to-ground-state recombination that resembles Auger recombination, and coupled QD solids show charge transport between the trap and band edge states. Atomistic calculations confirm size-dependent trends in the energy difference between dimer and single QD band edge states and suggest that dimers are fused on (100) crystal facets. Overall, this thesis work demonstrates the importance of controlling the structure of monodisperse QD solids to optimize their charge transport.

Chapter 2 Charge Carrier Hopping Dynamics in PbS Quantum Dot Solids of Varying Size and Size Dispersity

The basis of this chapter has been published as:
R. H. Gilmore, E. M. Y. Lee, M. C. Weidman, A. P. Willard, W. A. Tisdale, "Charge Carrier Hopping Dynamics in Homogeneously Broadened PbS Quantum Dot Solids," *Nano Lett.* **17**, 2017.

2.1 Introduction

Energetic disorder inhibits charge carrier transport in a range of nanostructured materials including polymer and small molecule organics[113-114] and nanocrystal quantum dots (QDs).[115-117] In particular, energetic disorder in QD solar cells reduces both the open circuit voltage (due to extraction of charges at lower energy)[79] and the short circuit current (due to reduced minority carrier diffusion length).[68, 112] Because the quantum-confined band gap is a function of QD size, the size dispersity originating from colloidal synthesis often leads to inhomogeneously broadened electronic transitions.[118] Improved energetic homogeneity would be beneficial to long range charge carrier transport in quantum dot solids, and is an important avenue to pursue in further increasing solar cell efficiencies.[21, 119]

Charge carrier transport in PbS quantum dot solids with short ligands at or near room temperature is dominated by free carriers, rather than excitons.[55-56, 62] Charge transport is thought to proceed predominantly by site-to-site tunneling.[79] Faster tunneling is expected for shorter inter-particle spacing, and the resulting trend of increasing mobility with decreasing ligand length has been demonstrated through field-effect transistor (FET) measurements.[71] However, the dependence of mobility on QD size is more complicated. FET measurements have shown either increasing mobility with increasing QD size or non-monotonic trends,[71-72] whereas theoretical models predict that mobility should decrease with increasing QD size.[120] Spectroscopic techniques such as ultrafast transient absorption (TA) offer a complementary view of charge carrier dynamics in QD solids, and have previously been used to study charge carrier thermalization[61] and diffusion-assisted Auger recombination in quantum dot solids.[112]

Here we present a femtosecond transient absorption (TA) study of charge carrier hopping dynamics in electronically coupled PbS QD solids as a function of the QD size, d, and size dispersity, δ, of the QD ensemble. We fit the dynamic spectral redshift of the band-edge bleach signal to a kinetic Monte Carlo (KMC) model to extract the inhomogeneous linewidth and charge carrier hopping time. The samples with lowest size dispersity ($\delta \lesssim 3.3\%$) have inhomogeneous broadening smaller than 10 meV, or $0.4k_BT$ at room temperature. We use the measured inhomogeneous broadening and total ensemble linewidth to calculate homogeneous contributions to the absorption and emission linewidths. We find that the homogeneous absorption linewidth scales inversely with QD size from ~55 meV for 4.1 nm (1.3 eV) QDs to ~25 meV for 5.8 nm (0.92 eV) QDs. We also find that the charge carrier hopping rate and mobility increase with decreasing quantum dot size, consistent with theoretical predictions. Grazing-incidence small-angle X-ray scattering (GISAXS) measurements reveal that slower hopping times in solids with similar size QDs but greater size dispersity ($\delta \lesssim 4\%$) are a result of larger average inter-particle spacing due to less efficient packing. Thus, we find that structural disorder can have a greater effect than energetic disorder on transport properties in quantum dot solids made from slightly polydisperse ($\delta \lesssim 4\%$) ensembles.

2.2 Fabricate Samples of Varying Size and Size Dispersity

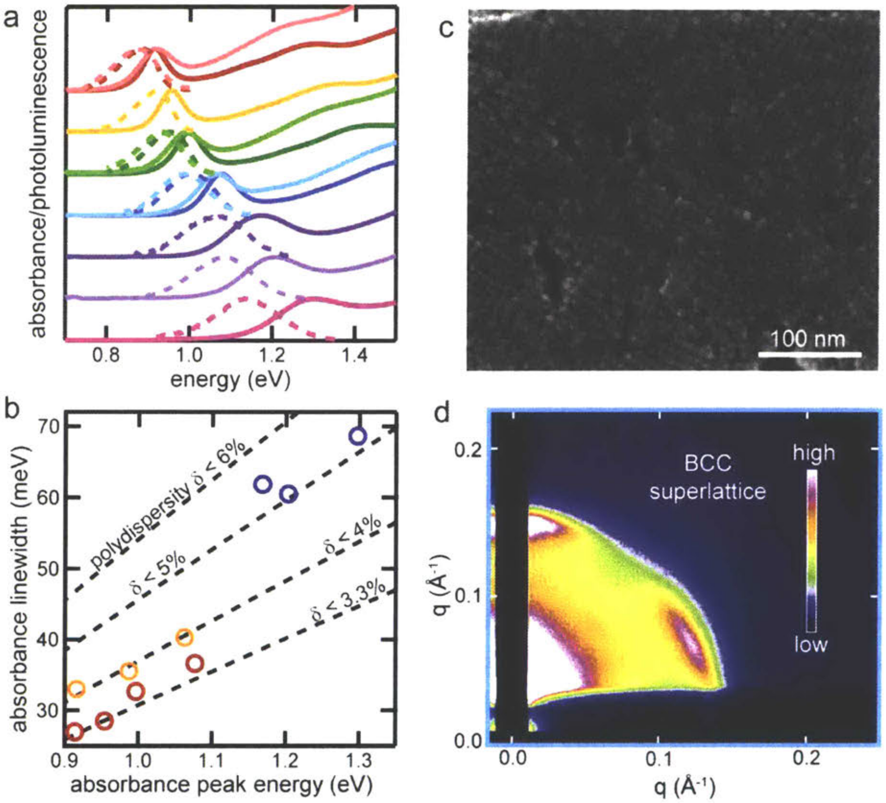

Figure 2.1. Tuning size dispersity in PbS quantum dot solids. (a) Solution phase absorption (solid lines) and emission (dashed lines) spectra for the ten PbS quantum dot batches used in this study. (b) Ensemble absorption linewidth (standard deviation) as a function of first absorption peak energy, with small QDs with $\delta \lesssim 5\%$ in blue, large QDs with $\delta \lesssim 4\%$ in orange and large QDs with $\delta \lesssim 3.3\%$ in red. The dashed lines show the calculated size dispersity of the ensemble assuming a delta function homogeneous linewidth. (c) HR-SEM image of a PbS QD solid (~100 nm thick, 0.92 eV absorption peak, $d = 5.8$ nm, $\delta < 4.1\%$) at ambient temperature following ethanethiol ligand exchange. (d) Grazing incidence small angle X-ray scattering (GISAXS) pattern of a similar film (1.17 eV absorption peak, $d = 4.9$ nm, $\delta < 3.5\%$), showing some retention of body-centered cubic (BCC) ordering following ligand exchange.

In Figure 2.1, we show absorption and emission spectra for PbS quantum dots of varying size and size dispersity that were synthesized according to previously published procedures (see

Section 2.9).[27, 37] The absorption spectra were fit (Figure 2.12 and Section 2.10) to determine the peak energy and ensemble linewidth (standard deviation) of the first absorption peak.[102] The standard deviation of the ensemble absorption linewidth is plotted as a function of the peak absorption energy in Figure 2.1b. The dotted lines indicate an upper bound on the size dispersity of the batch, which is calculated from a sizing curve by assuming the entire linewidth is due to inhomogeneous broadening.[27] The size dispersity, δ, is the standard deviation in QD diameter expressed as a percentage of the average diameter. We synthesized several sets of quantum dots of similar size but differing size dispersity, as shown in Figure 2.1b, where the lowest size dispersity samples ($\delta \lesssim 3.3\%$) are shown in red, and the more polydisperse samples of similar size ($\delta \lesssim 4\%$) are shown in orange. The smaller QDs, which have greater size dispersity ($\delta \lesssim 5\%$), are shown in blue.

To fabricate electrically conductive QD solids, QDs dispersed in toluene were spin coated onto glass substrates and ligand exchanged with ethanethiol inside a nitrogen glovebox (see Section 2.9). The resulting films were ~100-200 nm thick and nominally *n*-type as determined by Seebeck measurement.[50] The absorption spectra for the ligand exchanged films are shown in Figure 2.2. A high-resolution scanning electron microscopy (HR-SEM) image of a representative ethanethiol-treated QD solid shows regions of local close-packed order (Figure 2.1c). Prior to ligand exchange, these solids were highly ordered superlattices with a body-centered cubic (BCC) lattice structure (Figure 2.7).[51] Following the single step ligand exchange used here,[50] the QD solids still retained some of their original superlattice order, as shown in the GISAXS pattern for a representative sample in Figure 2.1d and for other samples in Figure 2.13 in Section 2.11, but significant long-range order was lost.

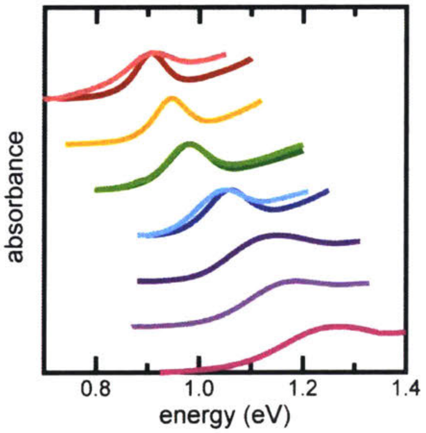

Figure 2.2. Absorption spectra of quantum dot solids with ethanethiol ligands. The colors are consistent with those in Figure 2.1a.

2.3 Transient Absorption of Coupled QD Solids

To monitor the nonequilibrium charge carrier dynamics, we employed ultrafast transient absorption spectroscopy. Samples were excited by a 2.4 eV (520 nm) excitation pulse, which was well above the band edge for all QD samples, which ranged from ~0.9-1.3 eV (1350-950 nm). This excitation pulse excited all QDs with nearly equal probability at an excitation density of 0.03-0.1 photons absorbed per QD per pulse (2×10^{13} photons/cm^2), which is two to three orders of magnitude greater than the dark free carrier density.[85] Following hot carrier relaxation, we monitored the band edge charge carrier population using a broadband infrared probe that spanned 0.8-1.45 eV (1600-850 nm, see Section 2.9 for additional details). The absorption bleach of the $1S_h$-$1S_e$ transition in PbS QDs is linearly proportional to the charge carrier population in both the $1S_h$ and $1S_e$ levels, but the peak bleach energy may shift with time as discussed in detail below.[45, 61, 110]

In Figure 2.3, we show representative absorption transients for QD solids with size dispersity of $\delta < 5.4\%$ (a,c,e) and $\delta < 3.5\%$ (b,d,f). Additional transients for all other samples are shown in Figure 2.14 in Section 2.11. The color plots in panels a and b show the transient absorption probe spectrum as a function of time. The linear absorption spectra are overlaid for reference (white solid lines, right side of graph). The breadth of the transient absorption spectrum reflects that of the linear spectrum, with the $\delta < 5.4\%$ solid having a noticeably broader TA bleach than the $\delta < 3.5\%$ solid. Additionally, the peak bleach energy, shown with a dashed line to guide the eye, shifts noticeably with time in the $\delta < 5.4\%$ solid, but not in the $\delta < 3.5\%$ solid. A few hundred picoseconds after excitation, the charge carrier population in the $\delta < 5.4\%$ solid is on QDs at the low energy edge of the linear absorption peak, whereas in the $\delta < 3.5\%$ solid, it is still on QDs at the absorption peak energy. Spectral slices at selected times are shown in panels c and d, and they confirm the previously mentioned observations of a broader transient bleach that redshifts with time in the $\delta < 5.4\%$ solid and a narrow transient bleach that redshifts minimally in the $\delta < 3.5\%$ solid. To extract the average band gap energy of QDs containing excited charge carriers as a function of time, we fit Gaussians to the bleach spectra (solid lines in panels c and d), whose central peak positions are shown in panels e and f. In the 2.8 ns time window in our experiment, the average energy of occupied QDs decreased by 24 meV in the $\delta < 5.4\%$ solid, but by only 2 meV in the $\delta < 3.5\%$ solid. The transient redshift dynamics did not change with excitation fluence over the range investigated here.

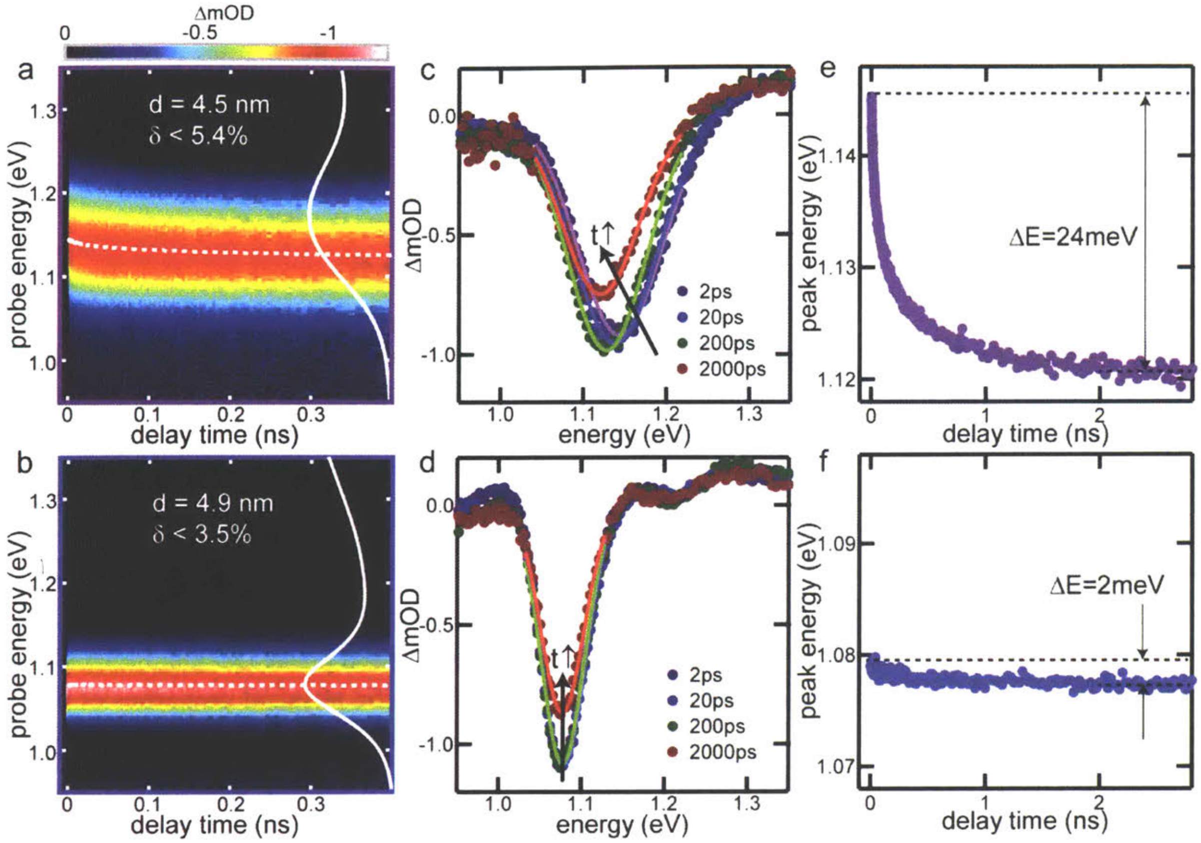

Figure 2.3. Transient absorption tracks the average energy of QDs containing excited charge carriers. (a, b) TA data collected from ethanethiol treated solids made from PbS QDs with $\delta < 5.4\%$ (a) and $\delta < 3.5\%$ (b). Solid white lines are the ground state linear absorption spectra. Dashed lines show the TA bleach peak position as a function of time. (c, d) Spectral slices at selected times showing the redshift of bleach peak in the $\delta < 5.4\%$ sample (c) but not in the $\delta < 3.5\%$ sample (d). Dots represent data and lines show Gaussian fits to the peaks. (e, f) Bleach peak energy as a function of time for the $\delta < 5.4\%$ (e) and $\delta < 3.5\%$ (f) samples.

2.4 Kinetic Monte Carlo Model to Fit Dynamics

To generate a microscopic physical interpretation of the transient absorption data, we performed kinetic Monte Carlo simulations of charge carrier dynamics in a model QD solid. By comparing simulation results to experimental observations, we can infer details about the microscopic structure of the material and determine how variations in this structure influence charge transport properties. Our simulations describe the dynamics of independent free charge carriers diffusing within a three-dimensional array of QDs. In our model, charge carriers are localized on individual QDs and diffuse via stochastic inter-QD hopping dynamics. As a first approximation, we assume symmetric conduction and valence bands under the effective mass approximation, so variation in the band gap energies is distributed equally between the conduction and valence bands (see Section 2.12 for a discussion of alternate treatments of band alignment). The hopping rates for individual charge carriers depend on the relative positions and energetics of nearby QDs. To model this dependence we describe the hopping rate for electrons in the conduction band and holes in the valence band from QD i to QD j using the Miller-Abrahams rate equation,[121]

$$k_{i \to j} = \begin{cases} k' \exp\left(-\frac{(\varepsilon_j - \varepsilon_i)/2}{k_B T}\right); & \varepsilon_j > \varepsilon_i \\ k'; & \text{otherwise.} \end{cases} \tag{2.1}$$

In this equation ε_i and ε_j are the band gap energies of QDs i and j respectively, so $(\varepsilon_j - \varepsilon_i)/2$ is the energy difference seen by an electron (hole) in the conduction (valence) band under the effective mass approximation, $k_B T$ is the Boltzmann constant times temperature, and

$$k' = k_0 \exp(-\beta r_{ij}), \tag{2.2}$$

where r_{ij} denotes the edge-to-edge distance between the QDs, k_0 is the intrinsic hopping rate, and β describes the tunneling radius. This generic model of intermolecular charge transport has been frequently utilized to describe free carrier diffusion in condensed phase QD and molecular systems.[114, 122-123] By parameterizing this model to reflect the specific physical properties of our experimental QD solids, we were able to reproduce the key features of the TA data, including the dependence of spectral linewidth and transient redshift on QD size dispersity (such as shown in Figure 2.3).

We simulated the effects of varying QD size dispersity by generating model QD solids with varying spatial and energetic characteristics. We modeled the spatial distribution of QDs by placing model QDs on the vertices of an ordered BCC lattice with a lattice spacing derived directly from GISAXS data. Because the model system is spatially ordered we can treat the quantity k' (eq (2.1)) as a physical constant for all nearest neighbor transitions. To simulate the effects of inhomogeneous broadening, we assigned each QD an energy (ε_i and ε_j in eq (2.1)), drawn randomly from a Gaussian distribution with mean $\bar{\varepsilon}$ and standard deviation σ_{inh}. Simulations were initialized by distributing charge carriers on random sites within the model QD solid, mimicking the consequences of photoexcitation with an above band-gap light source. We then propagated the system forward in time via a standard kinetic Monte Carlo algorithm.[124] For computational efficiency, and to reduce the number of model parameters, we restricted carrier hopping only to nearest-neighbor sites on a perfectly ordered lattice. We also ran analogous simulations that do not include these simplifying assumptions (i.e., simulations that feature both long-range hopping and the presence of explicit spatial disorder), but found no significant improvement in the ability to reproduce experimental results. For more details on the KMC simulations, see Section 2.13 and Figure 2.18.

The hops that drive charge carrier diffusion proceed preferentially to QDs with smaller band gaps. As a result, the distribution of charge carrier energetics shifts to lower energies as the system propagates from its initial state to a state in which the free charge carriers are fully thermalized within their respective bands. This thermalized state reflects a Boltzmann distribution over the inhomogeneously broadened density of states, which for our model is simply a Gaussian distribution[114] with the same standard deviation (i.e., $\sigma_{\mathrm{inh}}/2$ within each band, or σ_{inh} for the band gap) and with a mean band gap energy of occupied QDs that is red-shifted by a value of

$$\Delta\varepsilon = \frac{\sigma_{\mathrm{inh}}^2}{2k_{\mathrm{B}}T} \tag{2.3}$$

in the case of symmetric conduction and valence bands (see Section 2.12 for derivation and a discussion of alternate treatments of band alignment). This relationship implies that the overall magnitude of the transient red shift can be used to determine the inhomogeneous broadening of the QD solid. Furthermore, the timescale for the free charge carriers to reach energetic equilibrium is determined by the value of the hopping pre-factor, k', in eq (2.1). As a first approximation, we assume a single k' value that describes both electron and hole transport (experimental evidence for different electron and hole mobility is discussed later). Together the parameters σ_{inh} and k' determine the time-dependent profile of simulated TA data.

We simulated experimental data by first determining $\bar{\varepsilon}$ based on the position of the first peak in the absorption spectrum, and then fitting simulation to experiment by varying the parameters σ_{inh} and k'. In Figure 2.4, we show sample fits for the QD solid with $\delta < 5.4\%$ (Figure 2.3a,c,e), which exhibits large σ_{inh} and fast k' (Figure 2.4a), the QD solid with $\delta < 3.5\%$ (Figure 2.3b,d,f), which exhibits small σ_{inh} and moderate k' (Figure 2.4b), and a larger-diameter, intermediate dispersity QD sample ($\delta \lesssim 4\%$) exhibiting moderate σ_{inh} and slow k' (Figure 2.4c). Fits for all other quantum dot solids are shown in Figure 2.15.

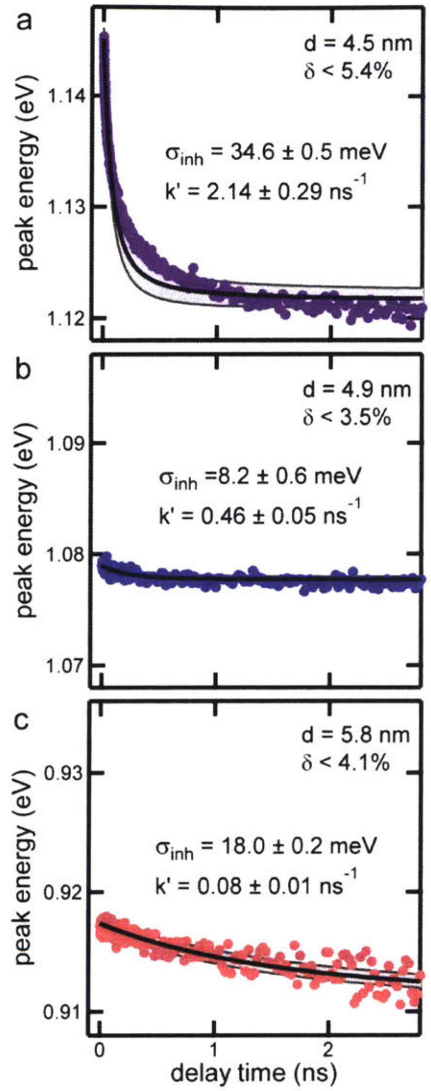

Figure 2.4. Kinetic Monte Carlo fits to transient absorption data. (a) KMC fit for a representative solid of small quantum dots with $\delta \lesssim 5\%$ (same sample as shown in Figure 2.3a). (b) KMC fit for a representative QD solid with $\delta \lesssim 3.3\%$ (same sample as shown in Figure 2.3b). (c) KMC fit for a representative QD solid with $\delta \lesssim 4\%$. Colored points are the data (same colors as Figure 2.1a), and black lines are the KMC fits with the gray shaded area showing one standard deviation error in the fitting parameters.

2.5 Single QD Linewidth

In Figure 2.5, we summarize the results of KMC simulation fits for all ten QD ensembles studied. As shown in Figure 2.5a, inhomogeneous linewidth, σ_{inh}, varies between 8-40 meV in these samples (see also Table 2.1), with smaller diameter batches (blue symbols) generally exhibiting greater inhomogeneous broadening. From the inhomogeneous linewidths and the ensemble total absorption and emission linewidths, we calculated the homogeneous absorption and emission linewidths for each sample according to

$$\sigma_{\text{hom}}^2 = \sigma_{\text{tot}}^2 - \sigma_{\text{inh}}^2 \tag{2.4}$$

The homogeneous absorption linewidth (defined as the standard deviation, σ_{hom}) decreased from 55 meV to 25 meV as the QDs size increased from 4 nm to 6 nm in diameter, as shown in Figure 2.5b (and Table 2.1). These values are consistent with a recent report by Jonas and co-workers, in which 2D spectroscopy was used to determine an average single-nanocrystal absorption linewidth of σ_{hom} = ~34 meV (~80 meV FWHM) in PbSe QDs with a 1.10 eV average band gap.[125]

Table 2.1. Key parameters from experiment and simulations: fitted absorption peak maximum; fitted total absorption linewidth (standard deviation, σ_{tot}); calculated QD diameter based on our sizing curve (*d*);[27] calculated size dispersity assuming delta-function homogeneous linewidth, expressed as standard deviation of the mean diameter (δ); the fitted hopping time constant, which is the reciprocal of the hopping rate prefactor, $t_{hop} = 1/k'$; fitted inhomogeneous linewidth from TA experiments (σ_{inh}); inferred homogeneous linewidth (σ_{hom} from eq (2.4) using σ_{tot} from column 2 and σ_{inh} from column 6); and the "actual" size dispersity calculated from the fitted inhomogeneous linewidth, σ_{inh}, from the KMC model.

abs peak (eV)	**σ_{tot} (meV)**	***d* (nm)**	**dispersity, δ**	**t_{hop} (ns)**	**σ_{inh} (meV)**	**σ_{hom} (meV)**	**model size dispersity**
	$\delta \lesssim 5\%$						
1.297	68.6	4.1	5.2%	0.43	40.1	55.7	3.0%
1.203	60.5	4.4	5.1%	0.44	35.5	49.0	2.9%
1.168	61.9	4.5	5.4%	0.47	34.6	51.3	2.9%
	$\delta \lesssim 4\%$						
1.062	40.3	5.0	4.0%	7.6	10.8	38.8	1.0%
0.987	35.6	5.4	3.9%	7.7	10.7	33.9	1.1%
0.916	33.1	5.8	4.1%	12.7	18.0	27.7	2.2%
	$\delta \lesssim 3.3\%$						
1.077	36.7	4.9	3.5%	2.2	8.2	35.8	0.8%
0.997	32.7	5.3	3.5%	3.1	10.0	31.1	1.1%
0.954	28.5	5.5	3.3%	4.9	7.5	27.5	0.8%
0.914	27.0	5.8	3.4%	5.0	8.2	25.7	1.0%

The corresponding homogeneous emission linewidth was consistently ~10-20 meV larger than the homogeneous absorption linewidth. These values are in line with previously reported homogeneous emission linewidths in smaller ~1.6 eV PbS QDs measured by single QD fluorescence (100 meV FWHM, or σ_{hom} = 43 meV),[126] photoluminescence excitation spectroscopy (170 meV FWHM, or σ_{hom} = 72 meV),[127] or solution photon correlation Fourier spectroscopy (173-234 meV FWHM, or σ_{hom} = 73-99 meV for ~1.6-1.9 eV QDs).[28] Interestingly, the homogeneous linewidths measured in PbS QDs are roughly twice as broad as homogeneous emission linewidths measured in visible-emitting QDs, such as CdSe, CdSe with CdS or ZnS shells, InP, or InAs, which have single-QD FWHM linewidths of 40-95 meV (σ_{hom} = 17-40 meV).[17, 118]

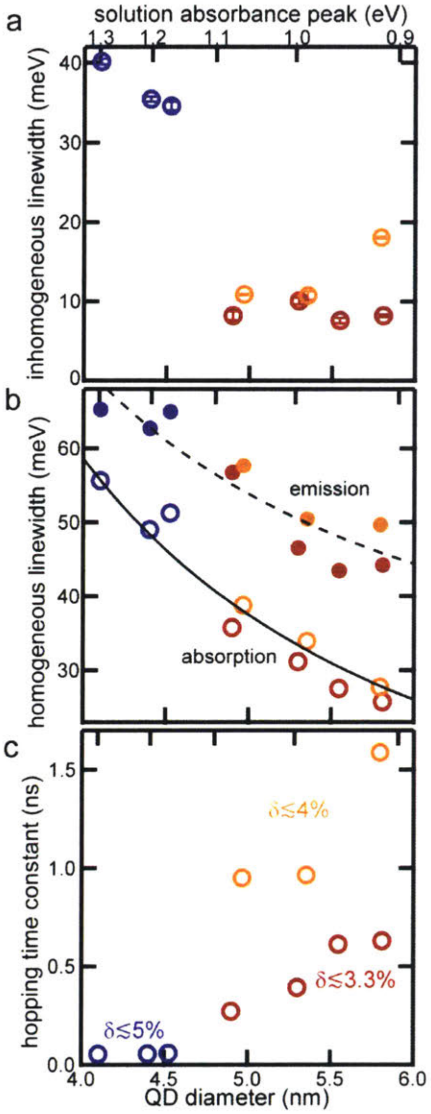

Figure 2.5. Fundamental parameters extracted from KMC fitting. (a) Inhomogeneous linewidths (standard deviation) of the ten PbS QD samples as found from the fitted energy redshift in the KMC simulations. (b) Homogeneous linewidth (standard deviation) for the absorption (circles) and emission (points) spectra, calculated from the ensemble linewidth and the fitted inhomogeneous linewidth. The solid (absorption) and dashed (emission) lines show the $1/R^2$ scaling expected for homogeneous broadening dominated by deformation-potential coupling to acoustic phonons.[128] (c) Characteristic hopping time, defined as the inverse hopping rate pre-factor adjusted for the number of nearest neighbors in the lattice. Symbol colors are consistent with Figure 2.1b.

Strong coupling to acoustic phonons has been proposed as the origin of the broad homogeneous linewidth in PbS QDs. Fernée *et al.* identified a 125 meV temperature-dependent component to the photoluminescence homogeneous linewidth, indicating rapid dephasing in about 5 fs.[127] Kamisaka *et al.* had predicted this fast dephasing time in lead salt QDs.[129] In an early theoretical model, Takagahara predicted increasing coupling to acoustic phonons with decreasing QD size, due primarily to deformation potential coupling, which follows a $1/R^2$ size dependence.[128] Bozyigit *et al.* also observed coupling to low energy acoustic phonon modes originating from mechanical softening of the QD surface.[34] The size-dependence of the homogeneous linewidth shown in Figure 2.5b follows the expected $1/R^2$ size-dependence (solid line for absorption, dashed line for emission), further supporting the proposed origin of the homogenous linewidth in PbS QDs as deformation potential coupling to acoustic phonons. The dephasing times calculated from our homogeneous linewidths are 5-10 fs, in agreement with previously reported experimental and theoretical results.[127-128]

It is often observed that the ensemble emission linewidth is slightly larger than the ensemble absorption linewidth in highly monodisperse PbS quantum dots.[27, 35] Since the inhomogeneous linewidth arises primarily from size dispersity *via* the size-dependent band gap[125, 130] – which should impact both absorption and emission equally – the difference in ensemble linewidth likely reflects a difference in the absorption and emission homogeneous linewidths. It has been suggested that photoluminescence in PbS QDs may arise from recombination between a band edge charge carrier and a localized, surface-trapped charge carrier[131] or from a combination of band edge and sub-band edge photoluminescence.[97, 127] Emission from both the $1S_h$-$1S_e$ band edge transition and a defect state may explain the asymmetric lineshapes of the emission spectra,[127] and be responsible for larger homogeneous emission linewidths.

We note that by making the assumption of symmetric contribution of band gap variation to conduction and valence band levels, we are determining an upper bound on σ_{inh} and therefore a lower bound on σ_{hom} (see Section 2.12). Atomistic simulations have suggested that the bands are not actually symmetric, but that the conduction band energy is more sensitive to variations in QD size than the valence band energy.[42] To address the possibility of band asymmetry, we also ran simulations in which we assumed that the size-dependent energetic dispersity was all contained in a single band, while the other level is pinned. This extreme case gives qualitatively similar results to the effective mass model with symmetric band alignment, but provides a lower bound on σ_{inh} and an upper bound on σ_{hom}. These results are presented in Section 2.12 in Figure 2.16 and Figure 2.17.

The quality of the KMC simulation fits to the transient redshift data shown in Figure 2.4 can be improved by recognizing that both electrons and holes contribute to the transient absorption signal, and that they likely have different hopping time constants.[71] For the small QDs with $\delta \lesssim 5\%$, which appear to have faster initial dynamics but slower long time dynamics, we fit a KMC model with two rate constants k_1' and k_2' (but still a single value of σ_{inh}). The results are summarized in Figure 2.6. The faster hopping rate constant was consistently found to be 15-20 times greater than the slower time constant. However, the transient absorption experiment alone cannot identify which charge carrier – electron or hole – is more mobile.

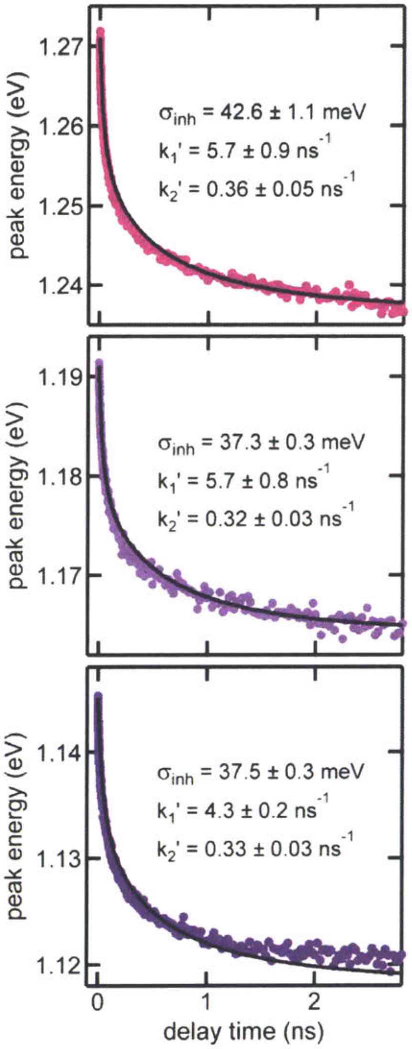

Figure 2.6. Kinetic Monte Carlo fits for the small samples with size dispersity $\delta \lesssim 5\%$ with two time constants representing different hopping rates for electrons and holes.

Our data support the hypothesis that QD size dispersity is the dominant source of static energetic disorder in thiol-exchanged PbS QD solids. Other authors have pointed to the importance of surface ligand variation as a significant source of energetic disorder in QD solids.[21] Brown *et al.* used the ligands on the QD surface to tune the conduction and valence band position relative to the vacuum level by up to 1eV without changing the band gap.[132] One therefore might expect QD-to-QD variations in surface chemistry to impact the energy landscape seen by mobile electrons and holes. However, if surface chemistry-induced energetic disorder was significant (i.e. same magnitude as heterogeneity due to size-dependent band gap), there would not be a driving force for transport to QDs with smaller band gaps. Since we clearly and directly observe a redshift toward charge carrier occupation of smaller-band gap QDs over time, and the magnitude of this redshift is 1) consistent with the inhomogeneous broadening evident in the linear absorption spectra, and 2) consistent with the tunable size dispersity in the ensemble, we conclude that size dispersity is the dominant source of static energetic disorder in our QD solids.

2.6 Impact of Size Dispersity on Transport

In Figure 2.5c, we plot the inverse hopping rate pre-factor, $1/8k'$, adjusted for the eight nearest neighbors in a BCC lattice – hereafter referred to as the characteristic hopping time. The characteristic hopping time, $1/8k'$, is slower in the solids with $\delta \lesssim 4\%$ than those of similar QD size with $\delta \lesssim 3.3\%$. This parameter does not directly include the contribution of energetic disorder, which enters into the rate equation only through the Boltzmann factor (eq (2.1)). Instead, larger average QD spacing in the $\delta \lesssim 4\%$ solids (revealed by GISAXS data presented in Figure 2.13) yields slower intrinsic tunneling rates. Many studies have shown the exponential dependence of the tunneling rate on the distance between QDs (eq (2.2)), which is usually controlled by varying the ligand length for fixed QD size and size dispersity.[71, 77] Here, the ensemble size dispersity determines the interparticle spacing. Monodisperse samples self-assemble into highly ordered superlattices, and retain some of their order even after solid-state ligand exchange.[50-51] In contrast, solids with greater size dispersity do not self-assemble as well (Figure 2.7),[8, 133] and the lattice is not able to contract as much during ligand exchange. Larger average interparticle spacing implies larger edge-to-edge spacing in solids with greater size dispersity, even with identical ligand exchange procedures. The hopping prefactor includes an exponential dependence on the edge-to-edge spacing between QDs, as shown in eq (2.2), so the larger spacing and increased spatial disorder results in slower characteristic hopping times in the $\delta \lesssim 4\%$ solids. When the hopping time constant data in Figure 2.5c are re-plotted against center-to-center spacing – instead of QD diameter – the $\delta \lesssim 3.3\%$ and $\delta \lesssim 4\%$ samples collapse onto a single monotonic trend (Figure 2.8).

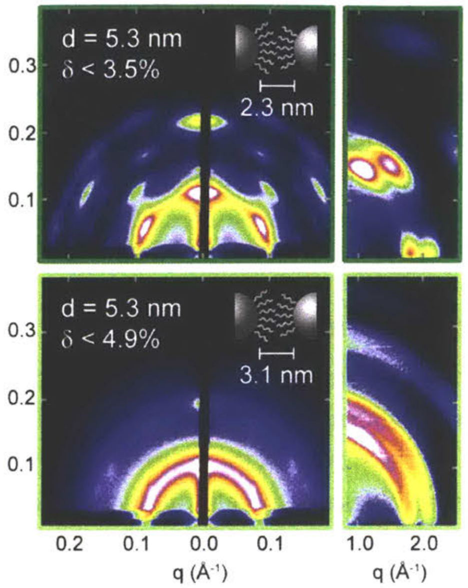

Figure 2.7. Grazing-incidence small-angle (left) and wide-angle (right) X-ray scattering (GISAXS and GIWAXS) patterns for quantum dot solids with $\delta < 3.5\%$ (top) and $\delta < 4.9\%$ (bottom) with native oleic acid ligands. The $\delta < 3.5\%$ solid shows a highly ordered superlattice with individual QDs all oriented in the same way with the atomic planes aligned. In contrast, the $\delta < 4.9\%$ sample shows much less order, both for the superlattice and the individual QD orientation. The poorer self-assembly in the $\delta < 4.9\%$ solid results in an average edge-to-edge QD spacing of 3.1 nm, which is 0.8 nm larger than that of the $\delta < 3.5\%$ sample (a 35% increase).

Both energetic and spatial disorder inhibit charge transport and prevent the development of delocalized charge carriers and band-like transport.[79, 83] To understand the relative magnitudes of the impact of spatial and energetic disorder on charge carrier hopping rates, we compare the average time between hops in the diffusive transport regime, $1/k_{\text{hop}}$, which includes the influence of both spatial and energetic disorder, with the characteristic hopping time, $1/8k'$, which does not include contributions from energetic disorder. In the limit of a perfectly monodisperse sample, these two values are the same since the Boltzmann factor is unity and there are 8 nearest neighbors in a BCC lattice. The comparison of these two parameters, as extracted from KMC fits to our experimental data, is shown in Figure 2.9a. For the small QDs with inhomogeneous linewidths of about $1.5k_BT$ ($\delta \lesssim 5\%$), the energetic disorder accounts for about one third of the hopping time, as $1/k_{\text{hop}}$ is about one and a half times $1/8k'$. For the $\delta \lesssim 3.3\%$ samples for which $\sigma_{\text{inh}} < 0.4k_BT$, the energetic disorder accounts for less than 2% of the hopping time. Indeed, transport in these homogeneously broadened solids is in a nearly flat energy landscape, as shown schematically in Figure 2.10. In contrast, the increased spatial disorder in the $\delta \lesssim 4\%$ solids of similar size increases the hopping time by over a factor of two. Thus, while energetic disorder on the order of k_BT inhibits charge transport, as the size dispersity decreases further, spatial disorder becomes the dominant factor inhibiting charge transport.

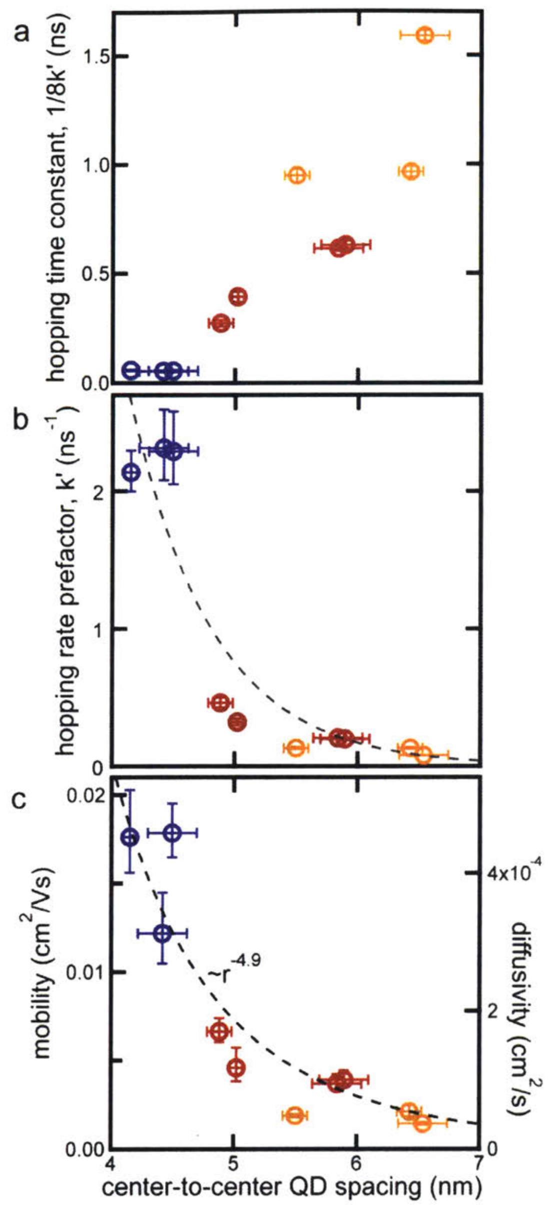

Figure 2.8. Intrinsic charge carrier hopping rates as a function of center-to-center QD spacing (a) Hopping times from Figure 2.5 plotted vs center-to-center QD spacing, rather than QD diameter. (b) The hopping rate decreases with increasing center-to-center spacing. Dashed line shows an exponential fit. (c) Even after accounting for a greater distance travelled per hop, mobility and diffusivity decrease with increasing center-to-center QD spacing. Dashed line shows $d_{cc}^{-4.9}$ fit.

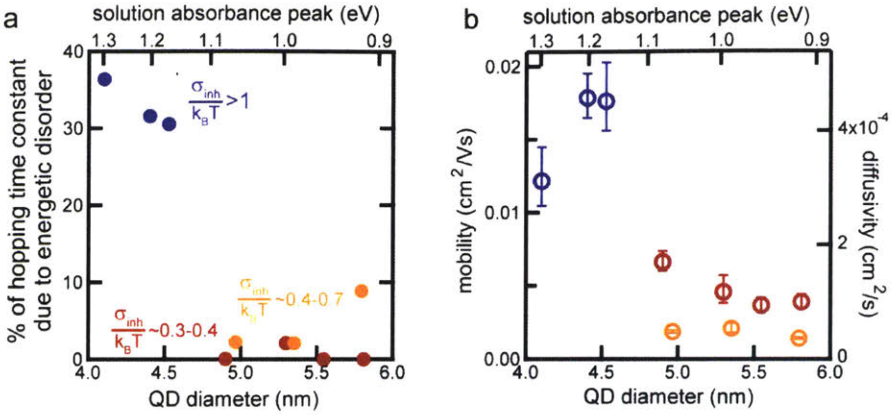

Figure 2.9. (a) The percentage of the hopping time that is attributed to energetic disorder, as given by $(1/k_{tot}-1/8k')/(1/k_{tot})$. (b) Calculated intrinsic charge carrier mobility and diffusivity as a function of QD size.

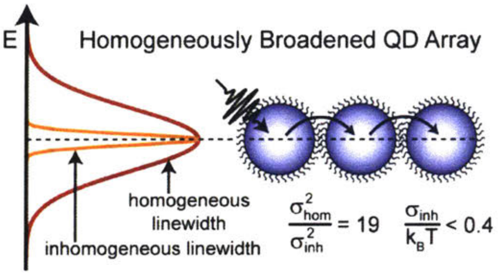

Figure 2.10. Schematic showing a homogeneously broadened QD solid with an inhomoeneous linewidth much less than both the single QD (homogeneous) linewidth and the available thermal energy at room temperature.

2.7 Size-dependent Hopping Rate

Because our KMC fitting model is a spatiotemporal model, it directly provides information regarding charge carrier transport. By tracking the mean squared displacement (MSD) as a function of time (Figure 2.11a), we determined the diffusivity, D, from the KMC simulation according to,

$$\lim_{t\to\infty} MSD = 6Dt. \tag{2.5}$$

The diffusivity relates to the mobility, μ, by the Einstein relationship, $\mu=qD/k_BT$. In Figure 2.9b, we present the intrinsic free charge carrier mobility and diffusivity as a function of QD size. This calculated mobility is in line with mobility values reported in the literature for lead salt QD solids with thiol ligands.[77, 134] Other chemical binding groups may give faster or slower mobility for similar ligand lengths, because the chemical nature of the ligands impacts the tunneling barrier height.[134-135] For example, time-resolved microwave conductivity measurements showed that amine ligands have higher mobility than either carboxylic acid or thiol ligands,[77] and transient absorption measurements by Gao *et al.* on films of ethanediamine-treated PbSe QDs found fast charge carrier relaxation and diffusion, reaching equilibrium in a few picoseconds.[61]

The diffusivity can be related to the diffusion length, L_D, using the charge carrier lifetime, τ,

$$L_{\mathrm{D}} = \sqrt{D\tau}. \tag{2.6}$$

However, determining the intrinsic charge carrier lifetime in coupled PbS QD solids is difficult because the lifetime is power-dependent at higher excitation densities due to diffusion-assisted Auger recombination,[112] and because signal-to-noise becomes a problem at sufficiently low excitation densities in thin film samples (<0.001 photons absorbed per QD per pulse). Additionally, even at low excitation densities, the charge carrier lifetime in QD solids is often determined by trapping processes, rather than by an intrinsic band edge carrier lifetime.[98, 115] Thus, rather than calculating a single diffusion length, the intrinsic charge carrier diffusion length is plotted as a function of charge carrier lifetime in Figure 2.11b, for lifetimes out to the PbS QD solution lifetime of 2μs.[27]

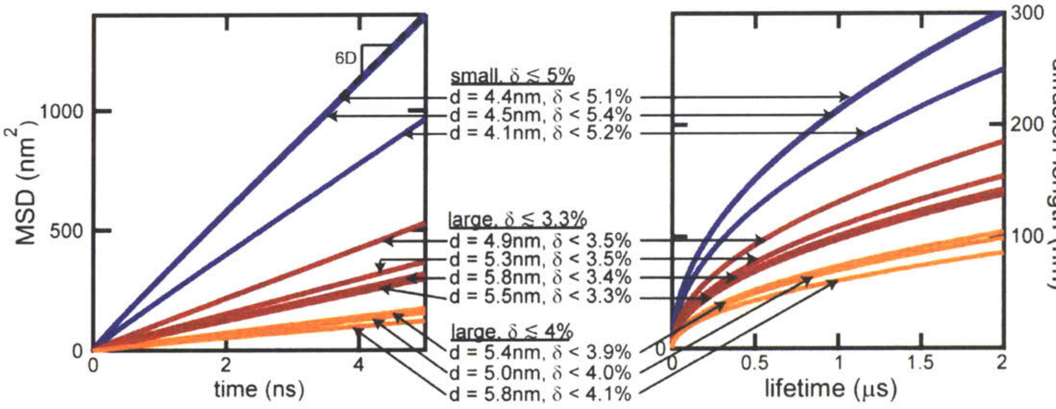

Figure 2.11. (a) Mean squared displacement as a function of time from the KMC simulation. The dashed line shows an example of a linear fit at long times to get the diffusivity from the KMC simulation. (b) Simulated charge carrier diffusion length as a function of carrier lifetime.

Charge carrier diffusivity is proportional to the site-to-site hopping rate through the relationship,

$$D = k_{\mathrm{hop}} d_{\mathrm{cc}}^2/6, \tag{2.7}$$

where d_{cc} is the center-to-center spacing between quantum dots. While the hopping rate, k_{hop}, is expected to increase with decreasing QD size because of stronger electronic coupling between smaller QDs, the shorter distance traveled per hop ($D \sim d_{\mathrm{cc}}^2$) and the larger charging energy in smaller QDs ($E_c \sim 1/d$) push the trend in the opposite direction.[72, 79, 136] Overall, these competing factors complicate predictions of size-dependent mobility. Nonetheless, Shabaev *et al.* predicted that the hopping rate would dominate, and the mobility would decrease with increasing QD size.[120] Time-of-flight photocurrent measurements concur, also showing decreasing mobility with increasing QD size,[76] as do our measurements, shown in Figure 2.9b. However, electrical measurements of the mobility using field-effect transistor (FET) structures disagree, often showing the opposite trend of increasing mobility with increasing QD size.[71-72] Bozyigit *et al.* pointed out that the discrepancy between mobility measurements made by FET and those made by other techniques lies in the contribution of trapped charge carriers to the effective FET mobility.[93] On average, traps are deeper when the band gap is larger (i.e. smaller QDs), resulting in a larger fraction of trapped charge carriers in films of smaller QDs and a decrease in the apparent mobility as measured by FET. In contrast, the spectroscopic measurements presented here reflect the intrinsic charge carrier hopping dynamics of the band-edge population, which reveal the theoretically predicted trend of decreasing mobility with increasing quantum dot size.

Because we directly monitor the band-edge population, charge carriers are excluded from our measurement if they fall into deep traps. Fast trapping and release from shallow traps on timescales within our measurement time window have been observed in PbSe QD photodetectors.[22] There is evidence that similar shallow traps are present in our PbS QD solids in the weak sub-band-edge bleach signal present in several samples shown in Figure 2.14. These shallow traps would affect our results by increasing the amount of time it takes a charge carrier to reach a thermally equilibrated state and may be a source of error between the data and KMC model fit, in particular contributing to the slower time component of the red-shift in smaller QD solids. Other authors have estimated that the density of these shallow traps is on the order of 1 in 100 QDs,[85] and that their contribution to the hopping dynamics is small. However, any contributions from trapping and escape from shallow trap states would suggest that the mobilities and diffusivities are lower bounds for the intrinsic charge carrier transport behavior.

2.8 Conclusions

We have shown that charge transport in homogeneously broadened PbS quantum dot solids can be achieved with sufficiently monodisperse QD ensembles. Transient absorption spectroscopy paired with a kinetic Monte Carlo model was used to determine the inhomogeneous linewidth and charge carrier hopping time for a range of samples. We confirmed theoretical predictions for $1/R^2$ size dependence of the homogeneous linewidth as a result of coupling to acoustic phonons, and for increasing mobility with decreasing QD size. We found that when the energetic disorder is below the available thermal energy, the size dispersity still contributes substantially to spatial disorder, which inhibits charge transport. To further increase the spatial order, and to improve the long-range order needed for many optoelectronic devices, solution-phase ligand exchanges will be needed. With monodisperse QDs, solution-phase ligand exchange, and controlled self-assembly, sufficiently ordered solids that are free from energetic and spatial disorder should be possible, encouraging continued advances in QD optoelectronic devices.

2.9 Experimental Methods

PbS QD Synthesis and QD Solids Preparation. The three smallest batches of PbS quantum dots were synthesized according to Zhang *et al,.*[37] and the larger batches according to Weidman *et al.*[27] Size dispersity was controlled by varying the Pb:S precursor species ratio, with higher Pb precursor concentrations yielding more monodisperse ensembles. Purified QDs were re-dispersed in toluene at a concentration of 100 mg/mL in a nitrogen glovebox. 40 μL of the solution was spun at 1500 rpm for 30 s onto a 0.5 in square borosilicate glass slide (Schott D-263 from Thermo Fisher) that had been cleaned and treated overnight in a 0.02M (3-mercaptopropyl)trimethoxysilane (Sigma-Aldrich, 95%) solution in toluene to improve QD adhesion. The sample was then placed in a 0.1M solution of 1-ethanethiol (Sigma-Aldrich, 97%) in acetonitrile for 24 hours for ligand exchange. This created films with an optical density of about 0.1 at the first absorption peak. Prior to ligand exchange, these QDs are air stable,[27] and following ligand exchange, the samples were kept in an inert atmosphere at all times, including during TA measurements.

Transient Absorption Spectroscopy. Transient absorption spectroscopy was performed at the Advanced Optical Spectroscopy and Microscopy Facility at the Center for Functional Nanomaterials at Brookhaven National Laboratory. A commercial Ti:sapphire femtosecond regenerative amplifier (SpectraPhysics Spitfire Pro) operating at a 1 kHz repetition rate was used to generate 800 nm fundamental. An optical parametric amplifier (LightConversion) was used to generate pump pulses at 520 nm with ~100 fs time resolution. The probe pulses were generated by focusing a small portion of the 800 nm fundamental onto a sapphire crystal to generate a white-light supercontinuum over the range of 850–1600 nm. An 850 nm longpass filter was used to remove excess fundamental light at 800 nm from the probe. The probe light was split into signal and reference beams, which were dispersed by concave grating spectrometers and detected on a shot-by-shot basis by fiber-coupled InGaAs diode arrays (256 pixels, 750 – 1600 nm) coupled to a high-speed data acquisition system (Ultrafast Systems). The pump-probe time delay was controlled by a mechanical delay stage (Newport). Each measurement is an average of at least two scans of the delay stage to ensure that dynamics were not changing with laser exposure time. Probe power was typically only a few hundred nanowatts, much less than the pump powers of 7-40 microwatts.

Kinetic Monte Carlo Simulations. Numerical simulations of carrier transport in QD solids were done using a kinetic Monte Carlo (KMC) algorithm in which a free carrier (electron or hole) undergoes a series of stochastic hops between individual quantum dots according to a rate given by the Miller-Abrahams model in equation (1) in the main text. The model system consists of a three-dimensional periodically replicated cell in a BCC lattice configuration containing 16,000 QDs. Each QD is randomly assigned a site energy, ε, drawn from a Gaussian distribution with a standard deviation, σ_{inh}. Statistics were averaged over 10 realizations of the QD solid (energetic disorder), and each realization of the QD solid consisted of 7.5×10^6 single carrier trajectories. In the main text, we reported the average and standard deviation of the observable quantity such as transient energetics of free charges from these trajectories. Our code is available at *http://github.com/emyl3196/QDcarrier*.

Fitting the KMC model to the TA data. Based on the predicted average transient energetics during the first ~3 ns (the longest time delay in the transient absorption experiment) of free carriers from the KMC simulations, we solved for the two unknown parameters—inhomogenous linewidth (σ_{inh}) and the hopping rate prefactor (k')—by minimizing the sum of residuals using SciPy v. 0.15.0's built in stochastic population based method for global optimization called the differential evolution algorithm.[137] For each experiment data set, optimal fit parameters were obtained using the differential evolution algorithm with a population size of 15 and generation number of 5 such that there were total of 180 function evaluations (note: 5 [generation number]*15 [population size]*2 [number of parameters] = 180 function evaluations). In each function evaluation, a single realization of the QD solid with 7.5×10^6 KMC trajectories were done to average these KMC statistics and predict the transient energetics. Once these parameters were found, we then used these values for the full KMC simulation (10 realizations of the QD lattice * 7.5×10^6 single carrier trajectories) to calculate carrier diffusivity and average hopping time in the diffusive transport regime, in which a larger lattice (up to 35,000 QDs) and longer simulation time (up to 40 ns) was used if necessary.

Characterization. Absorption spectra were collected using a Cary 5000 UV-vis-NIR spectrophotometer. Solution phase measurements were made in normal transmission mode and include contributions from both absorption and scattering. For these measurements, QDs were suspended at low concentration in tetrachloroethylene. Thin film measurements were made using an integrating sphere attachment designed to correct for the large amount of scattering observed in these samples.

Photoluminescence spectra were collected using a BaySpec NIR spectrometer. QDs were suspended at low concentrations in tetrachloroethylene for photoluminescence measurements.

Scanning electron microscopy (SEM) was performed on a Zeiss Merlin operating at 20 kV. Samples were prepared on silicon substrates following the same methods as used for the transient absorption measurements.

Grazing-incidence small-angle X-ray scattering (GISAXS) measurements were performed at the D1 beamline of the Cornell High Energy Synchrotron Source (CHESS). The X-ray beam was produced by a hardbent dipole magnet and a Mo:B_4C multilayer double-bounce monochromator, producing radiation with a wavelength of 1.166 Å and bandwidth of 1.5%. The GISAXS patterns were collected on a DECTRIS Pilatus3 200 K detector. The sample-to-detector distances were calibrated using a silver behenate standard. GISAXS data were collected with a 1 s exposure time and a 0.25° incident angle. The illuminated sample area was 100 μm by 1 cm. GISAXS measurements were performed on the same samples used for TA, after taking the TA measurements.

2.10 Appendix A: Fitting Absorption Spectra to Determine Peak and Linewidth

Previous reports have suggested that lead salt quantum dot absorption spectra should be fit to a series of Gaussian excitonic peaks and a Rayleigh scattering background.[102, 138] Equally good fits can also be obtained with an exponential background to approximate very broad electronic transitions.[102] We find that doing so results in better agreement in the size dependent trends of the absorption and photoluminescence homogeneous linewidths, as shown in Figure 2.12. In the samples with greater size dispersity, broader higher energy features have greater overlap with the band edge absorption feature, having the effect of making it appear broader and higher in energy. Thus the maximum value and the half-width at half-maximum (HWHM) on the low energy side will underestimate the quantum dot size (overestimate peak value) and overestimate the size dispersity. This disagreement is worse for larger size dispersity samples.

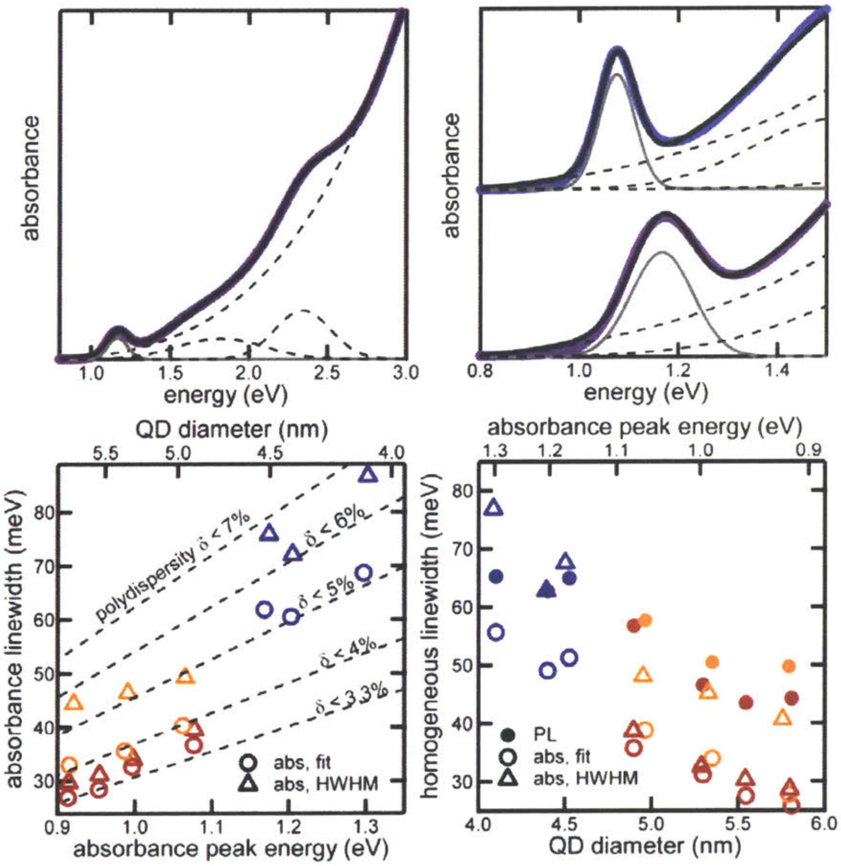

Figure 2.12. Fitting absorption spectra to determine peak energy and linewidth. (a) Sample fit (black solid line) to absorption spectrum (purple) with E^4 Rayleigh scattering and three Gaussian peaks for the defined features (dotted lines, band edge peak in gray). (b) Sample absorption spectra fits for monodisperse (top) and polydisperse (bottom) samples near the first absorption peak, showing the fitted peak position in dark gray. (c) Comparison of the absorption linewidth for the fit (open circles) to that determined by measuring the half-width at half-maximum (HWHM, triangles) on the low energy side of the peak. (d) Comparison of the calculated homogeneous linewidth for the absorption spectra fits (open circles), absorption spectra HWHM (triangles), and PL (closed circles).

2.11 Appendix B: Experimental Data for All QD Sizes

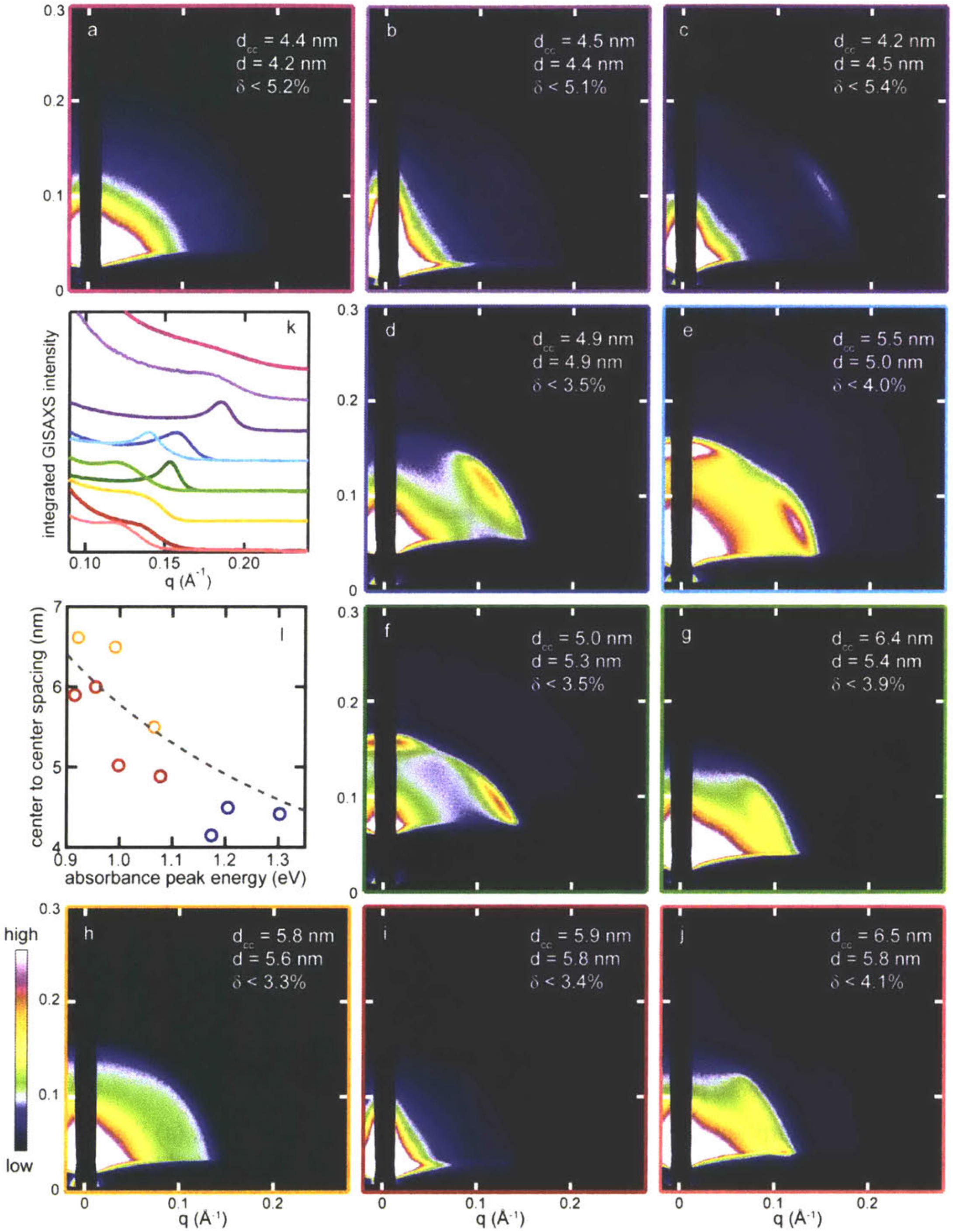

Figure 2.13. (a-j) GISAXS data for all samples, labelled with the center-to-center spacing, d_{cc}, QD diameter, *d*, and size dispersity, *δ*. Because QDs are actually faceted, not spherical, very close packing with aligned crystal facets can result in $d_{cc} < d$.[136] (k) Azimuthally integrated GISAXS intensity. (l) Center-to-center spacing, with dashed line showing expected spacing based on sizing curve and 0.5 nm edge-to-edge spacing for ethanethiol.[50]

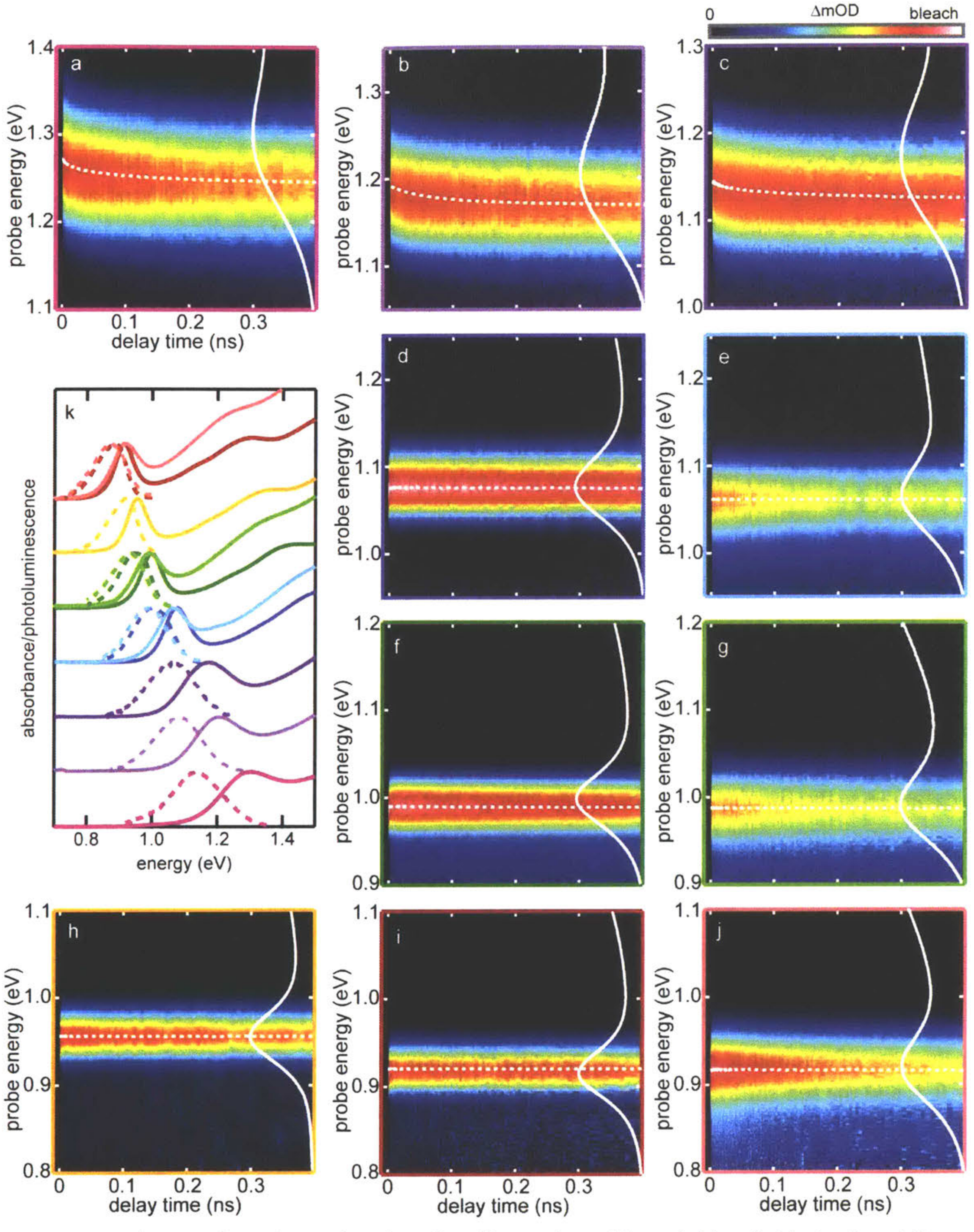

Figure 2.14. (a-j) Transient absorption data for all samples with peak bleach (dashed) and linear absorption spectrum (solid line). Border colors are the same as the spectra in (k).

2.12 Appendix C: Comments on Energetic Alignment in the KMC model

In our experiments, we are measuring the change in the average energy of the first absorption peak of QDs with excited charge carriers as a function of time. However, in the KMC model, we want to model independent hopping of electrons and holes in the conduction and valence bands, respectively. We thus need a way to relate the modeled charge carrier hopping to the measured change in energy of occupied QDs. Energetic variations in the QD band gap, which arise from size dispersity in the QD ensemble, result in changes to the conduction and valence band positions. Within each band, the average red-shift from the randomly distributed charge carriers in the initial state to the thermalized state is given by

$$\Delta\varepsilon_{\mathrm{CB}} = -\frac{{\sigma_{\mathrm{inh,CB}}}^2}{k_{\mathrm{B}}T}, \quad \Delta\varepsilon_{\mathrm{VB}} = \frac{{\sigma_{\mathrm{inh,VB}}}^2}{k_{\mathrm{B}}T}. \tag{2.8}$$

where $\Delta\varepsilon_{\mathrm{CB}}$ and $\Delta\varepsilon_{\mathrm{VB}}$ are the changes in energy of the conduction and valence bands, and $\sigma_{\mathrm{inh,CB}}$ and $\sigma_{\mathrm{inh,VB}}$ are the inhomogeneous linewidths (standard deviation) of the conduction and valence band energies. The total energy red-shift of the band gap that is observed in the transient absorption measurements is then given by

$$\Delta\varepsilon_{\mathrm{BG}} = \Delta\varepsilon_{\mathrm{CB}} - \Delta\varepsilon_{\mathrm{VB}} = -\frac{{\sigma_{\mathrm{inh,CB}}}^2}{k_{\mathrm{B}}T} - \frac{{\sigma_{\mathrm{inh,VB}}}^2}{k_{\mathrm{B}}T}. \tag{2.9}$$

We now need an expression to relate the conduction and valence band energetic dispersity to the band gap inhomogeneous linewidth (standard deviation), $\sigma_{\mathrm{inh,BG}}$. If we make the effective mass approximation, the conduction and valence bands are symmetric and each band sees half of the band gap energetic dispersity. However, atomistic simulations suggest that energetic variations are actually larger in the conduction band than in the valence band.[42] Thus, we define m as the fraction of the band gap change that occurs in the valence band. The inhomogenous linewidths of the conduction and valence bands are then given by

$$\sigma_{\mathrm{inh,CB}} = (1-m)\sigma_{\mathrm{inh,BG}}, \quad \sigma_{\mathrm{inh,VB}} = m\,\sigma_{\mathrm{inh,BG}}. \tag{2.10}$$

The red-shift of the band gap is then given by

$$\Delta\varepsilon_{\mathrm{BG}} = -\frac{{\sigma_{\mathrm{inh,BG}}}^2}{k_{\mathrm{B}}T}\left((1-m)^2 + m^2\right) = -\frac{{\sigma_{\mathrm{inh,BG}}}^2}{k_{\mathrm{B}}T}(1 - 2m + 2m^2). \tag{2.11}$$

For the case of symmetric conduction and valence bands under the effective mass approximation, $m = 0.5$, and the red-shift is given by

$$\Delta\varepsilon_{\mathrm{BG}} = -\frac{{\sigma_{\mathrm{inh,BG}}}^2}{2k_{\mathrm{B}}T}, \tag{2.12}$$

which gives the largest fitted values of $\sigma_{\mathrm{inh,BG}}$ for a given measured red-shift. If all energetic shifts occur in one band while the other is pinned ($m = 0$ or $m = 1$), then

$$\Delta\varepsilon_{\mathrm{BG}} = -\frac{{\sigma_{\mathrm{inh,BG}}}^2}{k_{\mathrm{B}}T}, \tag{2.13}$$

which gives the smallest fitted values of $\sigma_{\mathrm{inh,BG}}$ for a given measured red-shift. If energetic variations are present in both the conduction and valence bands, but larger in, for example, the conduction band than the valence band, the fitted value of $\sigma_{\mathrm{inh,BG}}$ will be intermediate to these two cases. For this reason, we assume symmetric bands under the effective mass approximation in the main text (and show all fits in Figure 2.15), and show the fits for the other extreme with all energetic variation in one band in Figure 2.16 and give summary figures of the results in Figure 2.17 to give bounds on the inhomogeneous linewidth and the characteristic hopping time.

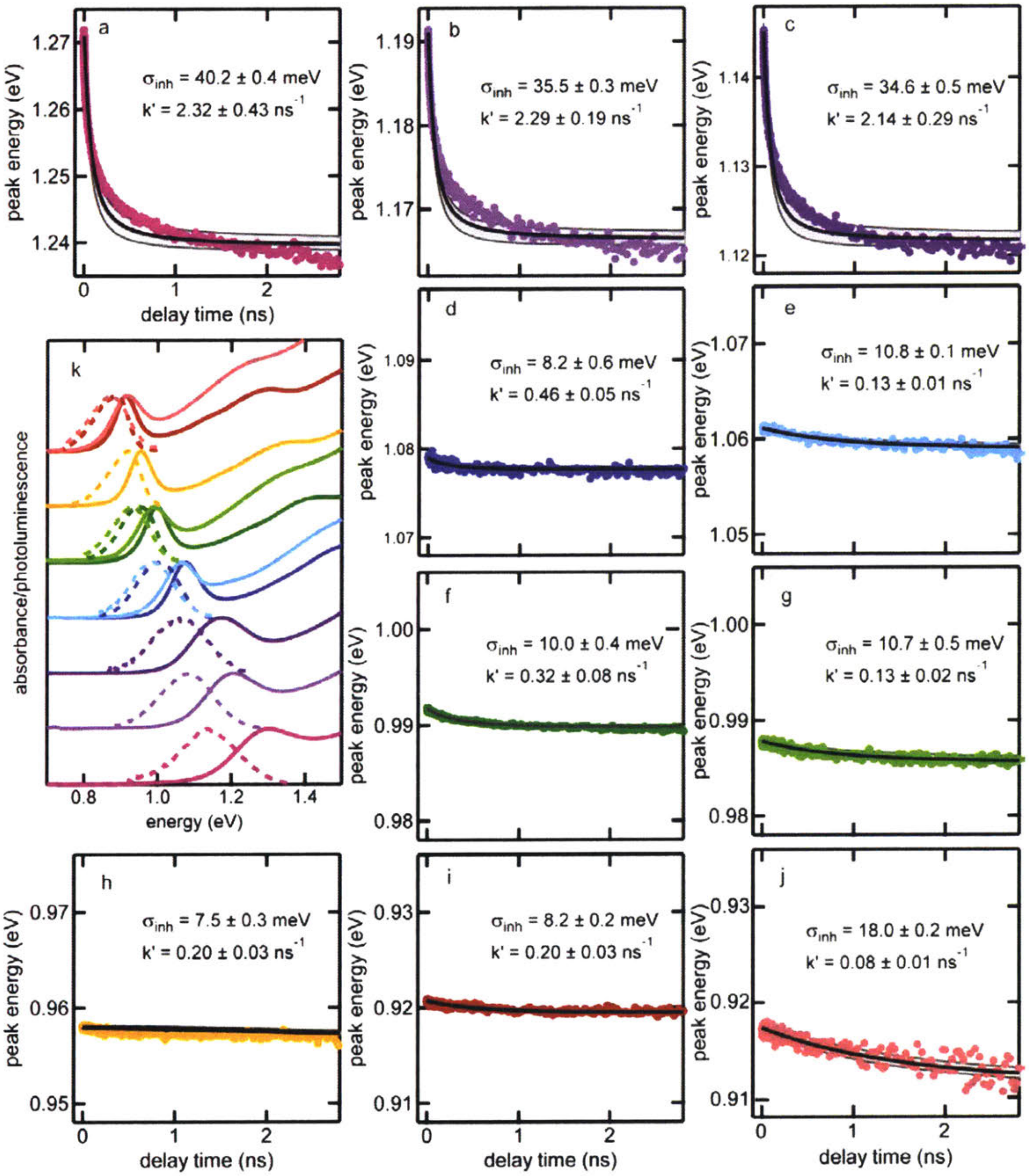

Figure 2.15. (a-j) Kinetic Monte Carlo fits (solid lines) for all samples assuming symmetric conduction and valence bands, with error bounds (shaded gray) and data points shown in same colors as in the solution absorption (solid) and photoluminescence (dashed) spectra in (k).

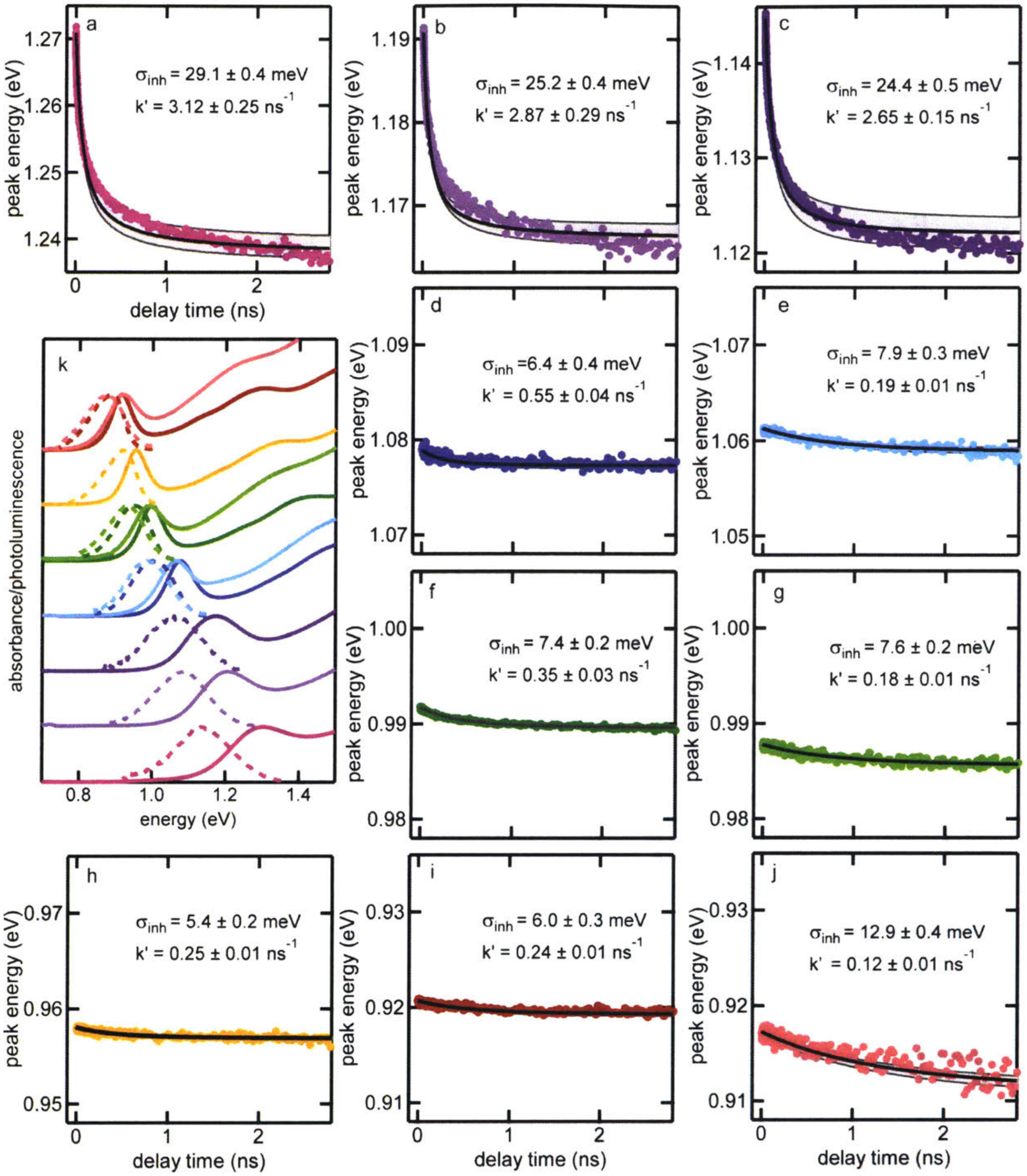

Figure 2.16. (a-j) Kinetic Monte Carlo fits (solid lines) assuming all energetic variation is in one band (could be either conduction band or valence band) for all samples, with error bounds (shaded gray) and data points shown in same colors as in the solution absorption (solid) and photoluminescence (dashed) spectra in (k).

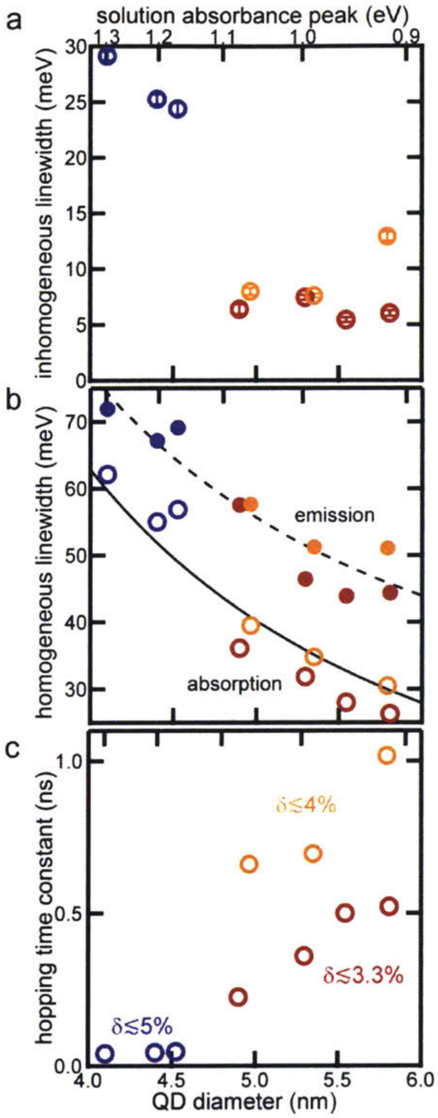

Figure 2.17. The equivalent of Figure 2.5 for fundamental parameters extracted from KMC simulations assuming all energetic variation in one band (conduction or valence band). (a) Inhomogeneous linewidths (standard deviation) of the ten PbS QD samples as found from the fitted energy redshift in the KMC simulations. (b) Homogeneous linewidth (standard deviation) for the absorption (circles) and emission (points) spectra, calculated from the ensemble linewidth and the fitted inhomogeneous linewidth. The solid (absorption) and dashed (emission) lines show the $1/R^2$ scaling expected for homogeneous broadening dominated by deformation-potential coupling to acoustic phonons. (c) Characteristic hopping time, defined as the inverse hopping rate pre-factor adjusted for the number of nearest neighbors in the lattice.

2.13 Appendix D: Discussion of Assumptions about the Superlattice Structure

As mentioned in the main text, for computational efficiency and to reduce the number of model parameters, we restricted charge carrier hopping to nearest-neighbor hopping on a perfectly ordered BCC lattice. Here, we demonstrate that those assumptions are reasonable and more complex models have a very limited effect on the fitting.

The exciton Bohr radius is 20 nm in PbS,[139] so the QDs used in this study experience strong quantum confinement. Under these conditions, variable range hopping may be possible, particularly at lower temperatures.[64, 66] In Figure 2.18a, we allow for this possibility, and compare the results from simulations that allow only nearest neighbor hopping to simulations that allow hopping to QDs that are up to ten times the nearest neighbor distance away. These simulations are done for the smallest QDs studied, which experience the strongest quantum confinement. We find that the two simulations are nearly identical, indicating that nearest neighbor hopping dominates in these solids at room temperature, confirming this assumption of our model.

PbS QDs have been shown to self-assemble in both BCC and FCC superlattices.[50, 140] Our GISAXS patterns in Figure 2.13 suggest that some of our samples may have an FCC structure (Figure 2.13c,g,j). The symmetry of these two superlattices is such that the nearest neighbor distance determined from the first scattering peak is the same for both structures, though the unit cell size and the next-nearest neighbor spacing is different. Since charge carrier hopping is nearest neighbor hopping, we expect the KMC model fit to be the same for the BCC and FCC lattices, as is confirmed in Figure 2.18b. We note that in an FCC lattice each QD has 12 nearest neighbors, while in a BCC lattice, each QD has only 8 nearest neighbors, so while the choice of crystal lattice will not affect the overall fitted charge transfer rate, it will affect the per-QD-pair hopping rate, $k_{i \to j}$. Variations in number of nearest neighbors, particularly if this varies sample-to-sample, may be an important source of noise in the extracted hopping time constant and mobility times presented in Figure 2.5, Figure 2.8, and Figure 2.9.

Based on the GISAXS patterns presented in Figure 2.13, there is clearly some long range disorder in these QD solids. What is less clear is the degree of disorder on the length scales relevant to charge transport in these samples. Charge carriers are only expected to travel a few hundred nanometers in their lifetime, and a much shorter distance in the 3 ns experimental time window used for the fitting. High-resolution SEM images[50] (and Figure 2.1c) indicate that these solids may be highly ordered on the short length scales relevant to the timescales studied here, even if they do not have as much long-range order as shown in the GISAXS patterns.

We considered that heterogeneity in dot-to-dot spacing may play an important role in transport rates, so we also ran KMC simulations with a disordered lattice, shown in Figure 2.18c. The disordered lattice was created by performing a NVT simulation with the Molecular Dynamics software LAMMPS,[141] starting with 16,000 Lennard-Jones (LJ) particles initially in a BCC configuration. The simulation box was enlarged to equilibrate the LJ particles with density $\rho=0.98\rho_{BCC}$ and temperature T=1 in reduced units. The distribution of QD center-to-center spacings in the disordered lattice as compared to a BCC lattice is shown in Figure 2.18d. Using a disordered lattice also requires using a hopping rate equation with a prefactor that is a function of the edge to edge spacing between QDs, as in equation (2) in the main text. For these simulations, we used a value of β=1Å^{-1}.[64] We expected disorder to enhance transport at short time scales,[115] but this effect is very small and within the simulation error, as seen in the inset of Figure 2.18c. While in real samples, disorder will affect the interparticle spacing, the center-to-center distance is fixed based on the GISAXS data in our model, so the impact of a disordered lattice – beyond a change in the average surface-to-surface distance – on the simulated hopping dynamics is minimal.

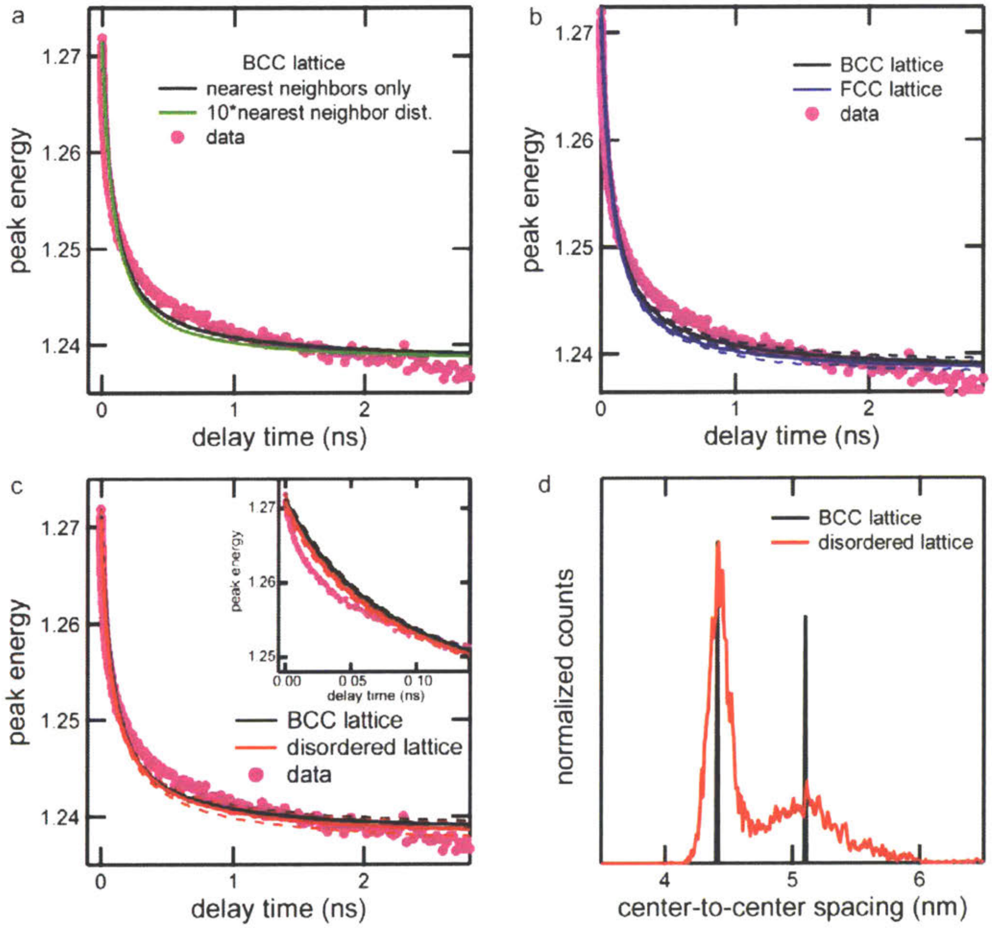

Figure 2.18. (a) KMC simulation with a BCC lattice considering hopping to the 8 nearest neighbors only (black), and with a distance-dependent hopping rate, allowing hopping as far as 10 times the nearest neighbor distance (green). (b) Comparison of KMC simulation with BCC (black) and FCC (blue) lattices. Dashed lines give the standard deviation of 10 simulations. (c) Comparison of KMC simulation with BCC (black) and disordered (red) lattices. A tunneling constant of $\beta = 1$ Å is used to calculate the tunneling rate as a function of edge-to-edge spacing for the disordered lattice.[64] Dashed lines give the standard deviation of 10 simulations. (inset) Zoom in on the fit in the first 140 ps. (d) Distribution of center-to-center spacing for the BCC lattice and the disordered lattice that is derived from a BCC lattice.

Chapter 3 Temperature-Dependent Charge Transport

The basis of this chapter is in preparation for submission as:
R. H. Gilmore, E. M. Y. Lee, K. G. Yager, S. W. Winslow, M. N. Ashner, A. P. Willard, W. A. Tisdale. "Inverse Temperature Dependence of Charge Carrier Hopping in Monodisperse Quantum Dot Solids"

3.1 Introduction

Temperature-dependent measurements are invaluable for identifying charge transport mechanisms present in optoelectronic materials such as QD solids,[52, 64, 66, 68-69, 78-79] organic semiconductors,[142-147] perovskites,[148-149] and transition metal dichalcogenides.[150] Thermally-activated nearest neighbor and variable range hopping mechanisms can be differentiated using temperature-dependent transport measurements.[64, 66, 79] In the strong coupling limit when band-like transport is expected to occur in ordered semiconductor solids, increasing mobility with decreasing temperature as a result of reduced phonon scattering is expected and often presented as conclusive evidence in support of this transport mechanism.[52, 68-69, 78, 150]

Here, we present temperature-dependent transient absorption measurements on coupled QD solids. We extract the transient redshift in the average band gap energy of QDs containing excited charge carriers, and find increasing redshift with decreasing temperature, as expected for thermally activated hopping in an inhomogeneous ensemble. We fit this data with the thermally activated hopping model presented in Chapter 2, holding the inhomogeneous linewidth constant with temperature and fit two hopping rates representing electrons and holes. We find, surprisingly, that the hopping rate, which is ~ $(10\text{ ps})^{-1}$ to $(10\text{ ns})^{-1}$, increases with decreasing temperature, contrary to expected behavior in a thermally activated hopping model. However, including thermal expansion of the QD superlattice in our model can explain this trend. A decrease of 1–2Å in the edge-to-edge spacing as the temperature decreases from 300K to 150K can account for the observed increase in the hopping rate. Grazing-incidence small-angle X-ray scattering (GISAXS) measurements suggest that a superlattice distortion may be responsible for this decrease in edge-to-edge spacing. These results demonstrate that increasing mobility with decreasing temperature can occur within an incoherent site-to-site hopping transport model if the model incorporates both structural and energetic temperature-dependent changes to the QD superlattice.

3.2 Temperature-Dependent Transient Absorption

We fabricate coupled QD solids from three representative QD sizes (4.2 nm, 5.0 nm, and 5.8 nm in diameter, calculated according to a sizing curve[27] from the absorption spectra in Figure 3.1a, with size dispersity of 3.0%, 1.1%, and 1.0% respectively[151]) by spin coating QDs from toluene and ligand exchanging with ethanethiol in a nitrogen glovebox. The samples were loaded into a cryostat in the glovebox and cooled with liquid nitrogen so we could monitor temperature-dependent non-equilibrium charge carrier dynamics using ultrafast transient absorption spectroscopy. The 4.2 nm QDs were excited by a 2.4 eV (520 nm) excitation pulse from a 1 kHz laser system, while the 5.0 nm and 5.8 nm QDs were excited by a 1.85 eV (670nm) excitation pulse from a 100 kHz laser system, resulting in nearly equal excitation probability of all QDs with a density of 0.03-0.1 photons absorbed per QD per pulse (~10^{13} photons/cm^2). Following hot carrier relaxation in 1-2 ps, we monitored the band edge charge carrier population over a 3 ns delay time using a broadband infrared probe (see Section 3.9 for additional details). The absorption bleach of the $1S_h$-$1S_e$ transition in PbS QDs is linearly proportional to the charge carrier population in both the $1S_h$ and $1S_e$ levels, but the peak bleach energy may shift with time as discussed in detail in Chapter 2 and shown in Figure 3.1b for the 4.2 nm QDs at 300 K. As in our previous work[151] described in Chapter 2, we fit a Gaussian to the transient absorption bleach at each time delay to extract the average band gap energy of QDs with excited charge carriers as a function of time following the excitation pulse.

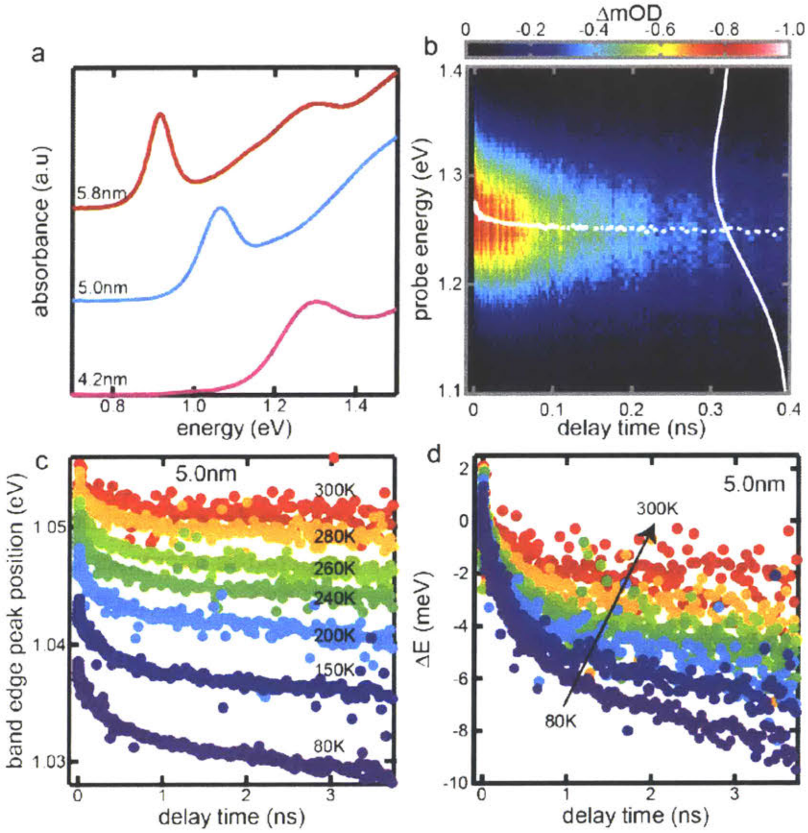

Figure 3.1. Transient absorption peak bleach redshifts for as a function of sample temperatures. (a) Linear absorbance spectra of the three QD ensembles used in this study. (b) Transient absorption color plot for 4.2 nm QDs at 300 K (c) Bleach peak energy as a function of time for several temperatures (labeled on graph) for the 5.0 nm QDs. (d) The data in panel (c) plotted as a change in peak energy relative to the energy at zero delay time. The colors used for each temperature are consistent with panel (c).

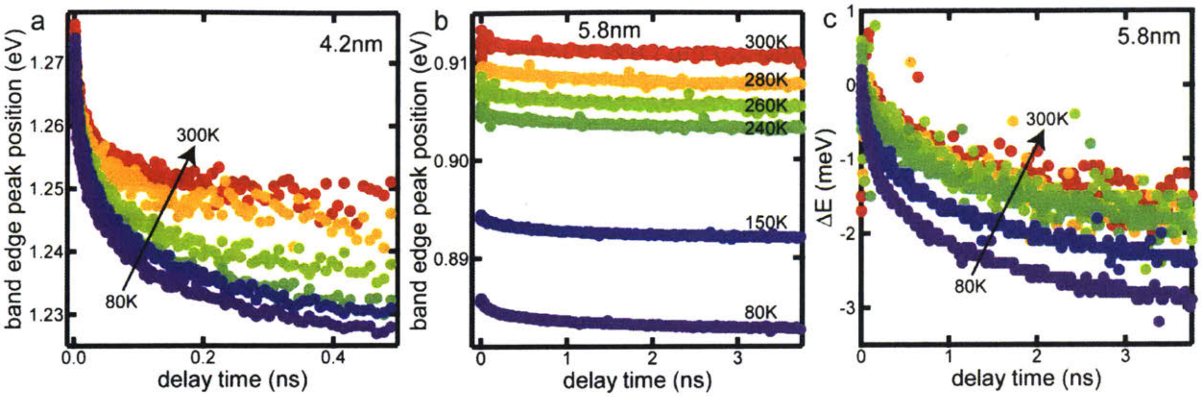

Figure 3.2. Transient absorption peak bleach redshifts for 4.2 nm (a) and 5.8 nm (b) QDs as a function of temperature. The data in panel (b) is plotted as a change in peak energy relative to the energy at zero delay time in (c). The colors used for each temperature are consistent across the panels.

The band edge bleach peak position as a function of delay time at several sample temperatures is shown in Figure 3.1c for the 5.0 nm QD solid and in Figure 3.2a,b for the 4.2 nm and 5.8 nm QD solids. The PbS QD band gap is temperature-dependent, and the magnitude of the shift with temperature depends on the QD size (Figure 3.2), so the starting bleach position for uniformly excited QDs is a function of temperature (Figure 3.1c). For small QDs, the band gap blueshifts with decreasing temperature. For the 4.2 nm QDs studied here, the band gap is approximately constant, redshifting by only a few meV with decreasing temperature (Figure 3.3a). Larger QDs have a band gap that redshifts with decreasing temperature (Figure 3.3b), with the magnitude of the redshift increasing as the QD size increases.[152] We also note that the QD absorption cross section appears to increase with decreasing temperature, as indicated by a stronger band edge peak in the linear absorption (Figure 3.2) and a larger magnitude transient bleach signal in transient absorption experiments.

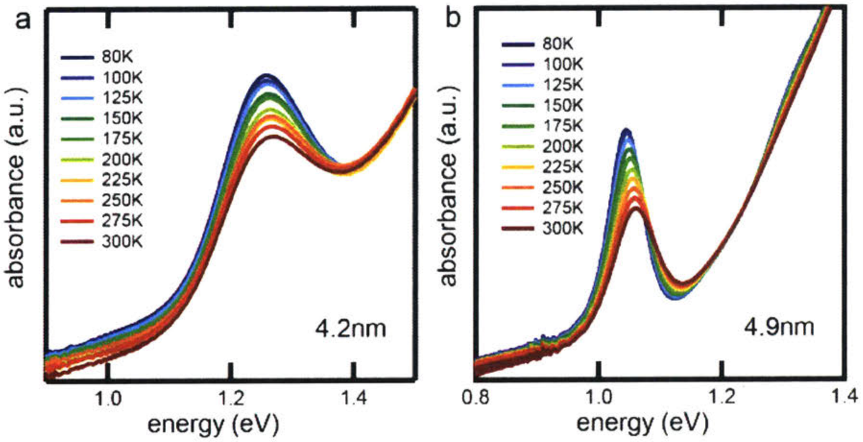

Figure 3.3. Linear absorption spectra as a function of temperature for 4.2 nm and 4.9 nm QDs.

To facilitate analyzing the transient redshift as a function of temperature, we replot the band edge peak position data for the 5.0 nm QDs (Figure 3.1c) and 5.8 nm QDs (Figure 3.2b) as the change in the peak bleach position energy relative to peak bleach energy at zero delay time between the excitation pulse and probe in Figure 3.1d and Figure 3.2c. We observed that the magnitude of the transient redshift increases with decreasing temperature for all QD sizes, confirming the applicability of a thermally activated hopping transport model in a QD solid with inhomogeneously distributed energy states.[114] Within this model, the hops that drive charge carrier diffusion proceed preferentially to QDs with smaller band gaps, while hops to QDs with larger band gaps are slower by a Boltzmann factor, $\exp(-\Delta\varepsilon/k_BT)$, that accounts for the energy difference, $\Delta\varepsilon$, between the two states (equation (2.1)). Thus the average charge carrier energy redshifts as the system propagates from the initial state with randomly distributed charge carriers towards a thermally equilibrated state. In the thermalized state, the excited charge carrier distribution reflects a Boltzmann distribution convolved with the inhomogeneously broadened density of states, so the average charge carrier energy is expected to decrease with decreasing temperature, as is observed experimentally (Figure 3.1 and Figure 3.2).

3.3 Pauli Master Equation Approach to Data Fitting

To simulate our data, we switch from using kinetic Monte Karlo, in which stochastic sampling of many possible charge carrier trajectories is required to build up robust statistics, to the Pauli master equation approach, in which the system rate matrix is used to propagate the ensemble distribution in time and deterministically calculate the charge carrier population dynamics. The charge carrier hopping from QD to QD is given by[153]

$$\frac{d}{dt}P_i(t) = \sum_{j\neq i} k_{ji}P_j - \sum_{j\neq i} k_{ij}P_i \tag{3.1}$$

where P_i is the charge carrier probability density on QD i, and k_{ij} is the charge carrier hopping rate from QD i to QD j (as given in equation (2.1) and (2.2)). The first term represents the total hopping rate to QD i from all other QDs (generation of charge carriers on QD i), and the second term is the total hopping rate from QD i (consumption of charge carriers on QD i). Equation (3.1) can be generalized for a superlattice with N QDs,

$$\frac{d}{dt}\mathbf{P}(t) = -\mathbf{M}\mathbf{P}(t) \tag{3.2}$$

where $\mathbf{P}(t)$ is the charge carrier probability for all N sites and $\mathbf{M}$ is the transition rate matrix with diagonal and off diagonal elements given by $M_{ii} = \sum_{j\neq i} k_{ij}$ (the total hopping rate from QD i) and $M_{ij} = -k_{ji}$.

If the transition rate matrix is constant with time, equation (3.2) is an initial value problem with the solution

$$\mathbf{P}(t) = e^{-\mathbf{M}t}\mathbf{P}(0) = \sum_{i=1}^{N} c_i e^{-\lambda_i t}\mathbf{v}_i \tag{3.3}$$

where **P**(0) is the initial excitation distribution, which is taken to be a uniform distribution across all QDs for our simulations, $\mathbf{v}_i$ are the eigenvectors corresponding to eigenvalues λ_i of **M**, and constants c_i are the solution to **P**(0)=**Vc** where **V** is a matrix with columns $\mathbf{v}_i$. The average band gap energy of QDs with excited charge carriers as a function of time, $\langle E(t)\rangle$, is calculated as

$$\langle E(t)\rangle = \boldsymbol{\varepsilon}\mathbf{P}(t) \tag{3.4}$$

where ε is a row vector containing the band gap energies of the N QDs in the superlattice. The master equation improved the simulation accuracy by eliminating KMC error and greatly reduced the computational power required to fit the data, facilitating globally fitting data at all temperatures for each sample. The calculation of mobility and diffusivity is more complicated using the master equation, so KMC simulations are still used to gain this spatial information about charge transport.

3.4 Temperature-Dependent Hopping Rates Based on Previous Model

We now implement the master equation to fit the charge carrier hopping model described in Chapter 2 to the temperature dependent TA data presented in Figure 3.1 and Figure 3.2. A QD solid with an ordered body-centered cubic (BCC) QD superlattice is generated and each QD is randomly assigned a band gap energy drawn from a Gaussian with mean $\bar{\varepsilon}$ and standard deviation σ_{inh}. The inhomogeneous linewidth, σ_{inh}, may be a function of temperature because the change in the QD band gap with temperature is a function of QD size.[152] The band gap of the largest QDs in the ensemble with the lowest energy band gaps will redshift more with decreasing temperature than the band gap of the smaller QDs with greater band gaps, increasing the inhomogeneous broadening. We estimated the magnitude of this increased inhomogeneous broadening with decreased temperature[152] and found that $d\sigma_{\text{inh}}/dT$ is -2.5 μeV/K for the 5.8 nm QDs, -3.6 μeV/K for the 5.0 nm QDs, and -8.9 μeV/K for the 4.2 nm QDs. This energy shift is 0.5, 0.8, and 1.9 meV for the three QD sizes, which is 4-5% of the room temperature inhomogeneous linewidth (Figure 2.15). This change in the inhomogeneous linewidth with temperature is similar in magnitude to the uncertainty on the inhomogeneous linewidth, so we neglect this change in the model and fix a single value of the inhomogeneous linewidth for each QD ensemble.

The inhomogeneous broadening is assumed to be split evenly between symmetric conduction and valence bands, and two hopping rates, one for electrons and one for holes, are fit using the Miller-Abrahams rate equation for the hopping rate from QD i to QD j

$$k_{ij} = \begin{cases} k' \exp\left(-\dfrac{(\varepsilon_j - \varepsilon_i)/2}{k_{\mathrm{B}}T}\right); & \varepsilon_j > \varepsilon_i \\ k'; & \text{otherwise.} \end{cases} \tag{3.5}$$

where ε_i and ε_j are the band gap energies of QD i and QD j, k_B is the Boltzmann constant, and T is the temperature. The two hopping rate prefactors, k_1' and k_2', are fit for electron and hole transport at each temperature, though we cannot say from this model which is for electrons and which is for holes.

At low temperatures, we must consider not just free electrons and holes, but also bound excitons. Exciton dissociation in PbS QD solids is a thermally activated process.[55-56] Nearly all charge carriers are free carriers near room temperature. At low temperatures, there is insufficient thermal energy to overcome the exciton binding energy, so a majority of charge carriers remain as bound excitons and do not dissociate into free carriers. At intermediate temperatures, both excitons and free charge carriers will be present. We estimate the fraction of dissociated carriers from the photoluminescence intensity as a function of temperature as shown in Figure 3.4a. Charge carriers are mostly excitons at 80 K, so we do not fit this data with our free carrier hopping model. For higher temperatures, we consider the impact of exciton transport on the observed carrier dynamics, though the fraction of excitons is less than 5% for temperatures 240 K and above. The exciton hopping rate is given by Förster resonant energy transfer (FRET), rather than tunneling. The exciton lifetime is 1-2 μs and the Förster radius is 8 nm[58] to 12 nm,[59] so the FRET hopping time is tens of nanoseconds (equation (1.3)). This FRET hopping time is an order of magnitude longer than the delay times used in our experiments, so excitons are essentially stationary within the time window of our experiment, and we therefore assume that the average exciton energy remains at the average QD band gap energy throughout our experiments.

The simulated transient redshift of the average band gap of QDs with excited charge carriers is calculated as

$$\langle E(t)\rangle = (1 - f_{diss})E(t = 0) + f_{diss}\,(\langle E_1(t)\rangle + \langle E_2(t)\rangle)/2 \tag{3.6}$$

where f_{diss} is the fraction of dissociated charge carriers, $E(t = 0)$ is the average band gap of QDs in the ensemble (because all QDs are excited with equal probability), and $\langle E_1(t)\rangle$ and $\langle E_2(t)\rangle$ are the average band gap energies of QDs with excited charge carriers calculated according to equation (3.4) for hopping in the conduction and valence bands according to equation (3.5) with prefactors k_1' and k_2'. This simulated transient redshift is fit to the experimental transient redshifts at temperatures from 150 K to 300 K and the results are shown in Figure 3.4b-d. A single inhomogenous linewidth, σ_{inh}, is fit for each QD ensemble, while the hopping rate prefactors, k_1' and k_2', are fit at each temperature.

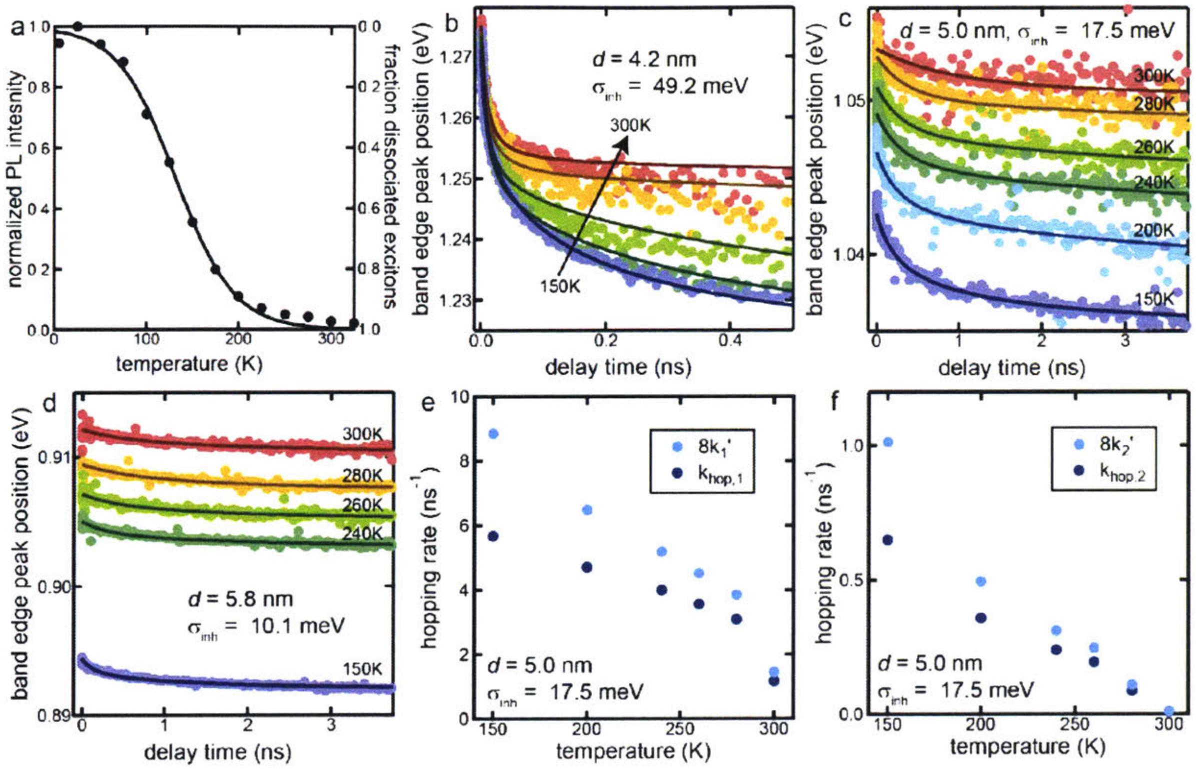

Figure 3.4. Fits based on model from Chapter 2. (a) Normalized photoluminescence intensity is used to estimate the fraction of dissociated excitons as a function of temperature. (b-d) Model fit to data at each temperature for the 4.2 nm (b) 5.0 nm (c), and 5.8 nm (d) QD solids. The colors used for each temperature are consistent throughout the figure. (e-f) Fitted hopping rates as a function of temperature for the 5.0 nm QD solids.

The charge carrier hopping model appears to fit the data well for all three QD sizes. However, the hopping rate prefactors, $k_1{}'$ and $k_2{}'$, do not show the expected temperature dependence (Figure 3.3e-f). We expected to see thermally activated behavior in the hopping rate prefactors with activation energy equal to the charging energy, resulting in a linear, negative slope equal to the charging energy when $\ln k'$ is plotted against inverse temperature. However, the fitted hopping rate prefactors instead increase with decreasing temperature, opposite to the expected trend for thermally activated hopping. We also compare the total thermalized hopping rate of charge carriers in the QD solid, k_{hop}, which includes the Boltzmann factor with the energy difference between neighboring QDs, and therefore might be expected to decrease with decreasing temperature as expected for thermally-activated hopping. However, we find that the total hopping rate also increases with decreasing temperature (Figure 3.3e-f).

The diffusivity and mobility are proportional to the hopping rate, so increasing total hopping rate with decreasing temperature implies that diffusivity and mobility will increase as well. This is a very surprising trend because the hopping rates in these QD solids are many picoseconds to several nanoseconds, which is too slow for band-like transport when $d\mu/dT < 0$

is expected.[68] Rather, we have a system in which the thermalized population energetic distribution, given by the magnitudes of the average energy redshifts, is consistent with a thermally-activated hopping model, but the kinetics are not. In a thermally-activated hopping model, the hopping rate should be slower at low temperatures, so the redshift of the average band gap energy of a QD with excited charge carriers should be slower as well. However, even the data in Figure 3.1d and Figure 3.2 clearly shows that the lower temperature measurements redshift faster for all QD sizes. Since the thermodynamics in these QD solids matches a thermally-activated hopping model, but the kinetics do not, we conclude that we are missing a fundamental physical process that impacts $k'(T)$. Since these QDs have low size dispersity and thus relatively little energetic disorder, we examine the structural order and possible structural changes in the QD superlattice to understand the temperature-dependent hopping rate.

3.5 Global Fitting Model Predicts Superlattice Contraction

As we saw with the impact of size dispersity on superlattice structure in Chapter 2, small changes in the interparticle spacing can have a large effect on the charge carrier tunneling rate. Most solid material contract in volume with decreasing temperature, so one might expect QD solids to do so as well. In fact, lattice contraction has been observed in gold nanoparticle solids.[154] We therefore propose a form for the hopping rate prefactor that includes both the thermally activated component from the charging energy and the edge-to-edge distance-dependent tunneling rate,

$$k'(T) = k_0 \exp\left(\frac{-E_C}{k_B T}\right) \exp\left(-\beta l(T)\right) \tag{3.7}$$

where k_0 is a temperature-independent constant, k_B is the Boltzmann constant, T is the temperature, and β is the tunneling constant taken to be 1.1 Å^{-1}.[71] The charging energy, E_C, is estimated from the charging energy of a sphere and is given by[66-67]

$$E_C = \frac{0.35e^2}{4\pi\varepsilon\varepsilon_0 d} \tag{3.8}$$

where e is the elemental charge, ε is the dielectric constant of the QD solid, ε_0 is the vacuum permittivity, and d is the QD diameter. The charging energy for our QDs is calculated to be 8.7 meV for the 4.2 nm QDs, 7.3 meV for the 5.0 nm QDs, and 6.3 meV for the 5.8 nm QDs. We assume linear temperature dependence for the edge-to-edge spacing, l, given by

$$l(T) = l(300K) - c(300K - T) \tag{3.9}$$

where c is a fitting constant that gives the decrease in edge-to-edge spacing per degree Kelvin of temperature decrease.

Thus, we fit a global hopping transport model with four fitting parameters, the inhomogeneous linewidth σ_{inh}, two temperature-independent prefactor constants for hopping in the conduction and valence bands $k_{0,1}$ and $k_{0,2}$, and the change in edge-to-edge spacing with temperature *c*, to the transient redshifts at all temperatures for each QD solid. These fits are shown in Figure 3.5a-c. The total hopping rates and hopping rate prefactors given by equation (3.7) for the three QD sizes are plotted in Figure 3.5e-j. In all cases the prefactor increases with decreasing temperature, and for the medium and large QDs, the total hopping rate does as well. In the smallest QDs with largest size dispersity, the total hopping rate initially increases and then decreases as the temperature is decreased and there is insufficient thermal energy to overcome the inhomogeneous broadening in the ensemble.

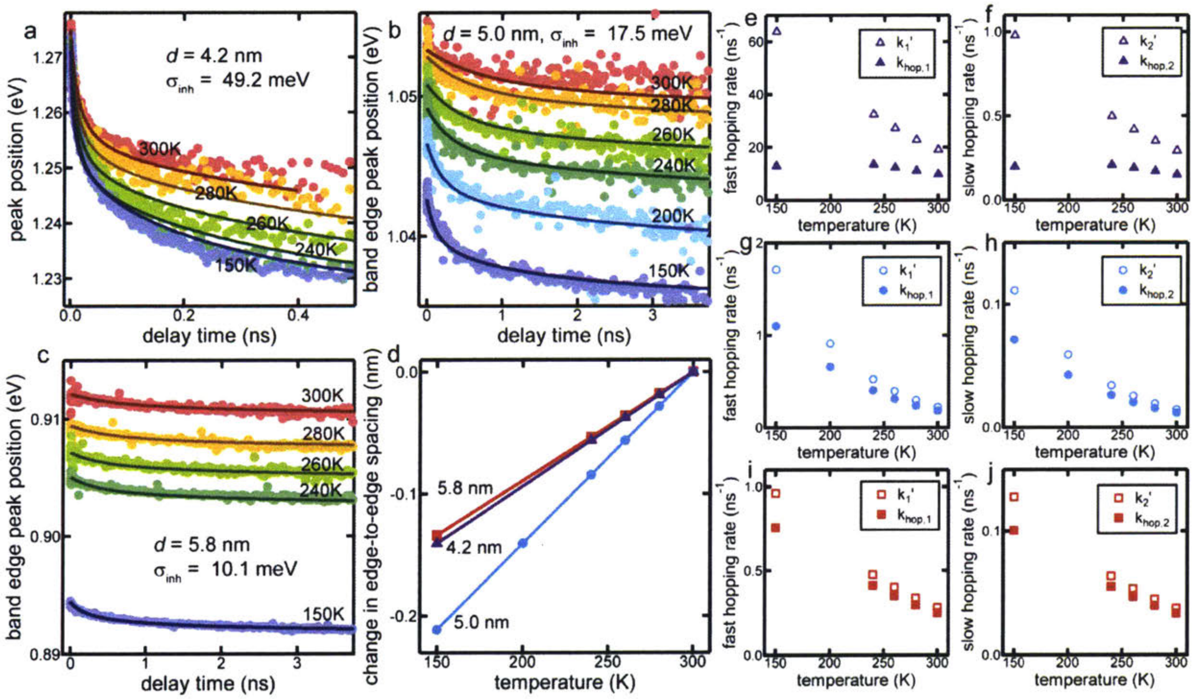

Figure 3.5. Fits with the global hopping model for the 4.2nm (a), 5.0 nm (b), and 5.8 nm (c) QD solids. (d) Predicted change in edge to edge spacing based on the model. (e-j) Fitted hopping rate prefactors (open symbols) and per QD pair total hopping rates (closed symbols) for the 4.2 nm (e-f), 5.0 nm (g-h), and 5.8 nm (i-j) QDs.

The global fit gives a prediction for the superlattice contraction with decreasing temperature for each of the QD solids. The fitted rates for the decrease in edge-to-edge spacing are 0.94 pm/K for the 4.2 nm QDs, 1.42 pm/K for the 5.0 nm QDs, and 0.89 pm/K for the 5.8 nm QDs. These contraction rates predict a decrease of 1.5 – 2 Å in the edge-to-edge spacing when the temperature decreases from 300 K to 150 K (Figure 3.5d). The expected decrease in QD diameter based on the thermal expansion coefficient of PbS is an order of magnitude smaller and therefore negligible.[155] GISAXS measurements for these QD solids give the center-to-center spacing for these QD solids as 4.4 nm, 5.5 nm, and 5.9 nm for the small, medium, and large QDs (Figure 2.13). If the QD diameter is calculated based on a sizing curve that assumes spherical QDs,[27] this center-to-center spacing gives nominal edge-to-edge spacing of 0.1 – 0.5 nm for these samples. However, real QDs are faceted. In ordered superlattices of monodisperse QDs like those we have here, the facets are often oriented towards each other in QD solids,[51] decreasing the relevant QD diameter and increasing the calculated edge-to-edge spacing. The effects of faceting on the actual distance from the center of the QD to the middle of a facet are shown in Figure 3.6 (calculations to obtain this figure are shown in Section 3.10). The relevant diameter for calculating edge-to-edge spacing from the center-to-center spacing can be 10-15% less than the diameter of a sphere with equivalent volume. If we assume a truncated octahedron shape that gives a relevant QD diameter that is 12.8% less than the equivalent spherical QD diameter,[51] we calculate edge-to-edge spacing of 0.74 nm, 1.14 nm, and 0.84 nm for the small, medium, and large QDs at 300 K. Compared to these interparticle distances, a change in the edge-to-edge spacing of 0.1 – 0.2 nm represents a decrease of 15-20% over a 150 K temperature change.

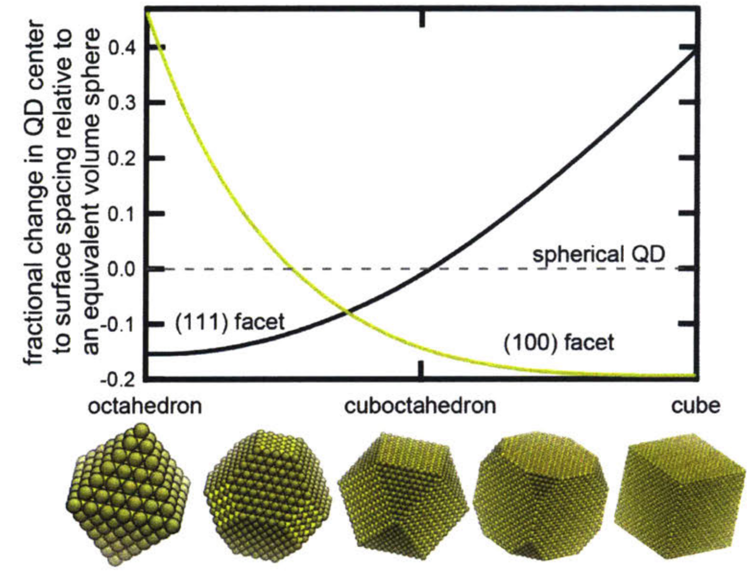

Figure 3.6. The effect of QD shape on the relevant QD diameter for charge transfer.

3.6 GISAXS Reveals Superlattice Distortion with Decreasing Temperature

Grazing-incidence small-angle X-ray scattering (GISAXS) experiments confirm that lattice distortion upon cooling results in a nearest neighbor separation reduction. GISAXS patterns were collected cooling from 298 K to 133 K using a separate batch of 5.7 nm diameter oleic acid capped QDs without ligand exchange. Figure 3.6a,b show the initial and final scattering patterns. Indexing the peaks[156] reveals a lattice distortion in which an initial face-centered cubic (FCC) lattice expands along the *a* and *b* axes while contracting along the *c* axis. The resulting superlattice is a body-centered tetragonal (BCT) lattice with a reduction of 5.2 Å in nearest neighbor spacing overall (Figure 3.7c). Oleic acid ligands are longer than the ethanethiol ligands used in the TA experiments. We expect the reduction in neighbor spacing upon distortion to be smaller in these superlattices but nonetheless significant. Attempts at capturing a similar distortion using ethanethiol ligand-exchanged QDs were unable to differentiate between lattice types due to lack of higher-order scattering peaks. An analogous projected distortion consistent with the observed GISAXS peaks yields a reduction of 1.4 Å in nearest neighbor spacing (Figure 3.8, details in Section 3.11), matching the contraction predicted from the hopping model.

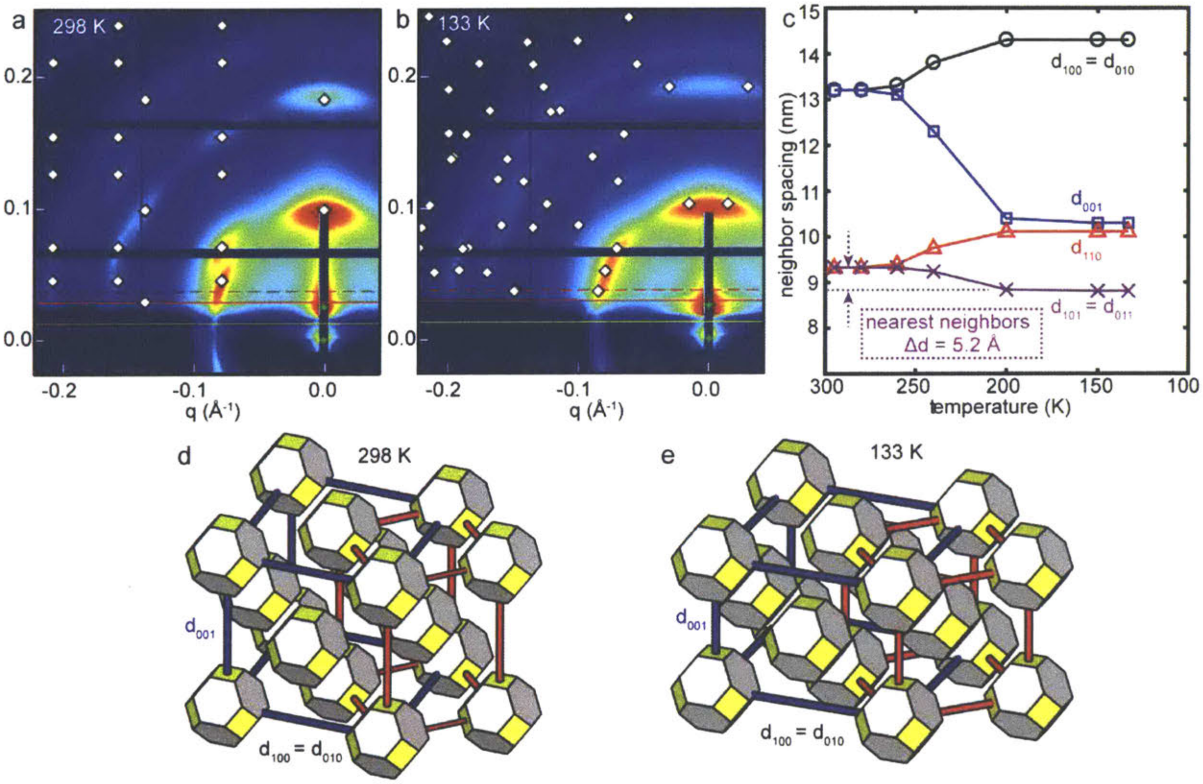

Figure 3.7. Temperature-dependent lattice distortion of an ordered superlattice of 5.7 nm QDs with oleic acid ligands. (a) GISAXS patterns at 298 K showing a face-centered cubic lattice and (b) 133 K showing a body-centered tetragonal lattice. (c) Change in neighbor center-to-center spacings with temperature for *a* and *b* axes (black, open circles), *c* axis (blue, open squares), d_{110} direction (red, open triangles), and nearest neighbors (purple crosses). (d, e) Schematics showing the superlattice distortion as a function of temperature with FCC unit cell (blue) and BCT unit cell (red).

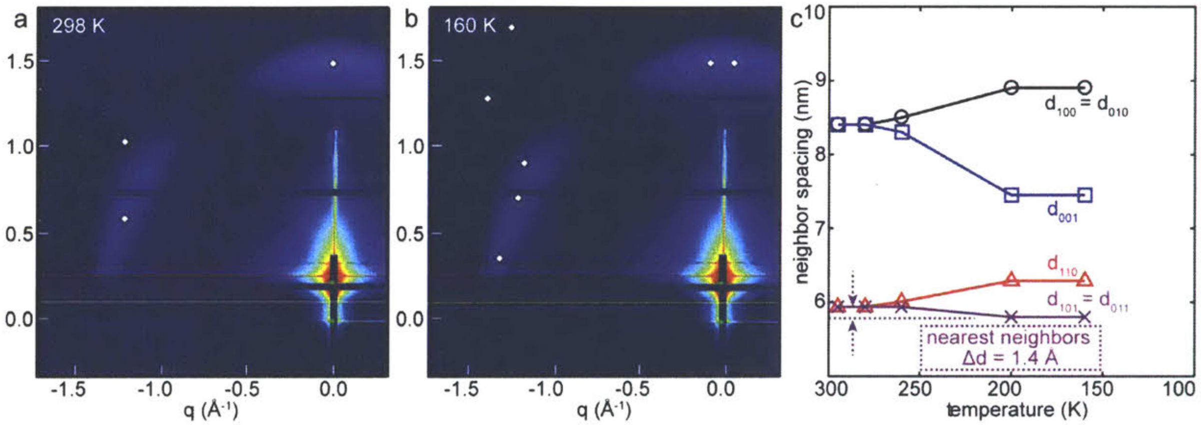

Figure 3.8. Temperature-dependent lattice distortion of an ordered superlattice of 5.0 nm QDs with ethanethiol ligands. (a) GISAXS patterns at 298 K with expected FCC diffraction peak positions and (b) 160 K with expected BCT peak positions based on the lattice distortion model described in the text. (c) Change in neighbor center-to-center spacings with temperature for *a* and *b* axes (black, open circles), *c* axis (blue, open squares), d_{110} direction (red, open triangles), and nearest neighbors (purple crosses).

3.7 Increasing Mobility with Decreasing Temperature

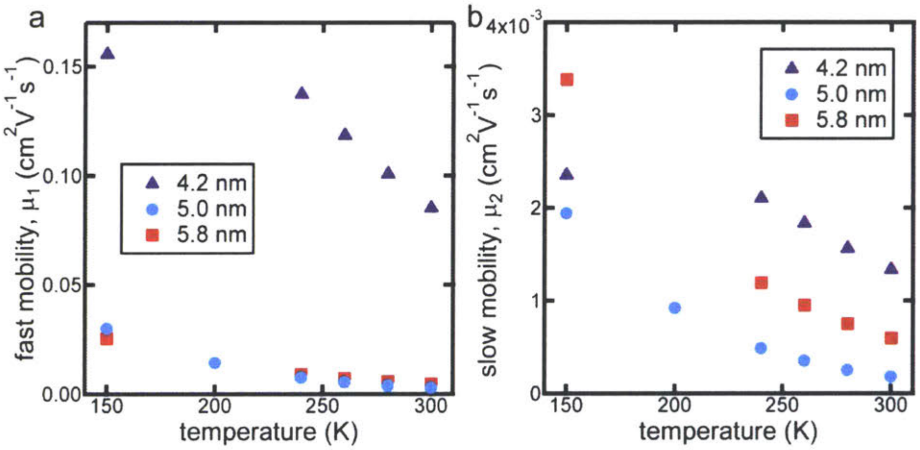

Figure 3.9. Calculated mobility from KMC simulations based on the global hopping model fit for the fast (a) and slow (b) hopping rates.

We then use kinetic Monte Carlo model simulations (similar to those presented in Chapter 2) with the fitted inhomogeneous linewidth and hopping rates from the global hopping model to simulate charge carrier hopping trajectories. We monitor the mean squared displacement and calculate the diffusivity and mobility as a function of temperature (as in Section 2.7 for room temperature data). The mobilities calculated for the fast and slow hopping rates are plotted in Figure 3.9. The observed increasing mobility with decreasing temperature in all three QD solids is surprising for charge transport in the hopping regime. The low size dispersity in our QD solids makes the Arrhenius contribution to the hopping rate small and enabled the observation of this surprising result. We attribute the increasing mobility to reduced interparticle spacing as a result of superlattice contraction at low temperatures.

Increasing mobility with decreasing temperature is expected for band-like transport, as occurs in bulk semiconductors. However, whether demonstrating $d\mu/dT < 0$ is sufficient evidence to claim the observation of band-like transport is the subject of significant debate.[68, 79] It has previously been suggested that hopping transport with low activation energy, *Ea*, can give $d\mu/dT < 0$ at higher temperatures because of the temperature dependence of prefactor in the hopping mobility expression that is derived from Einstein's relations between diffusivity and mobility,

$$\mu_{hop} = \frac{ed^2E_a}{3hk_BT}\exp\left(-\beta l - \frac{E_a}{k_BT}\right) \tag{3.10}$$

where e is the unit charge, d is the center-to-center distance between QDs, and h is Plank's constant.[79] Here, we show that the nearest neighbor edge-to-edge spacing, l, may also be a function of temperature, so the observation of $d\mu/dT < 0$ for hopping transport may extend to lower temperatures, depending on the lattice transformations present. We emphasize that the transient redshift and relaxation of charge carriers into lower energy states observed in the TA measurements this work is characteristic of hopping transport between localized states, and means these samples do not experience band-like transport, in which charge carriers would be expected to maintain a constant energy during transport. We also note that the highly monodisperse QD ensembles that might be expected to show band-like transport are also most likely to have small activation energies so that temperature-dependent structural changes or the temperature-dependent mobility prefactor are more likely to dominate the overall temperature-dependent mobility trend. Thus, showing $d\mu/dT < 0$ alone is supporting but not sufficient evidence for band-like transport and some additional evidence is needed.

While $d\mu/dT < 0$ is possible in the hopping transport regime, the high mobility exceeding 10 $cm^2V^{-1}s^{-1}$ that has been reported for QD solids showing possible band-like transport[52, 69] approaches theoretical limits for hopping transport.[79] Additionally, some reports showing high mobility and $d\mu/dT < 0$ use inorganic ligands such as thiocyanate[69] or molecular metal chalcogenides,[52] and it is unclear if these QD solids would be subject to lattice distortions similar to those observed here for QD solids with organic ligands. Amine treatment strips lead oleate from the surface of PbSe QDs,[157] leading to epitaxially connected superlattices with high mobility and an activation energy for transport that is inversely proportional to the excitation density and approaches band-like transport at high fluence.[78] Epitaxially connected QDs retain defined absorption peaks that redshift by only a few meV relative to unattached QDs,[78, 158] which is similar to the optical properties of other QD solids exhibiting possible band-like transport.[52, 69] Thus, retaining the excitonic peaks does not prove the absence of sintering, and it is possible that the large mobilities in these QD solids arise as a result of delocalized transport through networks of attached particles.

Regardless of whether QD solids are made of individual particles or attached superlattices, samples showing high mobility and inverse temperature dependence must also show some more direct measure of the extent of charge carrier delocalization to convincingly claim band-like transport. Various methods, including cross-polarized transient grating spectroscopy,[81] low temperature resistance and magnetotransport measurements,[82] and the transition from nearest neighbor hopping to variable-range hopping,[83] have been used to estimate the charge carrier localization length. Since carrier localization lengths of only a few times the QD diameter have been measured to date,[81-83] it seems unlikely that band-like transport has been observed. Instead, in monodisperse QD solids, the temperature-dependence of the spatial structure (interparticle spacing) may dominate over that of the energetic structure (thermally-activated Arrhenius dependence on the charging energy and inhomogeneous broadening). If the relative contributions of the structural and energetic components vary as a function of temperature, the mobility may initially increase and then decrease as a function of temperature, as has been observed experimentally.[69]

3.8 Conclusions

We have shown that incoherent nearest neighbor hopping transport in QD solids can result in increasing mobility with decreasing temperature. Temperature-dependent transient absorption spectroscopy confirmed that charge carriers thermalize on lower energy QDs within the ensemble as the temperature decreases. However, the rate at which they move to this pseudo equilibrium does not follow the expected thermally-activated behavior, but instead increases with decreasing temperature. This surprising trend is explained by a predicted 1.5 – 2 Å contraction of the PbS QD superlattice with decreasing temperature. GISAXS measurements on ordered QD solids with oleic acid ligands show a lattice distortion that supports this contraction when extrapolated to ethanethiol-capped QD solids. These results showing increased mobility with decreasing temperature for hopping transport in monodisperse QD solids have important implications for analyzing experiments that attempt to achieve band-like transport in QD solids.

3.9 Experimental Methods

PbS QD Synthesis and QD Solids Preparation. The 4.2 nm PbS quantum dots were synthesized according to Zhang *et al,*.[37] and the 5.0 nm, 5.7 nm and 5.8 nm batches according to Weidman *et al.*[27] Purified QDs were re-dispersed in toluene at a concentration of 100 mg/mL in a nitrogen glovebox. 40 μL of the solution was spun at 1500 rpm for 30 s onto a 0.5 in square borosilicate glass slide (Schott D-263 from Thermo Fisher) that had been cleaned and treated overnight in a 0.02M (3-mercaptopropyl)trimethoxysilane (Sigma-Aldrich, 95%) solution in toluene to improve QD adhesion. The sample was then placed in a 0.1M solution of 1-ethanethiol (Sigma-Aldrich, 97%) in acetonitrile for 24 hours for ligand exchange, and then rinsed with pure acetonitrile to remove excess ethanethiol. This created films with an optical density of about 0.1 at the first absorption peak. Prior to ligand exchange, these QDs are air stable,[27] and following ligand exchange, the samples were kept in an inert atmosphere at all times. The cryostat was loaded in the glovebox for TA measurements, and care was taken to avoid oxygen exposure when pumping down. The cryostat was pumped down to a pressure of 10^{-5} Torr before cooling with liquid nitrogen for temperature-dependent TA measurements.

Transient Absorption Spectroscopy. Transient absorption spectroscopy on the 4.2 nm QDs was performed at the Advanced Optical Spectroscopy and Microscopy Facility at the Center for Functional Nanomaterials at Brookhaven National Laboratory on the setup described in Section 2.9. For the femtosecond transient absorption experiments on 5.0 and 5.8 nm QDs, the 1040 nm output from a high repetition-rate Yb amplifier (Spectra-Physics) operating at 100 kHz was split into two beams. One arm was used to generate a 670 nm pump pulse using a commercial non-collinear optical parametric amplifier (Light Conversion). The other arm was used to generate a broadband probe pulse 1050-1600 nm by focusing the 1040 nm fundamental into a 10 mm YAG window. The pump pulse was compressed to ~50 fs FWHM using a fused silica prism compressor, sent through a mechanical delay stage (Newport) to control the pump-probe delay, and focused into a mechanical chopper (ThorLabs) to modulate the pump at 4 kHz. The pump and probe beams were focused by a concave mirror into the sample mounted in a crysostat, and the probe beam was coupled into a spectrometer with a high-speed data acquisition system (Ultrafast Systems) to collect spectra at 8 kHz. The acquisition and chopping were synchronized with the amplifier repetition rate to ensure a consistent number of laser pulses per spectrometer acquisition. Each measurement was the average of at least 4 scans with 1s acquisition per time point to ensure that dynamics did not change under laser exposure. Pump powers were a few mW to give similar pump pulse energy to the 1kHz laser system TA experiments.

Grazing-Incidence Small-Angle X-ray Scattering. GISAXS on the 5.7 nm oleic acid QDs and 5.0 nm ethanethiol QDs were performed at the Coherent Hard X-ray (CHX/11-ID) beamline of the National Synchrotron Light Source II (NSLS-II). The X-ray source is an undulator. A Si(111) double-crystal monochromator was used, yielding an energy resolution of $\Delta E/E = 0.01\%$. The 5.7 nm QDs were measured at a wavelength of 0.885 Å. The 5.0 nm QDs were measured at wavelength of 0.969 Å. The sample-detector distance is known based on the beamline design. Beamline setup was confirmed using standards, including silver behenate. Each image was captured from 15 seconds of exposure. The patterns were collected on a DECTRIS EIGER X 4M detector. An angle of 0.1° was used in the experiments. We observed no beam damage caused by the X-ray beam by comparison of patterns at fresh locations in the film to patterns with multiple exposures.

GISAXS patterns were indexed with software[156, 159] courtesy of Detlef Smilgies and Ruipeng Li from the Cornell High Energy Synchrotron Source (CHESS) which allow for selection of lattice type, lattice parameters, and superlattice plane parallel to the substrate. The software overlays expected scattering peaks onto the patterns. The patterns were indexed manually by eye to ensure agreement between high intensity peaks at low scattering vectors as well as higher-order reflections.

3.10 Appendix A: Effect of QD shape on minimum center-to-edge distance.

The shape of PbS QDs varies with size, from octahedron to cuboctohedron to cube, and all the variants in between. This change in shape changes the possible minimum diameter of QD, which impacts the calculated edge-to-edge spacing from the center-to-center spacing measured using GISAXS and the QD diameter calculated from a QD sizing curve that assumed spherical QDs. Thus, here we aim to determine the minimum distance from the center to the surface of the QD as a function of QD shape, which we normalize by the radius of a sphere of equivalent volume.

The volume of a cube with side length D is given by $V_{cube} = D^3$, and the surfaces of the cube are (100) facets of the PbS lattice. If the corners are removed, revealing (111) facets, the shape becomes a truncated cube. If a triangular pyramid of length l along the edge of the cube is removed, the volume of each removed pyramid is given by $V_{tri.pyramid} = l^3/6$, and there are 8 corners, so the volume of truncated cube is given by

$$V_{trunc.cube} = D^3 - \frac{4}{3}l^3, 0 < l < \frac{D}{2} \tag{3.11}$$

In the limit that $l = D/2$, the shape becomes a cuboctahedron with volume $V_{cuboct.} = (5/6)D^3$.

Approaching from the other end of the spectrum of possible shapes, we consider an octahedron with (111) surface facets. The volume is given by $V_{oct.} = (\sqrt{2}/3)a^3 = D^3/6$, where $a = D/\sqrt{2}$ is the side length of the octahedron with height D. Removing the corners of an octahedron gives a truncated octahedron. If we remove a square pyramid of side length k, each with volume $V_{sq.pyramid} = k^3/3\sqrt{2}$, from each of the 6 corners, the volume is given by

$$V_{trunc.oct} = \frac{\sqrt{2}}{3}a^3 - \sqrt{2}k^3, 0 < k < \frac{a}{2} \tag{3.12}$$

When $k = a/2$, this also becomes a cuboctahedron. To ensure the truncated octahedron is a continuous shape transformation from the truncated cube, the height of the truncated octahedron, $\sqrt{2}(a - k)$, must equal D, so $a = D/\sqrt{2} + k$. Rescaling to let $k = \sqrt{2}(D - l)$,

$$V_{trunc.oct} = \frac{4}{3}\left(\frac{3D}{2} - l\right)^3 - 4(D - l)^3, \frac{D}{2} < l < D \tag{3.13}$$

gives a continuous shape transformation from cube to cuboctahedron to octahedron for $0 < l < D$ in equations (3.10) and (3.12). The radius of a sphere of equivalent volume is then calculated according to $r_{sphere} = (3V/4\pi)^{1/3}$.

Because of how the volume is defined, the distance from the center of the QD shape to the center of the (100) surfaces is always given by:

$$r_{100} = D/2. \tag{3.14}$$

The distance from the QD center to the center of the (111) surfaces of the truncated cube is along the diagonal of the cube and is given by:

$$r_{tc,111} = \frac{\sqrt{3}}{2}D - \frac{1}{\sqrt{3}}l, 0 < l < \frac{D}{2}. \tag{3.15}$$

The distance from the QD center to the center of the (111) surface in the truncated octahedron can be calculated as the height of a triangular pyramid with an equilateral triangle base with side length a and a volume one-eighth of the volume of the octahedron:

$$r_{to,111} = \frac{1}{\sqrt{6}}\left(\frac{D}{\sqrt{2}} + k\right) = \frac{1}{\sqrt{3}}\left(\frac{3D}{2} - l\right), \frac{D}{2} < l < D. \tag{3.16}$$

Normalizing equations ((3.13), (3.14), and (3.15) by the radius of a sphere with volume given by equations (3.10) and (3.12) gives the curves plotted in Figure 3.5.

3.11 Appendix B: Lattice Distortion from GISAXS

The initial superlattice for the 5.7 nm oleic acid QDs was indexed as an FCC lattice (Figure 3.7d) with $a = b = c = 13.2\ nm$. The nearest neighbor edge-to-edge spacing is $\frac{\sqrt{2}}{2}a - D = 3.63\ nm$. The final superlattice at 133 K was indexed as a BCT lattice (Figure 3.7e) with $a = b = 14.3\ nm$ and $c = 10.3\ nm$. The nearest neighbor edge-to-edge spacing is $\frac{\sqrt{a^2+c^2}}{2} - D = 3.11\ nm$. Overall, the nearest neighbor edge-to-edge spacing decreased by 14.3%. The edge-to-edge spacing in the [100] and [010] directions along the a and b axes starts as 7.5 nm and ends as 8.6 nm, amounting to an increase of 14.7%. This distortion is projected onto the 5.0 nm ethanethiol sample by indexing the initial pattern as an FCC lattice and applying similar percentage changes in the nearest neighbor edge-to-edge spacing and [100] or [010] directions. The lattice can be indexed as an FCC lattice with $a = b = c = 8.4\ nm$. The final superlattice would then be a BCT lattice with $a = b = 8.9\ nm$ and $c = 7.46\ nm$. The nearest neighbor edge-to-edge spacing decreased from 0.94 nm to 0.80 nm, a contraction of 1.4 Å. The indexed GISAXS images for the oleic acid sample can be found in Figure 3.7. The initial pattern for the ethanethiol sample and the projected BCT lattice are seen in Figure 3.8. This projection agrees well with the final GISAXS pattern despite the lack of higher order scattering peaks to confirm the structure.

Chapter 4 Origin of Trap States

The basis of this chapter is in preparation for submission as:
R. H. Gilmore, Y. Liu, N. S. Dahod, W. Wu, M. C. Weidman, H. Li, J. C. Grossman, W. A. Tisdale. "Origin of Trap States in Lead Sulfide Quantum Dot Solids."

4.1 Introduction

Mid-band gap trap states have garnered substantial attention because they reduce photovoltaic device efficiencies by reducing the open-circuit voltage[97] and acting as charge carrier recombination sites.[98] Trap states are involved in charge carrier transport, either directly through mid-gap transport,[96, 99] or through multiple trapping and release steps.[22, 87] The physical origin of these mid-gap trap states is usually thought to be a surface defect because their properties change with ligand treatments,[160] air exposure,[88] and other oxidation treatments.[94]

Here, we present spectroscopic observations of trap states in PbS QD solids, which suggest that they are QD dimers or aggregates. In QD solids with insulating oleic acid ligands, the trap states behave like isolated QDs. Upon excitation of the trap state in an ultrafast transient absorption experiment, charge carriers undergo Auger recombination, revealing a trap state degeneracy, bi-exciton decay time, and absorption cross section similar to the band edge state of a single QD. From temperature-dependent photoluminescence measurements, we find a trap state density of 1 in ~2500 QDs, which is consistent with literature reports for thiol-treated QD solids.[85-86, 88] The availability of states at the band edge energy is much higher than at the trap state energy, so upon populating only the trap state, we observe upconversion to the band edge state in coupled QD solids. De-trapping follows two mechanisms, a fluence-dependent, temperature-independent Auger-assisted electron transfer process that occurs on a timescale of ~35 ps, and a fluence-independent, temperature-dependent thermally-assisted hopping process that occurs on a time scale of ~500 ps.

The trap states clearly resemble large QDs, both in terms of their isolated optical properties and their transport properties in how they interact with surrounding band edge states. However, our QD ensembles are highly monodisperse with only 1-3% size dispersity, and the trap state would correspond to QDs five to ten standard deviations below the mean. We do not observe these large QDs in TEM images, but we do occasionally observe two attached QDs, which can produce the observed trap state optical properties. Strong electronic coupling between two fused QDs reduces the band gap of the dimer structure by ~100-200 meV relative to the single QD band gap (1.08 eV for 4.9 nm QDs and 1.3 eV for 4.2 nm QDs), creating this lower energy trap in the QD solid. Atomistic density functional theory calculations show that QD dimers attached on the (100) facet exhibit optical properties that are consistent with the measured properties of trap state dimers in QD solids.

4.2 Photoluminescence from Band Edge and Trap States

PbS QDs were synthesized according to previously published procedures,[27, 37] dispersed in toluene, and spin coated onto glass substrates for TA measurements and single crystal quartz substrates for low temperature PL measurements. To make electronically coupled solids, QD solids were ligand exchanged with ethanethiol in a nitrogen glovebox (see Section 4.9).[50] In Figure 4.1a, we present photoluminescence spectra for 4.9 nm (1.08 eV first absorption peak) QDs. At room temperature, we observe emission from the band edge state, but as the temperature decreases, emission from a mid-band gap state grows in. Chuang *et al.*[97] observed a similar state, which they identified as the likely origin of the large open-circuit voltage deficit in PbS QD photovoltaics. Despite the presence of the lower energy state, which is expected to act as a trap state, there are many more available states at the band edge, and at room temperature there is sufficient thermal energy for charge carriers to escape the trap, as shown in the schematic in Figure 4.1b. The occupations, *n*, of the two states follow a Boltzmann distribution that accounts for the degeneracies, *g*, of the band edge and trap states:

$$\frac{PL_{BE}}{PL_{trap}} \propto \frac{n_{BE}}{n_{trap}} = \frac{g_{BE}}{g_{trap}} \exp\left(\frac{-\Delta E}{k_{\mathrm{B}}T}\right). \tag{4.1}$$

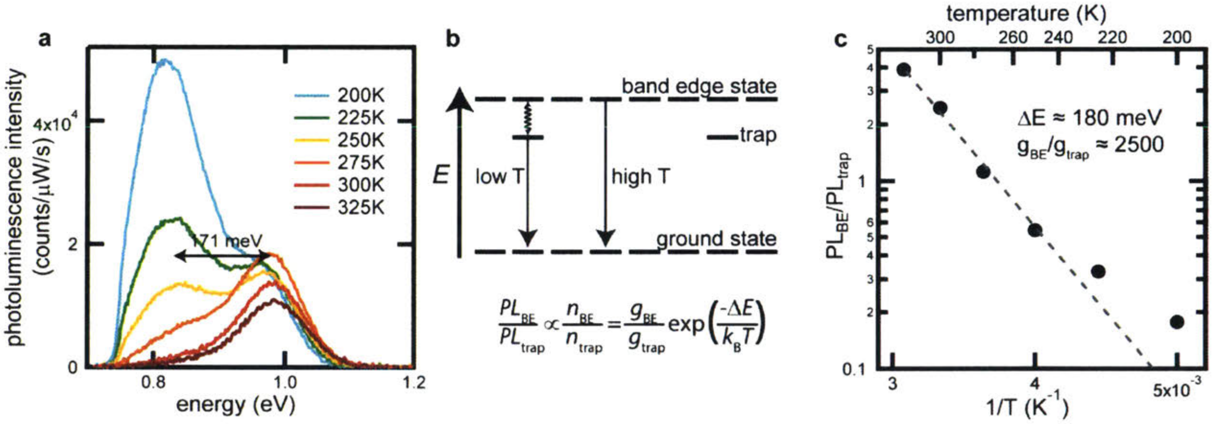

Figure 4.1. Emission from band edge and trap states in ethanethiol-treated PbS QD solids. (a) Photoluminescence spectra as a function of temperature showing PL from the band edge state at room temperature and from the trap state at lower temperatures. (b) Schematic showing much higher density of states at the band edge than at the trap state energy, so that at room temperature, charge carriers are thermalized into the band edge states. (c) Ratio of band edge to trap state PL as a function of temperature (filled circles). A fit (dashed line) gives the energetic barrier between QDs and the density of trap states.

If we assume similar radiative rates for the band edge and mid-gap trap state, the ratio of occupations is equal to the ratio of PL emission from the two states, and we can fit the degeneracy and activation energy, as is shown in Figure 4.1c. Note that we fit the emission only at high temperatures when excitons readily dissociate to free carriers (see Figure 1.4).[55-56] We find a trap state degeneracy of 1 in ~2500 QDs, which is consistent with other published trap state degeneracies in thiol-treated films measured using a variety of techniques.[85-86, 88, 93, 98] We find an activation energy of ~180 meV, which is approximately equal to the energy difference between the band gap and trap states, suggesting that either the conduction band or the valance band, but not both, shifts appreciably in energy.

4.3 Transient Absorption Directly Excites Trap States and Monitors De-trapping

Given equilibrium between band edge and trap states in coupled QD solids, if only the trap state is populated, upconversion to the band edge state is expected, as shown in the schematic in Figure 4.2a. We observe the dynamics of this de-trapping process using ultrafast transient absorption spectroscopy (see Section 4.9). In Figure 4.2b, the trap state at 1.06 eV of 4.2 nm (1.3 eV) QDs is excited with a 0.99 eV pump laser pulse, and de-trapping to the band edge state is observed. The energy of the band edge bleach signal at 1.24 eV is the thermalized energy of the band edge signal when excited well above the band gap.[151] Spectral slices (Figure 4.2g) clearly show only the trap state bleach at early times, and the population of both states at later times. The intensities of the band edge and trap state bleach signals as a function of time are presented in Figure 4.2g. If we assume that the decrease in bleach intensity of the trap state is entirely due to carriers de-trapping to the band edge state, we estimate that the trap state absorption cross section is approximately two to three times the band edge absorption cross section.

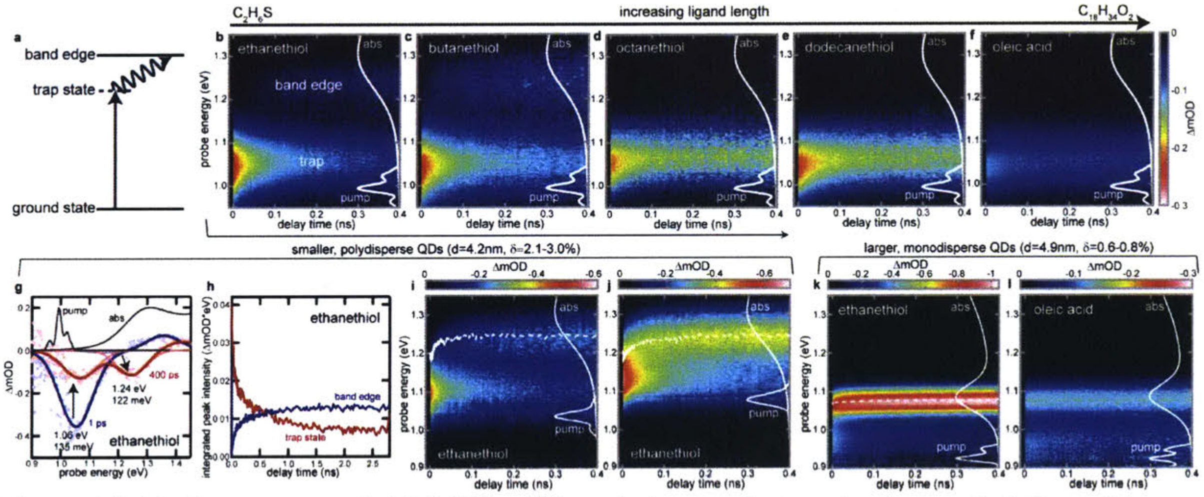

Figure 4.2. Excite trap states in PbS QD solids and observe de-trapping in coupled films. (a) Schematic showing population of the trap state followed by upconversion to the band edge state. (b-f) Color plots showing excitation of the mid-gap trap state QD solids ($d = 4.2$ nm, $\delta = 2.1$-3.0%) with varying ligand lengths. The pump spectra and QD solution absorption spectra are shown overlaid for reference. (g) Spectra at early and late times for the ethanethiol treated solid (b), with peak position and fwhm for the trap state and band edge peaks. (h) Integrated peak intensities as a function of delay time for the ethanethiol treated solid (b). (i-j) Color plots showing dynamics following mixed excitation of the trap and band edge state. (k-l) Excitation of the mid-gap state and band edge state in larger, monodisperse QD solids ($d = 4.9$ nm, $\delta = 0.6$-0.8%).

The mid-gap trap states are also present in QD solids with oleic acid ligands, but de-trapping to the band edge does not occur (Figure 4.2f). Exciting the trap state in QD solids with varying length thiol ligands (Figure 4.2b-e), we see that de-trapping occurs only for the shortest two ligands, ethanethiol and butanethiol, but not for the longer octanethiol or dodecanethiol ligands. From these results, we conclude that electronic coupling and fast diffusion away from the trap site is needed to depopulate the mid-gap trap state (see also Figure 4.3). Additionally, the trap state bleach intensity in the thiol-treated samples is consistently approximately three times greater than that in the oleic acid sample, indicating an increase in the trap state density with ligand exchange.

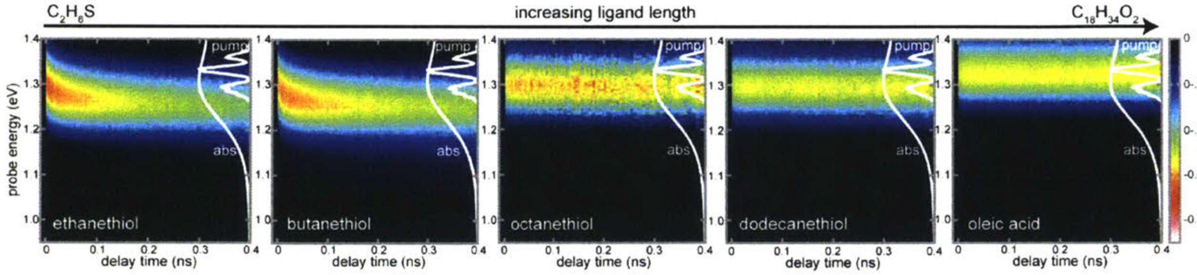

Figure 4.3. Transient absorption exciting at the band edge peak for QD solids with thiol ligands of varying lengths. A transient redshift indicating charge transport in the observed time window is present for ethanethiol and butanethiol QD solids, but not for octanethiol, dodecanethiol, or oleic acid.

To gain a better understanding of the energy distribution of the trap state as compared to the band edge state, we vary the excitation energy in the ethanethiol QD solid. As the excitation energy is increased to 1.03 eV and 1.08 eV (Figure 4.2h,i), the low energy tail of the band edge state is increasingly initially populated. The expected blue-shift to the thermalized equilibrium average energy (white dashed line) is then observed in addition to de-trapping. The mid-gap trap state and de-trapping in coupled solids is also observed in larger, monodisperse QDs (4.9 nm, 1.08 eV), but the trap state and band edge state are too close in energy to be able to excite only the trap state with our laser excitation pulse, so the band edge and trap states are excited simultaneously (Figure 4.2k,l). The monodisperse QDs and the excitation energy dependence clearly show that the mid-gap state is a distinct state and not simply an exponential tail of the size distribution, as has been suggested previously.[84, 100] Furthermore, the trap state absorption bleach at 0.97 eV in these larger QDs is lower in energy than in the smaller QDs, and closer in energy to the band edge peak, indicating a size-dependence of the mid-gap trap state energy. Spectral slices and peak intensity as a function of time are given in Figure 4.4. Excitation of trap states followed by de-trapping to the band edge is also observed for ligand exchange with 3-mercaptopropionic acid or tetrabutylammonium iodide (Figure 4.7).

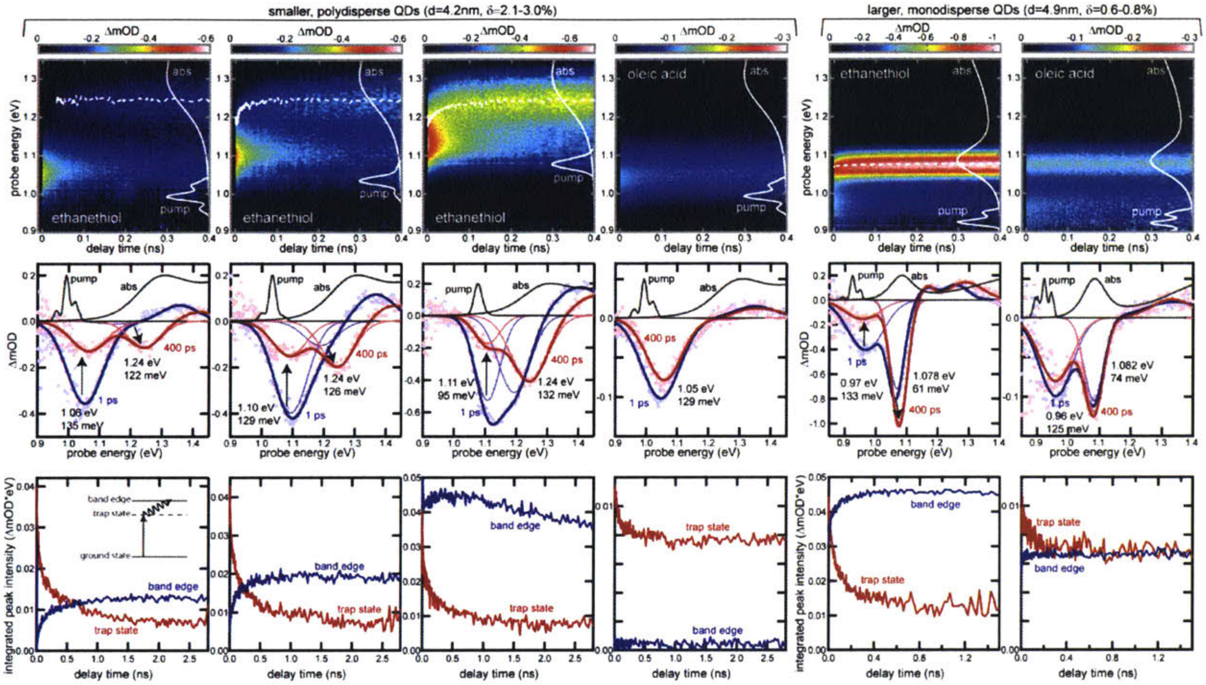

Figure 4.4. Transient absorption spectroscopy showing excitation of the trap state and upconversion to the band edge state in QD solids with ethanethiol ligands. (top row) Color plots repeated from Figure 4.2. (middle row) Spectra at 1 ps and 400 ps for the QD solids in the row above. (bottom row) Population dynamics of the band edge and trap states for the QD solids shown in the top row.

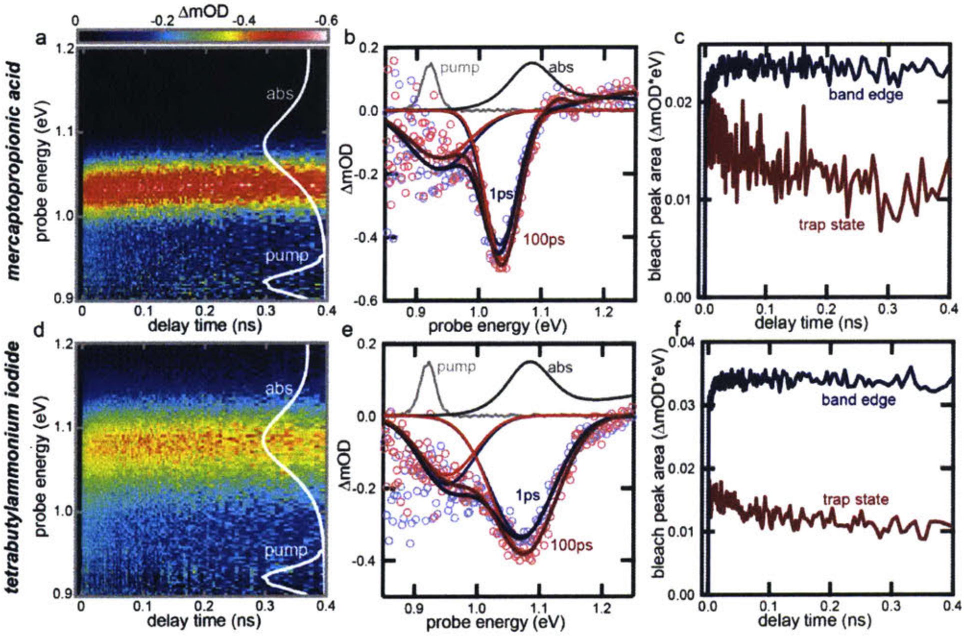

Figure 4.5. PbS QDs with mercaptopropionic acid (top row) and tetrabutylamonium iodide (bottom row) ligands also show trap state excitation and upconversion to the band edge state.

4.4 Trap State Dynamics are Similar to that of Large QDs

To learn more about the nature of the trap state and the de-trapping process, we turn to fluence-dependent measurements. Figure 4.5a presents the integrated trap state bleach intensity in an oleic acid QD solid as a function of delay time following trap state excitation for several excitation fluences. The initial bleach intensity increases with fluence, as does the fraction of the intensity that decays within the first ~100 ps. These dynamics are reminiscent of Auger recombination dynamics in isolated QDs in solution. Indeed, the time constants of the multi-exciton decay are in line with the band edge multi-exciton decay in PbS QDs (Figure 4.5b), which becomes faster for smaller QDs.[110] The absorption cross section of the trap state can also be estimated from the intensity-dependent measurements, and yields a value of 8×10^{-16} cm^2 (Figure 4.5c), which is the same order of magnitude as the band edge state (see Figure 1.9b,c).[102, 161] Thus, based on their optical absorption properties, the trap states appear to be large QDs isolated within a matrix of smaller QDs.

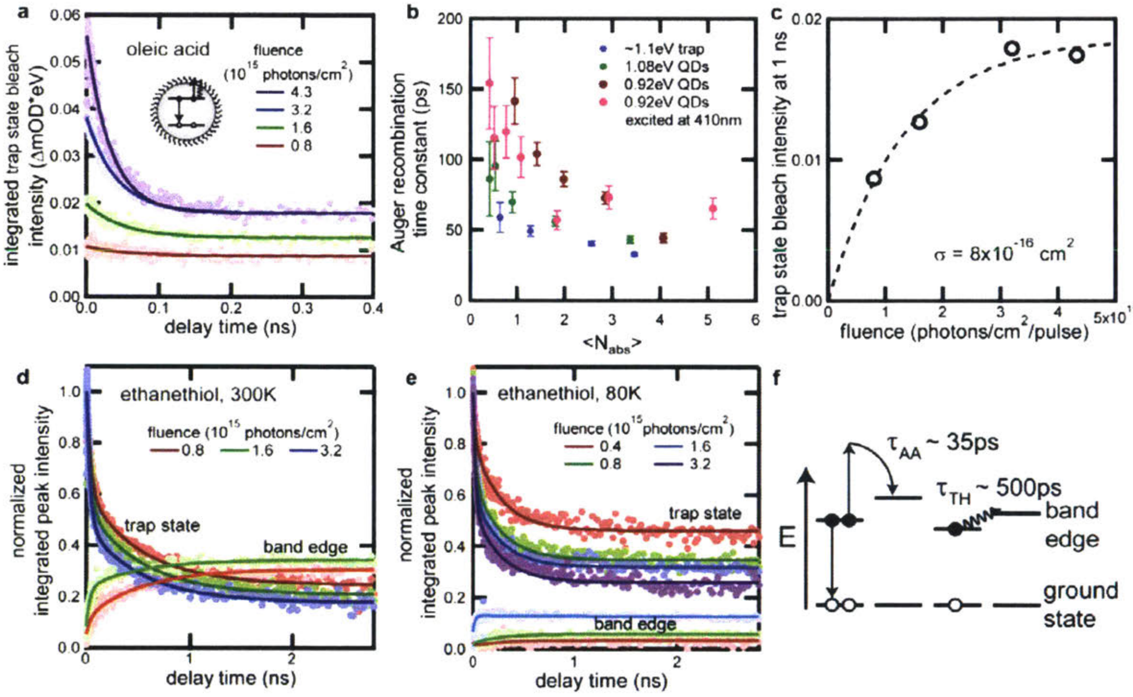

Figure 4.6. Trap state bleach dynamics. (a) Trap state bleach intensity in QD solid with oleic acid ligands as a function of delay time and excitation power showing dynamics characteristic of Auger recombination. (b) Decay time constant as a function of number of excitons absorbed per QD for the trap state and various sizes of QD band edge states. (c) Bleach intensity at 1ns as a function of excitation fluence with experimental data shown with open circles and a fit to the data to determine the absorption cross section shown with a dashed line. (d) Trap state and band edge bleach dynamics in ethanethiol-treated QD solid excited at the trap state energy with varying excitation powers at 300 K. Fitted time constants are 39 ± 5 ps (0.8×10^{15} photons/cm^2), 35 ± 3 ps (1.6×10^{15} photons/cm^2), 34 ± 2 ps (3.6×10^{15} photons/cm^2), and 520 ± 40 ps (all). The contribution from the fast component increases with increasing fluence. (e) Dynamics at 80 K. (f) Schematic showing proposed de-trapping mechanism.

Fluence dependent measurements on coupled QD solids with ethanethiol ligands reveal transport dynamics that are consistent with the trap state being large QDs in the ensemble. Figure 4.5d presents the normalized integrated trap and band edge state bleach intensities as a function of delay time following trap state excitation for multiple excitation fluences at 300 K. As the excitation fluence increases, the magnitude of population transfer from the trap to the band edge state increases. The de-trapping process follows two timescales, a fast component that increases in magnitude with increasing fluence, and a slow component that does not depend on fluence. Fluence-dependent measurements at 80 K (Figure 4.5e) freeze out the slow de-trapping mechanism, but reveal that the fast de-trapping mechanism is temperature-independent. The fast, ~35 ps, de-trapping process occurs on similar time scales as the Auger recombination process observed in oleic acid QD solids, so we conclude that the temperature-independent, fluence-dependent fast de-trapping process is an Auger-assisted process in which Auger recombination creates a hot charge carrier which then rapidly transfers to a neighboring QD before cooling back to the band edge. We assign the slow, ~500 ps, de-trapping mechanism to thermally-activated charge carrier hopping.[151] A summary of these two de-trapping mechanisms is presented in Figure 4.5f.

4.5 Trap States are QD Dimers

The presence of very large QDs that act as trap sites in the QD solid is surprising based on our materials characterization. These QDs are highly monodisperse, with the standard deviation of the size dispersion only 3.0% for the 4.2 nm QDs and 1.0% for the 4.9 nm QDs.[151] In contrast, the trap state energies would correspond to QDs with diameters of 4.7 nm and 5.4 nm for the 4.2 nm and 4.9 nm QDs respectively, 5-10 standard deviations larger than the mean diameter. We do not see evidence for these large QDs in our TEM images (Figure 4.6a).[27, 50] However, we do occasionally see two QDs that appear to be touching each other. High-resolution TEM (HR-TEM) reveals that the QDs are actually fused into a dimer QD (Figure 4.7b,c), which is expected to have a lower energy than a single QD.[79, 162]

To confirm the presence of PbS quantum dot dimers, HR-TEM images of PbS quantum dot monolayers were collected and analyzed (Figure 4.7). For this analysis, a dimer is defined as two PbS quantum dots fused together such that they support a single continuous crystal structure throughout both substructures. This is observed *via* clear lattice planes that span the entire dimer with no change in orientation (Figure 4.7b). In contrast, unattached quantum dots that are simply in close proximity to one another would not display any alignment between their two lattices (Figure 4.8a). Thus, in order to confirm attachment between two quantum dots that appear to be in contact, analysis of the HR-TEM images must reveal that the constituent nanocrystals are in fact aligned on one of their faces.

This analysis is implemented through inspection of the fast Fourier transform (FFT) of the candidate dimer image. The FFT reveals the orientation and spacing of the lattice planes visualized in HR-TEM. For instance, FFT analysis of a HR-TEM image of a quantum dot with its (200) plane parallel to the beam would reveal a peak at a 0.31 nm/cycle radial position with respect to the center spot of the FFT. This spacing is confirmed by inspecting the (200) peak in the XRD pattern for PbS. Additionally, the azimuthal position of the spot corresponding to these lattice planes is determined by the angle of the planes with respect to the image. For instance, two QDs in the same image with (200) planes oriented perpendicular to one another would show a difference in azimuthal position of 90 degrees with respect to the corresponding FFT spots. Several QDs in an image oriented randomly will show FFT spots at many azimuthal positions and radial distances (Figure 4.8a).

In analyzing potential dimers, FFTs of both constituents and the entire dimer were used to determine if all showed lattice planes that were aligned with respect to one another. Through this method, we observed PbS quantum dot dimers that were attached across their respective (100) faces (Figure 4.7b). We also observed one case in which two dots likely slightly eschew from this attachment and dimerize with a twinning boundary between the constituents (Figure 4.7c and Figure 4.8b). In this case, while the lattices were aligned as expected, the actual planes in alignment were different.

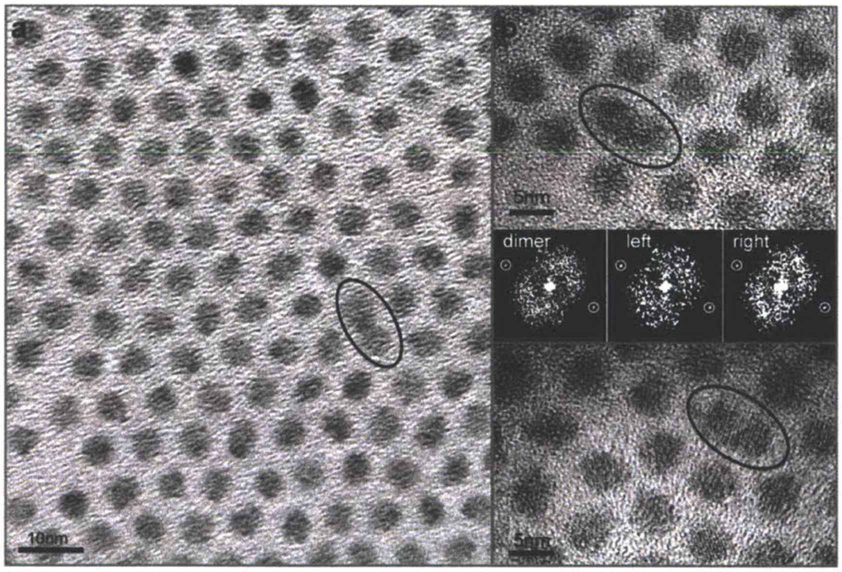

Figure 4.7. (a) TEM micrograph of monodisperse 4.9 nm QDs with oleic acid ligands showing an absence of large QDs, but the presence of a QD dimer. (b) HR-TEM micrograph of a dimer with FFT of the entire dimer and the left and right QD within the dimer, all identical and showing (100) planes oriented to the surface, indicating attachment on the (100) facet. (c) HR-TEM micrograph of a dimer with a twinning boundary at the attachment interface. FFT shows the left side of the dimer has (100) planes oriented to the surface while the right side has (111) planes, but the radially aligned peaks indicate aligned lattice planes across the dimer confirming fused attachment.

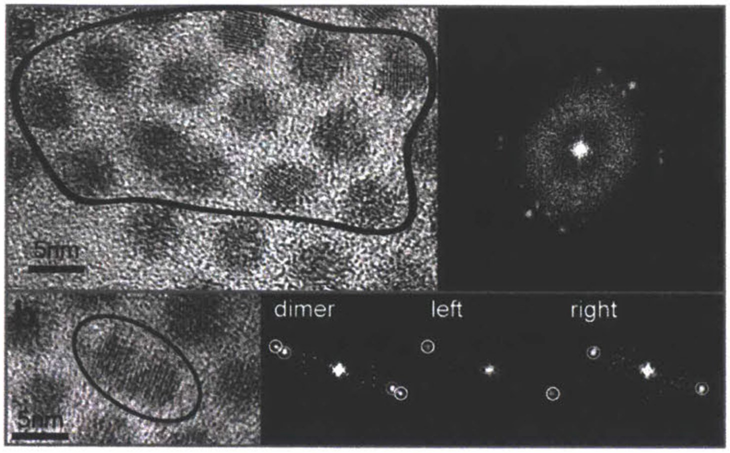

Figure 4.8. FFT analysis of HR-TEM images. (a) FFT analysis of a monolayer of unattached, randomly oriented QDs shows many FFT spots at different azimuthal positions. (b) FFT analysis for the dimer shown in Figure 4.7 shows two different lattice planes aligned and epitaxially attached.

Intentional formation of PbSe QD dimers by controlling the synthetic conditions has been demonstrated,[162] as has oriented attachment of PbSe QDs to form extended superlattices.[83, 163] Removal of surface ligands using $(NH_4)_2S$ results in connected QD assemblies for PbS, PbSe, CdSe, and CdS QDs, indicating that bare QD surfaces are likely attach across a range of materials.[164] It is therefore unsurprising that a few dimers could form unintentionally during standard synthesis and ligand exchange procedures. Oriented attachment of PbSe QDs proceeds along the (100) facets,[83, 163] and we also find fusing predominantly on the (100) facets in our QD dimers. Increased likelihood of fusing on the (100) facet may be a result of more weakly bound ligands and a greater chance of a bare surface on this facet as compared to the (111) facet.[165] Some dimers are formed during initial synthesis and solution processing and are present in solution and oleic acid samples (Figure 4.9). These dimers are not separated from single QDs by size-selective precipitation using common solvent/non-solvent pairs,[162] and so are not removed during purification steps. Additional dimers are formed during the solid-state ligand exchange step, increasing the trap state density by 50% to 100% following ligand exchange.

QDs made using lead oleate or lead acetate precursors, rather than lead chloride, show no measureable dimer trap state absorption with native oleate ligands, but do show trap state absorption after ethanethiol ligand exchange (Figure 4.10). There are several possible reasons why the lead chloride and oleylamine synthesis method might result in measurable dimer states, whereas the lead oleate or lead acetate synthesis methods do not. Oleylamine binds weakly to the QD surface and is in rapid equilibrium,[36] so it may be easier for ligands to detach and create bare surfaces that may fuse. The dimers might also form during the oleylamine to oleic acid solution ligand exchange step. The lead chloride and oleylamine synthesis is capable of producing nearly monodisperse QDs, and more monodisperse QDs may orient and fuse more readily.[79]

Additionally, different purification and processing steps might result in different ligand coverage,[165] which could also impact the likelihood of dimer formation. Alternatively, traps may be present at similar rates, but are harder to resolve because of greater inhomogeneous broadening. More work is needed to further understand the role of the synthetic method in dimer formation in order to make monodisperse, homogeneously-broadened, trap-free PbS QD solids.

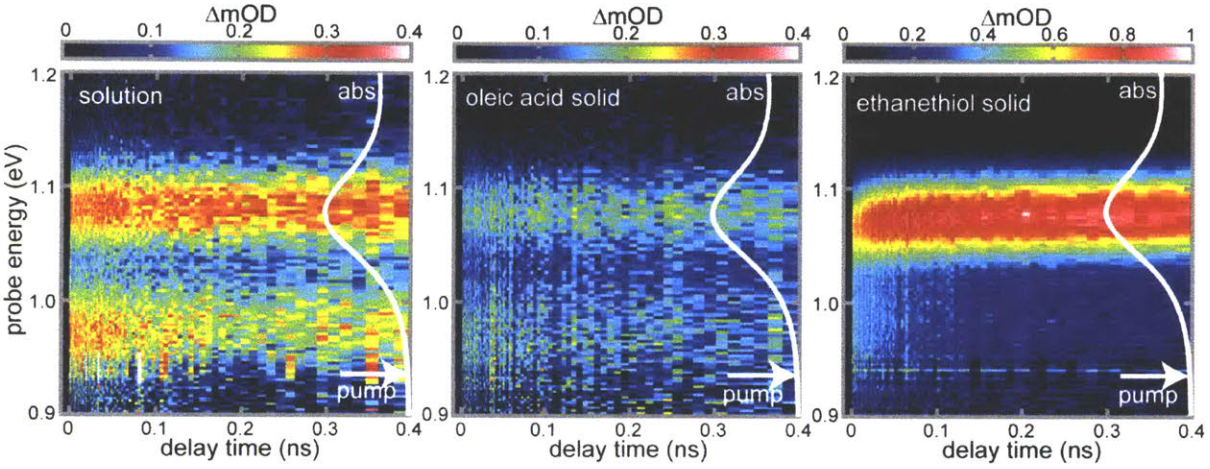

Figure 4.9. Trap state excitation of oleic acid-capped QDs in solution, oleic acid-capped QD solids, and following ligand exchange for ethanethiol. The optical density at the band edge peak absorption was 0.2 for the solution sample, 0.1 for the oleic acid sample, and 0.08 for the EMT sample. Thus, the concentration of trap states seems to be the same in solution and in a QD solid with oleic acid ligands, but is higher for ethanethiol-treated solids, even after accounting for an increase in absorption cross section for the shorter ligands.[47]

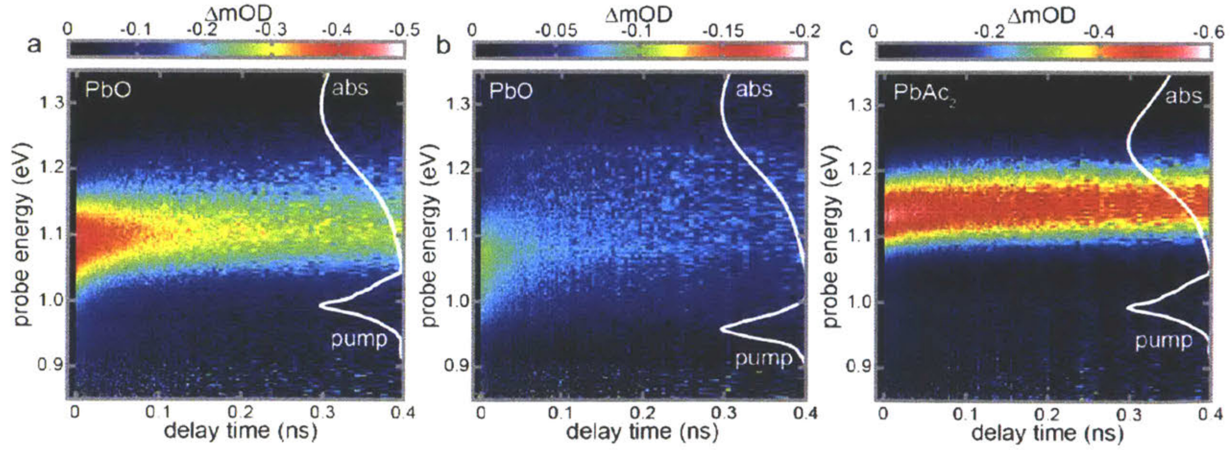

Figure 4.10. Trap state excitation in QDs synthesized with PbO (a-b) or PbAc$_2$ (c). (b) has a longer wavelength pump pulse than (a)

4.6 Expected Electronic Structure of a QD Dimer

We turn to theoretical models to verify that the lowest energy transition of the QD dimer is consistent with the observed trap state energy. Hughes *et al.*[162] previously reported the intentional synthesis of PbSe QD dimers in solution. They observed energetic splitting between the single QD and QD dimer levels, which decreased with increasing QD size from ~150 meV for 3 nm QDs to ~50 meV for 7 nm QDs.[162] This size-dependent trend in the energy splitting was explained using a tight binding model based on the effective mass approximation and spherical wave functions, with faceted QDs represented by spherical QDs of equivalent volume.[120, 162] The energy splitting was then calculated for fused QD dimers for which the equivalent spherical QDs are overlapped, so the center-to-center distance is less than the equivalent spherical QD diameter. We adapted this model for faceted PbS QDs as shown in Figure 4.9. This model predicts slightly shallower trap state depth than the ~100-200 meV we observe in our 4 to 5 nm faceted PbS QDs, but the size-dependent trend is consistent. However, this model makes many simplifying assumptions and does not account for attached facet, the size of the fused area, or any atomic rearrangement that may occur between fused QDs, which should impact coupling.[136, 166-167]

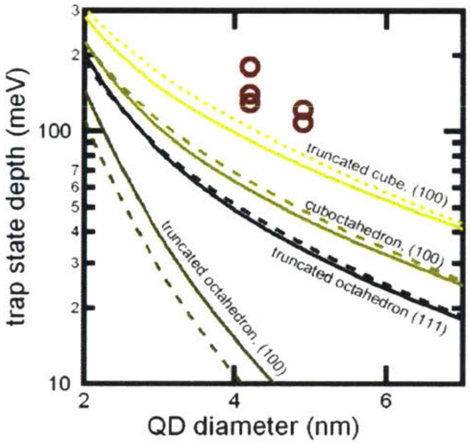

Figure 4.11. Calculated trap state depth for different QD shapes (truncated octahedron, cuboctahedron, truncated cube) and attached facets ((100), (111)) based on effective mass and tight binding approximations.[120, 162] Calculations with a confining potential barrier of 1.0 eV[162] are shown with solid lines and of 1.6 eV[93] with dashed lines. Trap state depth extracted from transient absorption measurements are shown in red circles.

To gain additional insight into how the dimer structure, in particular the crystalline facet and size of the fused region, relates to the band gap, we performed density functional theory calculations. Isolated QDs with diameters around 2 nm and 2.5 nm were constructed and directly fused along the (100) facet, similar to our previous work.[168] The bandgaps of the simulated 2 nm and 2.5 nm QDs agree with the experimental bandgaps of around 1.3 and 1.1 eV for 4.2 nm and 4.9 nm QDs respectively, due to the well-known DFT underestimation of semiconductor bandgaps. When only 4 atoms are fused, the band edge states and first exciton peaks of the fused dimer is similar to that of single isolated QD (Figure 4.10c). As the size of the fused region connecting QDs is increased (Figure 4.10a), additional absorption peaks with comparable degeneracies and absorption coefficients appear at lower energies than the first absorption peak of the single isolated dot (Figure 4.10b,c). The redshifts of the dimer peaks relative to the single QD of 80 – 210 meV are not directly proportional to the degree of fusing; rather they depend on the exact geometric configuration of the fused region. In particular, when there are 12 atoms in the fused plane, there is significant localization of the wavefunction around the fused region of the dimer (Figure 4.10d), representing a substantial change to the electronic structures. Similar results were obtained for the 2.5 nm simulated dot, for which dimers showed a redshift of the first exciton peak by ~30 – 70 meV and slightly higher absorption coefficients than the single QD (Figure 4.11).

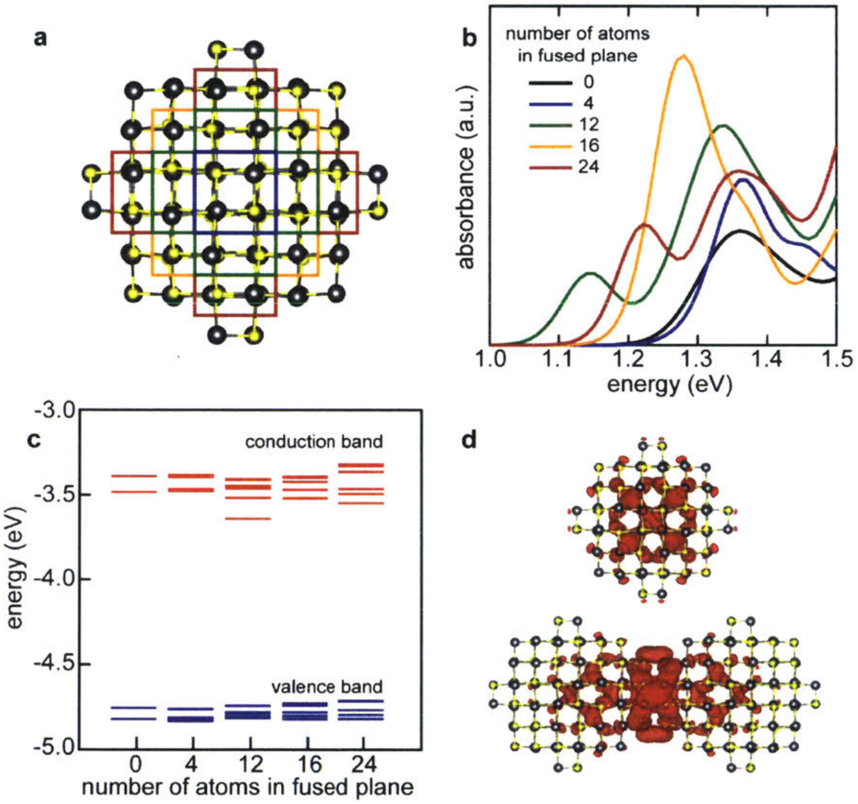

Figure 4.12. Sideview of the 2 nm diameter PbS QD. The black and yellow atoms represent Pb and S respectively. The colored boxes represent increasing degree of fusing in the QD dimers, from 4 to 12, 16, and 24 atoms. The fusing occurs along the (100) facet. The absorption spectra and (c) band edge states of fused dimers, compared with single isolated QD. (d) The wavefunction of the conduction band minimum of a single dot, and that of the fused dimer with 12 atoms in the fused plane. Significant localization of the states along the fused region compared to the delocalized states in the QD core for the single dot.

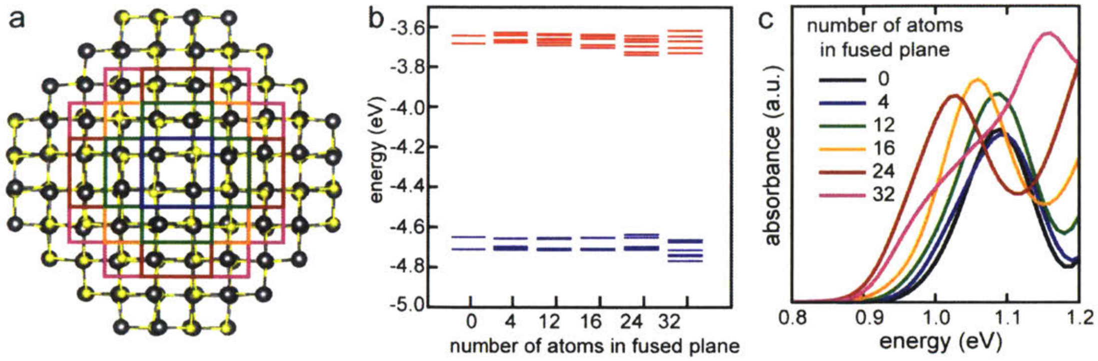

Figure 4.13. Sideview of the 2.5 nm diameter PbS QD. The black and yellow atoms represent Pb and S respectively. The colored boxes represent increasing degree of fusing in the QD dimers, from 4 to 12, 16, 24, and 32 atoms. The fusing occurs along the (100) facet. The absorption spectra and (c) band edge states of fused dimers, compared with single isolated QD.

The energetic shifts calculated in these atomistic calculations are consistent with the experimentally measured trap state energies and with the expected size-dependent trend. The number of atoms in the attached facet adds another variable in addition to size dispersity that increases the energetic disorder of QD dimers as compared to single QDs. Thus, we expect a greater linewidth for the ensemble QD dimer absorption as compared to the single QD absorption, which is observed experimentally for the highly monodisperse QDs. In contrast to the (100) fused QDs, QDs fused on the (111) facet showed very large reductions in the band gap energy by as much as 1 eV, and absorption spectra that do not resemble single QD absorption spectra in shape. Thus, the lowest energy transitions of QD dimers and absorption cross sections of these transitions are consistent with the assignment of trap states in QD solids to QD dimers fused on (100) facets.

4.7 Comparison to Trap State Literature

In light of the assignment of traps in PbS QD solids to QD dimers, we re-examine the literature, which generally assumes that traps are a surface defect state to see if it is consistent with QD dimer traps. Speirs *et al.*[95] observed a reduced trap state density and 147 meV increase in the open-circuit voltage in PbS/CdS core/shell QD solar cells as compared to core-only solar cells. We propose that the CdS shell prevents dimer formation, rather than passivates surface defect trap states as the authors suggest. Bozyigit *et al.*[34] used thermal admittance spectroscopy to measure the spectra of electronic trap states in PbS QD solids, and found a trap state spectrum that looks similar to a QD absorption spectrum, consistent with our findings from atomistic simulations of QD dimers. In light of the de-trapping mechanisms we have observed (Figure 4.6f), the observation of electrical current in response to optical excitation below the band edge may be a result of charge carrier de-trapping and transport through band edge states, rather than transport through trap states.[96]

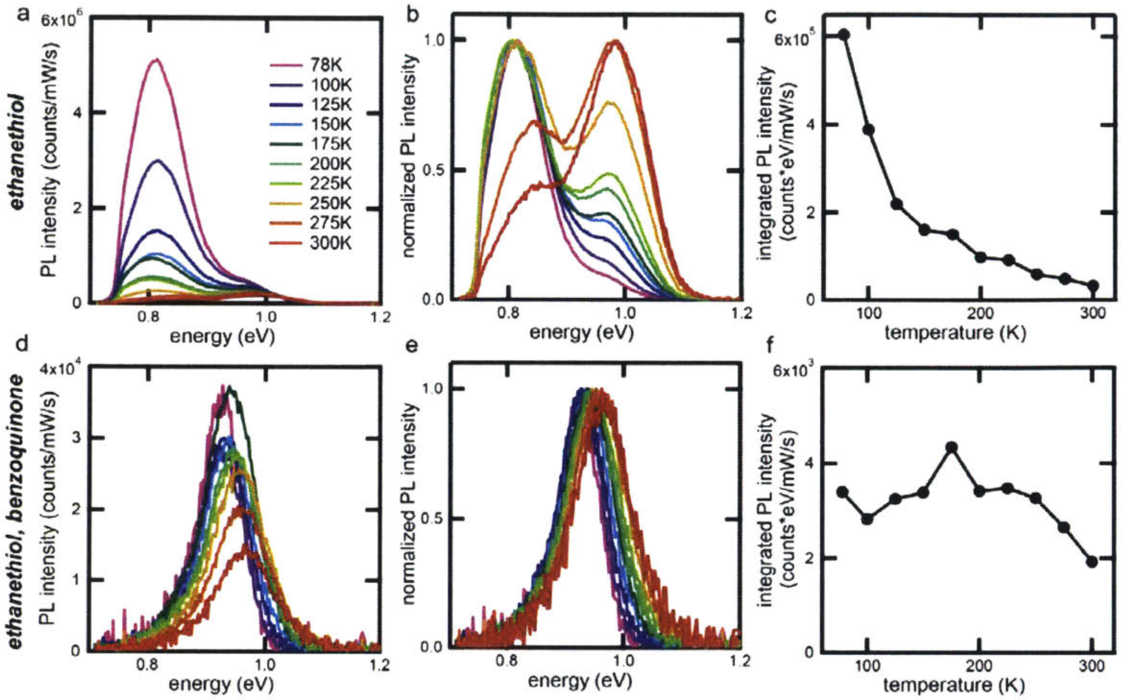

Figure 4.14. Temperature-dependent photoluminescence spectra for (a) ethanethiol-treated and (b) benzoquinone and ethanethiol-treated PbS QD solids. Normalized spectra are shown in (b) and (e) respectively. Integrated PL intensity as a function of temperature are shown in (c) and (f).

It has been proposed that undercharged Pb atoms create emissive surface trap states, which can be removed by oxidation treatments such as benzoquinone (BQ) to restore only band-edge PL in ligand exchanged QD solids.[94] We treated our PbS QD solids with BQ to see whether oxidation can remove the optically active dimer trap states in our QD solids. We found that the BQ treatment did remove the trap state PL from the ethanethiol-treated QD solids, restoring band edge PL at all temperatures (Figure 4.12). However, it also decreased the quantum yield by an order of magnitude, and the PL intensity remains low as the temperature decreases (Figure 4.12f). While there is no evidence of trap states in the PL measurements, in TA measurements (Figure 4.13) we are still able to directly excite the trap states in BQ-treated QD solids with either oleic acid or ethanethiol ligands. Based on the TA bleach intensity, the density of trap states may have decreased by up to ~10%, but increased scattered light might also account for this difference. The oleic acid samples have TA bleach dynamics that are very similar to non-BQ treated samples, but the ethanethiol samples show little-to-no upconversion to the band edge state. When we excite at the band edge state (Figure 4.14), BQ treated samples with either oleic acid or ethanethiol ligands show much faster charge carrier lifetimes than their non-BQ treated counterparts. Based on the low QY in BQ-treated solids, we conclude that BQ treatment introduces additional non-radiative recombination pathways in the QD solid. Because charge carriers recombine more quickly, a measureable population at the band edge never builds up in a TA experiment exciting the trap state. Additionally, when charge carriers are excited at the band edge, they are likely to recombine before reaching a trap state, so PL is observed only at the band edge energy. Thus, our experiments suggest that oxidation treatments do not remove dimer trap states, but instead inhibit charge transport and reduce charge carrier lifetimes in QD solids.

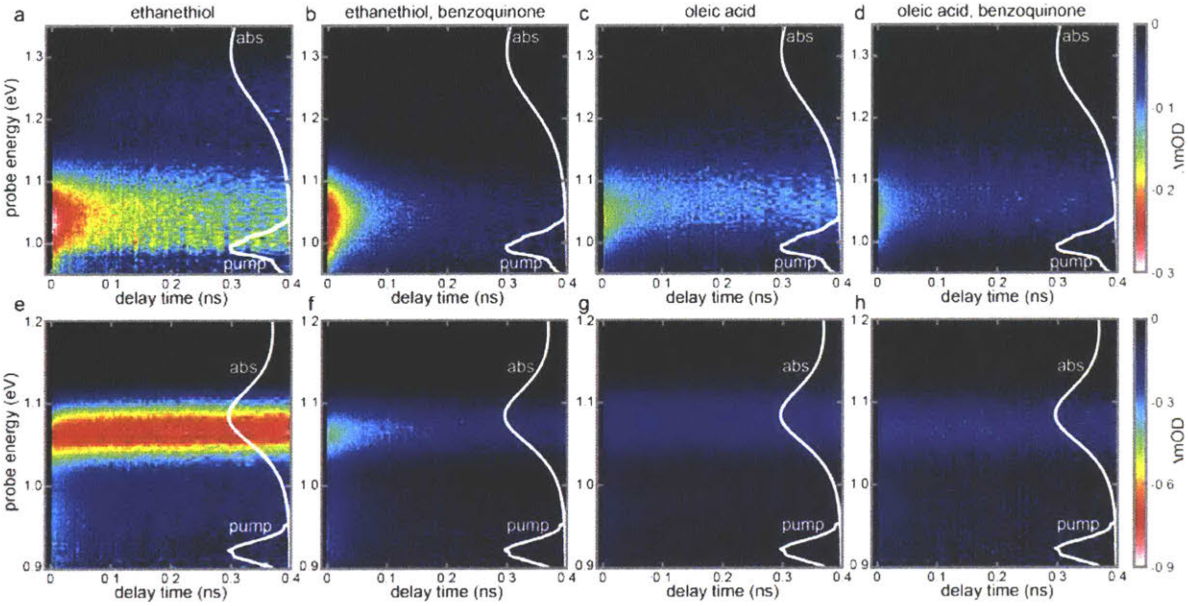

Figure 4.15. Optically exciting the trap states in QD solids with and without benzoquinone treatment.

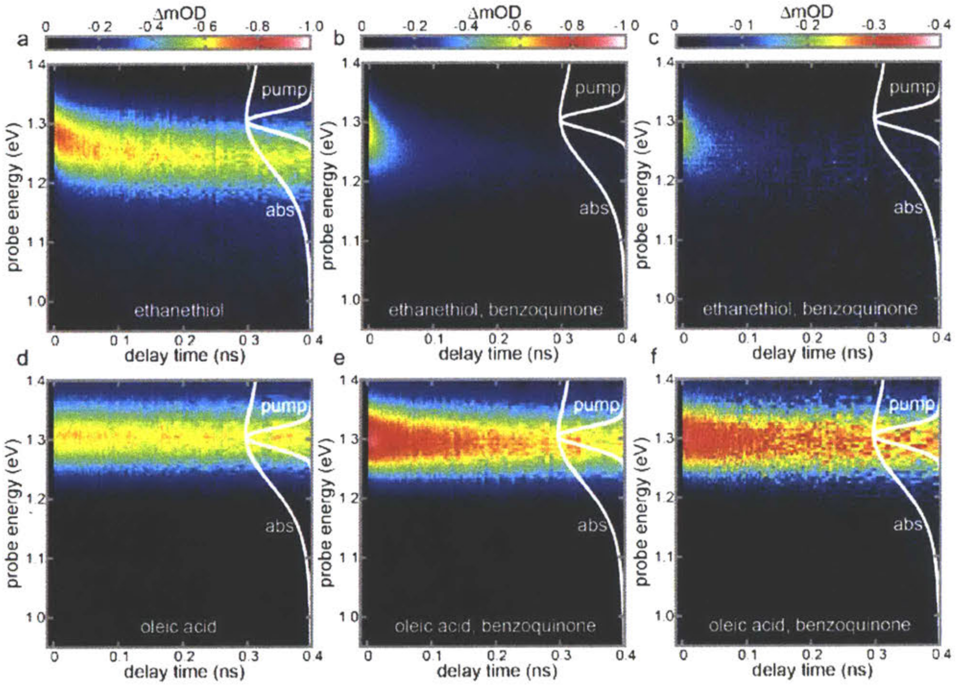

Figure 4.16. Exciting QD solids with and without benzoquinone treatment at the band edge state.

4.8 Conclusions

Future efforts must carefully optimize QD synthesis and device fabrication procedures to avoid the accidental formation of dimers, as they can significantly inhibit QD device performance even at very low concentrations of 1 in ~1000 QDs. Improved separation techniques beyond size-selective precipitations are needed to remove dimers that form during synthesis. Since additional dimers also readily form during solid state ligand exchange, solution-phase ligand exchanges,[21, 169] followed by purification to remove any dimers, may be required to form strongly coupled QD solids free of dimer trap states that can ultimately boost QD device efficiency.

4.9 Experimental Methods

PbS QD synthesis and QD solids preparation: The 4.2 nm QDs were synthesized according to Zhang *et al.*[37] and the 4.9 nm QDs were synthesized according to Weidman *et al.*[27] Both syntheses use $PbCl_2$ in oleylamine, but the Zhang synthesis uses bis(trimethylsilyl)sulfide ($(TMS)_2S$), while the Weidman synthesis uses elemental sulfur. The oleylamine ligands from synthesis were replaced with oleic acid ligands during purification steps following synthesis. Purified QDs were re-dispersed in toluene at a concentration of 100 mg/mL in a nitrogen glovebox. 40μL of this solution was spin cast at 1500 rpm for 30 s onto a 0.5 in square borosilicate glass slide (Schott D-263 from Thermo Fisher) for TA measurements or a 1 cm single crystal quartz substrate for PL measurements that had been cleaned and treated overnight with 0.02M (3-mercaptopropyl)trimthoxysilane (Sigma-Aldrich, 95%) solution in toluene to improve QD adhesion. Some samples were then placed in a 0.1M solution of the desired ligand (1-ethanethiol (Sigma Aldrich, 97%), 1-butanethiol (Sigma Aldrich, 99%), 1-octanethiol (Sigma Aldrich, 98.5%), 1-dodecanethiol (Sigma Aldrich, ≥98%), or 3-mercaptopropionic acid (Sigma Aldrich, ≥99%) in acetonitrile for 24 hours for ligand exchange. The ligand exchange for tetrabutylammonium iodide (Sigma Aldrich, ≥99%) was done at a concentration of 10 mg/mL in methanol, and allowed to sit on the sample for 30 s before spinning to remove and then washing with pure methanol. This created films that were ~100-200 nm thick and have an optical density of ~0.1 at the first absorption peak. Prior to ligand exchange, these QDs are air stable, and following ligand exchange, the samples were kept in an inert environment at all times, including during TA and PL measurements.

Photoluminescence (PL) spectroscopy: Photoluminescence spectra were collected using a 785 nm narrow-band continuous wave diode laser. Photoluminescence spectra were collected in a Janis ST-100 cryostat, which was loaded in the glovebox to prevent air exposure. The laser was focused onto the sample using a 125 mm lens at ~30° from the normal, and emitted light was collected using a backscattered geometry with a 75 mm lens and sent to a Bayspec NIR spectrometer. The total power density was 0.2 W/cm^2 at the sample.

Transient absorption (TA) spectroscopy: Transient absorption spectroscopy was performed at the Advanced Optical Spectroscopy and Microscopy Facility at the Center for Functional

Nanomaterials at Brookhaven National Laboratory, as described in Section 2.9. The optical parametric amplifier (LightConversion) was used to generate IR pump pulses (1150nm, 1200nm, 1250nm, or 1350nm) with ~100 fs time resolution. A longpass filter (Thorlabs) 50nm shorter than the pump pulse wavelength (e.g. 1200nm longpass for 1250nm pump) was used to clean up the pump line to ensure it did not inadvertently excite higher energy states. The pump and probe laser pulses were cross polarized (probe is horizontally polarized, pump is vertically polarized) to reduce the noise from scattered pump light in this degenerate pump-probe experiment. The pump power to excite the trap state was 300 μW to 2.7 mW, but a significant portion of this light was scattered or transmitted through the sample because the trap state density is low and thus the absorbance at those wavelengths is low.

Transmission electron microscopy (TEM): Transmission electron microscopy (TEM) was performed on a JEOL 2011 instrument operating at 200 kV. High Resolution TEM (HRTEM) images were collected on a JEOL 2010 instrument operating at 200kV. Samples were prepared by drop casting QD suspensions in hexanes onto copper TEM grids coated with an amorphous carbon support film.

Density functional theory (DFT) calculations: The DFT calculations were performed using the Quantum ESPRESSO suite[170] with the PBE generalized gradient approximation[171] to the exchange correlation functional. Electronic wavefunctions were expanded in plane waves basis with an energy cutoff of 30 Ry. The Pb $6s^26p^2$ and S $3s^23p^6$ electrons were included in the valence, and the core-valence interaction was treated by Hartwigsen-Goedeker-Hutter norm-conserving pseudopotentials.[172] A vacuum spacing of 15 Å was added to the supercell in all three spatial directions to remove any spurious interactions. Only gamma k-point is sampled, and the atomic positions were relaxed until the residual forces were less than 0.01eV/ Å. Absorption spectra were calculated with random phase approximation using BerkeleyGW.[173]

Chapter 5 Outlook

The scope of this thesis has been to study charge carrier transport in quantum dot solids with size dispersity of less than 5%. In these ensembles, energetic disorder is limited and structural variations become the dominant source of disorder in the QD solid; spatial properties have a greater impact than energetic disorder on charge transport and determine the temperature-dependent transport properties. Additionally, the use of highly monodisperse QDs allows the identification and characterization of trap states 100-200 meV below the band edge, which are found to be caused by unintentionally created QD dimers in the solid.

The findings in this thesis point to several future directions of study. To achieve ordered, homogeneously broadened, coupled QD solids, solution phase ligand exchanges to shorter organic or inorganic ligands followed by self-assembly into ordered superlattices will be required. Recent reports on solution phase ligand exchanges are very promising,[21, 169] but these techniques will need to become more widespread. Additionally, the propensity of QDs to self-assemble into ordered superlattices may depend on the ligand length, solvent, ligand coverage, QD size and shape, and other deposition conditions, and these factors need to be better understood. Studies of self-assembly and charge transport should be integrated with synthetic development of new ligand exchange chemistries to achieve ordered QD solids with high mobilities.

In this work, we found that QD dimer trap states are formed during solid state ligand exchanges, and once in a QD solid, it will be very difficult if not impossible to remove these QD dimers. Thus, solution phase ligand exchanges also offer a pathway to eliminating these dimer trap states. It might be possible to engineer the solution phase ligand exchange process to prevent their formation by reducing the likelihood that bare QD surfaces come into contact. Alternatively, more advanced solution phase separation techniques beyond size-selective precipitation such as density gradient ultracentrifugation[174] or size exclusion chromatography,[175] may be used to separate dimers that form during solution phase ligand exchange from single QDs.

The temperature-dependent lattice distortion that drives increasing mobility with decreasing temperature was unexpected and merits further study to understand the physical processes that drive it and how universal it might be across different QD solids. For example, will a lattice distortion or contraction occur if the superlattice begins as a BCC lattice, rather than FCC, at room temperature? Also, how does the lattice distortion depend on the QD size and shape, the organic or inorganic ligand, or the solvent used during film deposition?

While this work focused on free charge carrier transport, with different ligands such as carboxylic acids, or at lower temperatures, charge carriers are expected to be excitons. If the temperature-dependent mobility is driven by a contraction in the nearest neighbor spacing, one would expect exciton mobility to also increase with decreasing temperature in PbS QD solids, but this needs to be verified. An improved understanding of temperature-dependent exciton transport will complement this thesis work and provide a more complete understanding of charge carrier transport in PbS QD solids.

We hope that this work will inspire others to develop solution phase ligand exchanges and self-assembly methods that will facilitate the fabrication of strongly coupled, homogeneously broadened, ordered quantum dot superlattices with superior transport properties that will enable further progress in quantum dot devices.

References

1. Nanotechnology Timeline. http://www.nano.gov/timeline (accessed June 14, 2017).

2. Ekimov, A. I.; Onushchenko, A. A., Quantum Size Effect in 3-Dimensional Microscopic Semiconductor Crystals. *JETP Lett.* **1981,** *34*, 345-349.

3. Ekimov, A. I.; Efros, A. L.; Onushchenko, A. A., Quantum Size Effect in Semiconductor Microcrystals. *Solid State Commun.* **1985,** *56*, 921-924.

4. Brus, L. E., Electron Electron and Electron-Hole Interactions in Small Semiconductor Crystallites - the Size Dependence of the Lowest Excited Electronic State. *J. Chem. Phys.* **1984,** *80*, 4403-4409.

5. Rossetti, R.; Hull, R.; Gibson, J. M.; Brus, L. E., Excited Electronic States and Optical-Spectra of ZnS and CdS Crystallites in the ≊ 15 to 50 Å Size Range: Evolution from Molecular to Bulk Semiconducting Properties. *J. Chem. Phys.* **1985,** *82*, 552-559.

6. Rossetti, R.; Hull, R.; Gibson, J. M.; Brus, L. E., Hybrid Electronic-Properties between the Molecular and Solid-State Limits - Lead Sulfide and Silver-Halide Crystallites. *J. Chem. Phys.* **1985,** *83*, 1406-1410.

7. Murray, C. B.; Norris, D. J.; Bawendi, M. G., Synthesis and Characterization of Nearly Monodisperse CdE (E = S, Se, Te) Semiconductor Nanocrystallites. *J. Am. Chem. Soc.* **1993,** *115*, 8706-8715.

8. Murray, C. B.; Kagan, C. R.; Bawendi, M. G., Synthesis and Characterization of Monodisperse Nanocrystals and Close-Packed Nanocrystal Assemblies. *Annu. Rev. Mater. Sci.* **2000,** *30*, 545-610.

9. Hines, M. A.; Scholes, G. D., Colloidal Pbs Nanocrystals with Size-Tunable Near-Infrared Emission: Observation of Post-Synthesis Self-Narrowing of the Particle Size Distribution. *Adv. Mater.* **2003,** *15*, 1844-1849.

10. Protesescu, L.; Yakunin, S.; Bodnarchuk, M. I.; Krieg, F.; Caputo, R.; Hendon, C. H.; Yang, R. X.; Walsh, A.; Kovalenko, M. V., Nanocrystals of Cesium Lead Halide Perovskites (CsPbX3, X = Cl, Br, and I): Novel Optoelectronic Materials Showing Bright Emission with Wide Color Gamut. *Nano Lett.* **2015,** *15*, 3692-3696.

11. Bealing, C. R.; Baumgardner, W. J.; Choi, J. J.; Hanrath, T.; Hennig, R. G., Predicting Nanocrystal Shape through Consideration of Surface-Ligand Interactions. *ACS Nano* **2012,** *6*, 2118-2127.

12. Peng, X. G.; Manna, L.; Yang, W. D.; Wickham, J.; Scher, E.; Kadavanich, A.; Alivisatos, A. P., Shape Control of CdSe Nanocrystals. *Nature* **2000,** *404*, 59-61.

13. Choi, H.; Ko, J. H.; Kim, Y. H.; Jeong, S., Steric-Hindrance-Driven Shape Transition in PbS Quantum Dots: Understanding Size-Dependent Stability. *J. Am. Chem. Soc.* **2013,** *135*, 5278-5281.

14. Zhang, H. T.; Yang, J.; Hanrath, T.; Wise, F. W., Sub-10 nm Monodisperse PbS Cubes by Post-Synthesis Shape Engineering. *Phys. Chem. Chem. Phys.* **2014,** *16*, 14640-14643.

15. Casavola, M.; van Huis, M. A.; Bals, S.; Lambert, K.; Hens, Z.; Vanmaekelbergh, D., Anisotropic Cation Exchange in PbSe/CdSe Core/Shell Nanocrystals of Different Geometry. *Chem. Mater.* **2012,** *24*, 294-302.

16. Wang, L.; Tian, Y. M.; Okuhata, T.; Tamai, N., Charge Transfer Dynamics and Auger Recombination of CdTe/CdS Core/Shell Quantum Dots. *J. Phys. Chem. C* **2015,** *119*, 17971-17978.

17. Cui, J.; Beyler, A. P.; Coropceanu, I.; Cleary, L.; Avila, T. R.; Chen, Y.; Cordero, J. M.; Heathcote, S. L.; Harris, D. K.; Chen, O.; Cao, J. S.; Bawendi, M. G., Evolution of the Single-Nanocrystal Photoluminescence Linewidth with Size and Shell: Implications for Exciton-Phonon Coupling and the Optimization of Spectral Linewidths. *Nano Lett.* **2016,** *16*, 289-296.

18. Kovalenko, M. V.; Manna, L.; Cabot, A.; Hens, Z.; Talapin, D. V.; Kagan, C. R.; Klimov, V. I.; Rogach, A. L.; Reiss, P.; Milliron, D. J.; Guyot-Sionnnest, P.; Konstantatos, G.; Parak, W. J.; Hyeon, T.; Korgel, B. A.; Murray, C. B.; Heiss, W., Prospects of Nanoscience with Nanocrystals. *ACS Nano* **2015,** *9*, 1012-1057.

19. Samsung QDLED TV. http://www.samsung.com/global/tv/qled/quantum-dot/ (accessed August 29, 2017).

20. Dai, X. L.; Deng, Y. Z.; Peng, X. G.; Jin, Y. Z., Quantum-Dot Light-Emitting Diodes for Large-Area Displays: Towards the Dawn of Commercialization. *Adv. Mater.* **2017,** *29*.

21. Liu, M. X.; Voznyy, O.; Sabatini, R.; de Arquer, F. P. G.; Munir, R.; Balawi, A. H.; Lan, X. Z.; Fan, F. J.; Walters, G.; Kirmani, A. R.; Hoogland, S.; Laquai, F.; Amassian, A.; Sargent, E. H., Hybrid Organic-Inorganic Inks Flatten the Energy Landscape in Colloidal Quantum Dot Solids. *Nat. Mater.* **2017,** *16*, 258-263.

22. Gao, J. B.; Nguyen, S. C.; Bronstein, N. D.; Alivisatos, A. P., Solution-Processed, High-Speed, and High-Quantum-Efficiency Quantum Dot Infrared Photodetectors. *ACS Photonics* **2016,** *3*, 1217-1222.

23. Sothmann, B.; Sanchez, R.; Jordan, A. N., Thermoelectric Energy Harvesting with Quantum Dots. *Nanotechnology* **2015,** *26*.

24. Bruns, O. T.; Bischof, T. S.; Harris, D. K.; Franke, D.; Shi, Y.; Riedemann, L.; Bartelt, A.; Jaworski, F. B.; Carr, J. A.; Rowlands, C. J.; Wilson, M. W. B.; Chen, O.; Wei, H.; Hwang, G. W.; Montana, D. M.; Coropceanu, I.; Achorn, O. B.; Kloepper, J.; Heeren, J.; So, P. T. C.; Fukumura, D.; Jensen, K. F.; Jain, R. K.; Bawendi, M. G., Next-Generation *in vivo* Optical Imaging with Short-Wave Infrared Quantum Dots. *Nat. Biomed. Eng.* **2017,** *1*, 0056.

25. Kovalenko, M. V.; Kaufmann, E.; Pachinger, D.; Roither, J.; Huber, M.; Stangl, J.; Hesser, G.; Schaffler, F.; Heiss, W., Colloidal HgTe Nanocrystals with Widely Tunable Narrow Band Gap Energies: From Telecommunications to Molecular Vibrations. *J. Am. Chem. Soc.* **2006,** *128*, 3516-3517.

26. Keuleyan, S.; Lhuillier, E.; Brajuskovic, V.; Guyot-Sionnest, P., Mid-Infrared HgTe Colloidal Quantum Dot Photodetectors. *Nat Photonics* **2011,** *5*, 489-493.

27. Weidman, M. C.; Beck, M. E.; Hoffman, R. S.; Prins, F.; Tisdale, W. A., Monodisperse, Air-Stable PbS Nanocrystals v*ia* Precursor Stoichiometry Control. *ACS Nano* **2014,** *8*, 6363-6371.

28. Caram, J. R.; Bertram, S. N.; Utzat, H.; Hess, W. R.; Carr, J. A.; Bischof, T. S.; Beyler, A. P.; Wilson, M. W. B.; Bawendi, M. G., PbS Nanocrystal Emission Is Governed by Multiple Emissive States. *Nano Lett.* **2016,** *16*, 6070-6077.

29. Saran, R.; Curry, R. J., Lead Sulphide Nanocrystal Photodetector Technologies. *Nat. Photonics* **2016,** *10*, 81-92.

30. Sun, L. F.; Choi, J. J.; Stachnik, D.; Bartnik, A. C.; Hyun, B. R.; Malliaras, G. G.; Hanrath, T.; Wise, F. W., Bright Infrared Quantum-Dot Light-Emitting Diodes through Inter-Dot Spacing Control. *Nat. Nanotechnol.* **2012,** *7*, 369-373.

31. Murray, C. B.; Sun, S. H.; Gaschler, W.; Doyle, H.; Betley, T. A.; Kagan, C. R., Colloidal Synthesis of Nanocrystals and Nanocrystal Superlattices. *IBM J. Res. Dev.* **2001,** *45*, 47-56.

32. Zhao, N.; Osedach, T. P.; Chang, L. Y.; Geyer, S. M.; Wanger, D.; Binda, M. T.; Arango, A. C.; Bawendi, M. G.; Bulovic, V., Colloidal PbS Quantum Dot Solar Cells with High Fill Factor. *ACS Nano* **2010,** *4*, 3743-3752.

33. Chuang, C. H. M.; Brown, P. R.; Bulovic, V.; Bawendi, M. G., Improved Performance and Stability in Quantum Dot Solar Cells through Band Alignment Engineering. *Nat. Mater.* **2014,** *13*, 796-801.

34. Bozyigit, D.; Yazdani, N.; Yarema, M.; Yarema, O.; Lin, W. M. M.; Volk, S.; Vuttivorakulchai, K.; Luisier, M.; Juranyi, F.; Wood, V., Soft Surfaces of Nanomaterials Enable Strong Phonon Interactions. *Nature* **2016,** *531*, 618-622.

35. Cademartiri, L.; Bertolotti, J.; Sapienza, R.; Wiersma, D. S.; von Freymann, G.; Ozin, G. A., Multigram Scale, Solventless, and Diffusion-Controlled Route to Highly Monodisperse PbS Nanocrystals. *J. Phys. Chem. B* **2006,** *110*, 671-673.

36. Moreels, I.; Justo, Y.; De Geyter, B.; Haustraete, K.; Martins, J. C.; Hens, Z., Size-Tunable, Bright, and Stable PbS Quantum Dots: A Surface Chemistry Study. *ACS Nano* **2011,** *5*, 2004-2012.

37. Zhang, J. B.; Gao, J. B.; Miller, E. M.; Luther, J. M.; Beard, M. C., Diffusion-Controlled Synthesis of PbS and PbSe Quantum Dots with in Situ Halide Passivation for Quantum Dot Solar Cells. *ACS Nano* **2014,** *8*, 614-622.

38. Hendricks, M. P.; Campos, M. P.; Cleveland, G. T.; Jen-La Plante, I.; Owen, J. S., A Tunable Library of Substituted Thiourea Precursors to Metal Sulfide Nanocrystals. *Science* **2015,** *348*, 1226-1230.

39. Chernomordik, B. D.; Marshall, A. R.; Pach, G. F.; Luther, J. M.; Beard, M. C., Quantum Dot Solar Cell Fabrication Protocols. *Chem. Mater.* **2017,** *29*, 189-198.

40. Zhang, C. W.; Xia, Y.; Zhang, Z. M.; Huang, Z.; Lian, L. Y.; Miao, X. S.; Zhang, D. L.; Beard, M. C.; Zhang, J. B., Combination of Cation Exchange and Quantized Ostwald Ripening for Controlling Size Distribution of Lead Chalcogenide Quantum Dots. *Chem. Mater.* **2017,** *29*, 3615-3622.

41. Kang, I.; Wise, F. W., Electronic Structure and Optical Properties of PbS and PbSe Quantum Dots. *J. Opt. Soc. Am. B: Opt. Phys.* **1997,** *14*, 1632-1646.

42. An, J. M.; Franceschetti, A.; Dudiy, S. V.; Zunger, A., The Peculiar Electronic Structure of PbSe Quantum Dots. *Nano Lett.* **2006,** *6*, 2728-2735.

43. Hyun, B. R.; Zhong, Y. W.; Bartnik, A. C.; Sun, L. F.; Abruna, H. D.; Wise, F. W.; Goodreau, J. D.; Matthews, J. R.; Leslie, T. M.; Borrelli, N. F., Electron Injection from Colloidal PbS Quantum Dots into Titanium Dioxide Nanoparticles. *ACS Nano* **2008,** *2*, 2206-2212.

44. Miller, E. M.; Kroupa, D. M.; Zhang, J. B.; Schulz, P.; Marshall, A. R.; Kahn, A.; Lany, S.; Luther, J. M.; Beard, M. C.; Perkins, C. L.; van de Lagemaat, J., Revisiting the Valence and Conduction Band Size Dependence of PbS Quantum Dot Thin Films. *ACS Nano* **2016,** *10*, 3302-3311.

45. Trinh, M. T.; Houtepen, A. J.; Schins, J. M.; Piris, J.; Siebbeles, L. D. A., Nature of the Second Optical Transition in PbSe Nanocrystals. *Nano Lett.* **2008,** *8*, 2112-2117.

46. Schins, J. M.; Trinh, M. T.; Houtepen, A. J.; Siebbeles, L. D. A., Probing Formally Forbidden Optical Transitions in PbSe Nanocrystals by Time- and Energy-Resolved Transient Absorption Spectroscopy. *Phys. Rev. B* **2009,** *80.*

47. Diaconescu, B.; Padilha, L. A.; Nagpal, P.; Swartzentruber, B. S.; Klimov, V. I., Measurement of Electronic States of PbS Nanocrystal Quantum Dots Using Scanning Tunneling Spectroscopy: The Role of Parity Selection Rules in Optical Absorption. *Phys. Rev. Lett.* **2013,** *110.*

48. Cho, B.; Peters, W. K.; Hill, R. J.; Courtney, T. L.; Jonas, D. M., Bulklike Hot Carrier Dynamics in Lead Sulfide Quantum Dots. *Nano Lett.* **2010,** *10*, 2498-2505.

49. Moreels, I.; Lambert, K.; Smeets, D.; De Muynck, D.; Nollet, T.; Martins, J. C.; Vanhaecke, F.; Vantomme, A.; Delerue, C.; Allan, G.; Hens, Z., Size-Dependent Optical Properties of Colloidal PbS Quantum Dots. *ACS Nano* **2009,** *3*, 3023-3030.

50. Weidman, M. C.; Yager, K. G.; Tisdale, W. A., Interparticle Spacing and Structural Ordering in Superlattice PbS Nanocrystal Solids Undergoing Ligand Exchange. *Chem. Mater.* **2015,** *27*, 474-482.

51. Weidman, M. C.; Smilgies, D. M.; Tisdale, W. A., Kinetics of the Self-Assembly of Nanocrystal Superlattices Measured by Real-Time in Situ X-Ray Scattering. *Nat. Mater.* **2016,** *15*, 775-781.

52. Lee, J. S.; Kovalenko, M. V.; Huang, J.; Chung, D. S.; Talapin, D. V., Band-Like Transport, High Electron Mobility and High Photoconductivity in All-Inorganic Nanocrystal Arrays. *Nat. Nanotechnol.* **2011,** *6*, 348-352.

53. Kroupa, D. M.; Voros, M.; Brawand, N. P.; McNichols, B. W.; Miller, E. M.; Gu, J.; Nozik, A. J.; Sellinger, A.; Galli, G.; Beard, M. C., Tuning Colloidal Quantum Dot Band Edge Positions through Solution-Phase Surface Chemistry Modification. *Nat. Commun.* **2017,** *8*, 15257.

54. Meulenberg, R. W.; Lee, J. R. I.; Wolcott, A.; Zhang, J. Z.; Terminello, L. J.; van Buuren, T., Determination of the Excition Binding Energy in CdSe Quantum Dots. *ACS Nano* **2009,** *3*, 325-330.

55. Zhang, J.; Toentino, J.; Smith, E. R.; Zhang, J. B.; Beard, M. C.; Nozik, A. J.; Law, M.; Johnson, J. C., Carrier Transport in PbS and PbSe QD Films Measured by Photoluminescence Quenching. *J. Phys. Chem. C* **2014,** *118*, 16228-16235.

56. Gao, J. B.; Zhang, J. B.; van de Lagemaat, J.; Johnson, J. C.; Beard, M. C., Charge Generation in PbS Quantum Dot Solar Cells Characterized by Temperature-Dependent Steady-State Photoluminescence. *ACS Nano* **2014,** *8*, 12814-12825.

57. Mork, A. J.; Weidman, M. C.; Prins, F.; Tisdale, W. A., Magnitude of the Forster Radius in Colloidal Quantum Dot Solids. *J. Phys. Chem. C* **2014,** *118*, 13920-13928.

58. Clark, S. W.; Harbold, J. M.; Wise, F. W., Resonant Energy Transfer in PbS Quantum Dots. *J. Phys. Chem. C* **2007,** *111*, 7302-7305.

59. Bose, R.; McMillan, J. F.; Gao, J.; Rickey, K. M.; Chen, C. J.; Talapin, D. V.; Murray, C. B.; Wong, C. W., Temperature-Tuning of near-Infrared Monodisperse Quantum Dot Solids at 1.5 μm for Controllable Forster Energy Transfer. *Nano Lett.* **2008,** *8*, 2006-2011.

60. Adams, D. M.; Brus, L.; Chidsey, C. E. D.; Creager, S.; Creutz, C.; Kagan, C. R.; Kamat, P. V.; Lieberman, M.; Lindsay, S.; Marcus, R. A.; Metzger, R. M.; Michel-Beyerle, M. E.; Miller, J. R.; Newton, M. D.; Rolison, D. R.; Sankey, O.; Schanze, K. S.; Yardley, J.; Zhu, X. Y., Charge Transfer on the Nanoscale: Current Status. *J. Phys. Chem. B* **2003,** *107*, 6668-6697.

61. Gao, Y. N.; Talgorn, E.; Aerts, M.; Trinh, M. T.; Schins, J. M.; Houtepen, A. J.; Siebbeles, L. D. A., Enhanced Hot-Carrier Cooling and Ultrafast Spectral Diffusion in Strongly Coupled PbSe Quantum-Dot Solids. *Nano Lett.* **2011,** *11*, 5471-5476.

62. Choi, J. J.; Luria, J.; Hyun, B. R.; Bartnik, A. C.; Sun, L. F.; Lim, Y. F.; Marohn, J. A.; Wise, F. W.; Hanrath, T., Photogenerated Exciton Dissociation in Highly Coupled Lead Salt Nanocrystal Assemblies. *Nano Lett.* **2010,** *10*, 1805-1811.

63. Efros, A. L.; Shklovskii, B. I., Coulomb Gap and Low-Temperature Conductivity of Disordered Systems. *J. Phys. C* **1975,** *8*, L49-L51.

64. Liu, H.; Pourret, A.; Guyot-Sionnest, P., Mott and Efros-Shklovskii Variable Range Hopping in CdSe Quantum Dots Films. *ACS Nano* **2010,** *4*, 5211-5216.

65. Wehrenberg, B. L.; Yu, D.; Ma, J. S.; Guyot-Sionnest, P., Conduction in Charged PbSe Nanocrystal Films. *J. Phys. Chem. B* **2005,** *109*, 20192-20199.

66. Kang, M. S.; Sahu, A.; Norris, D. J.; Frisbie, C. D., Size- and Temperature-Dependent Charge Transport in PbSe Nanocrystal Thin Films. *Nano Lett.* **2011,** *11*, 3887-3892.

67. Yu, D.; Wang, C. J.; Wehrenberg, B. L.; Guyot-Sionnest, P., Variable Range Hopping Conduction in Semiconductor Nanocrystal Solids. *Phys. Rev. Lett.* **2004,** *92*, 216802.

68. Kagan, C. R.; Murray, C. B., Charge Transport in Strongly Coupled Quantum Dot Solids. *Nat. Nanotechnol.* **2015,** *10*, 1013-1026.

69. Choi, J. H.; Fafarman, A. T.; Oh, S. J.; Ko, D. K.; Kim, D. K.; Diroll, B. T.; Muramoto, S.; Gillen, J. G.; Murray, C. B.; Kagan, C. R., Bandlike Transport in Strongly Coupled and Doped Quantum Dot Solids: A Route to High-Performance Thin-Film Electronics. *Nano Lett.* **2012,** *12*, 2631-2638.

70. Liu, Y.; Tolentino, J.; Gibbs, M.; Ihly, R.; Perkins, C. L.; Liu, Y.; Crawford, N.; Hemminger, J. C.; Law, M., PbSe Quantum Dot Field-Effect Transistors with Air-Stable Electron Mobilities above 7 $cm^2 V^{-1} s^{-1}$. *Nano Lett.* **2013,** *13*, 1578-1587.

71. Liu, Y.; Gibbs, M.; Puthussery, J.; Gaik, S.; Ihly, R.; Hillhouse, H. W.; Law, M., Dependence of Carrier Mobility on Nanocrystal Size and Ligand Length in PbSe Nanocrystal Solids. *Nano Lett.* **2010,** *10*, 1960-1969.

72. Kang, M. S.; Sahu, A.; Norris, D. J.; Frisbie, C. D., Size-Dependent Electrical Transport in CdSe Nanocrystal Thin Films. *Nano Lett.* **2010,** *10*, 3727-3732.

73. Chua, L. L.; Zaumseil, J.; Chang, J. F.; Ou, E. C. W.; Ho, P. K. H.; Sirringhaus, H.; Friend, R. H., General Observation of *n*-Type Field-Effect Behaviour in Organic Semiconductors. *Nature* **2005,** *434*, 194-199.

74. Jang, J.; Liu, W. Y.; Son, J. S.; Talapin, D. V., Temperature-Dependent Hall and Field-Effect Mobility in Strongly Coupled All-Inorganic Nanocrystal Arrays. *Nano Lett.* **2014,** *14*, 653-662.

75. Fafarman, A. T.; Koh, W. K.; Diroll, B. T.; Kim, D. K.; Ko, D. K.; Oh, S. J.; Ye, X. C.; Doan-Nguyen, V.; Crump, M. R.; Reifsnyder, D. C.; Murray, C. B.; Kagan, C. R., Thiocyanate-Capped Nanocrystal Colloids: Vibrational Reporter of Surface Chemistry and Solution-Based Route to Enhanced Coupling in Nanocrystal Solids. *J. Am. Chem. Soc.* **2011,** *133*, 15753-15761.

76. Yazdani, N.; Bozyigit, D.; Yarema, O.; Yarema, M.; Wood, V., Hole Mobility in Nanocrystal Solids as a Function of Constituent Nanocrystal Size. *J. Phys. Chem. Lett.* **2014,** *5*, 3522-3527.

77. Gao, Y. N.; Aerts, M.; Sandeep, C. S. S.; Talgorn, E.; Savenije, T. J.; Kinge, S.; Siebbeles, L. D. A.; Houtepen, A. J., Photoconductivity of PbSe Quantum-Dot Solids: Dependence on Ligand Anchor Group and Length. *ACS Nano* **2012,** *6*, 9606-9614.

78. Talgorn, E.; Gao, Y. N.; Aerts, M.; Kunneman, L. T.; Schins, J. M.; Savenije, T. J.; van Huis, M. A.; van der Zant, H. S. J.; Houtepen, A. J.; Siebbeles, L. D. A., Unity Quantum Yield of Photogenerated Charges and Band-Like Transport in Quantum-Dot Solids. *Nat. Nanotechnol.* **2011,** *6*, 733-739.

79. Guyot-Sionnest, P., Electrical Transport in Colloidal Quantum Dot Films. *J. Phys. Chem. Lett.* **2012,** *3*, 1169-1175.

80. Scheele, M., To Be or Not to Be: Band-Like Transport in Quantum Dot Solids. *Z. Phys. Chem.* **2015,** *229*, 167-178.

81. Crisp, R. W.; Schrauben, J. N.; Beard, M. C.; Luther, J. M.; Johnson, J. C., Coherent Exciton Delocalization in Strongly Coupled Quantum Dot Arrays. *Nano Lett.* **2013,** *13*, 4862-4869.

82. Turk, M. E.; Choi, J. H.; Oh, S. J.; Fafarman, A. T.; Diroll, B. T.; Murray, C. B.; Kagan, C. R.; Kikkawa, J. M., Gate-Induced Carrier Delocalization in Quantum Dot Field Effect Transistors. *Nano Lett.* **2014,** *14*, 5948-5952.

83. Whitham, K.; Yang, J.; Savitzky, B. H.; Kourkoutis, L. F.; Wise, F.; Hanrath, T., Charge Transport and Localization in Atomically Coherent Quantum Dot Solids. *Nat. Mater.* **2016,** *15*, 557-563.

84. Gao, J. B.; Johnson, J. C., Charge Trapping in Bright and Dark States of Coupled PbS Quantum Dot Films. *ACS Nano* **2012,** *6*, 3292-3303.

85. Wanger, D. D.; Correa, R. E.; Dauler, E. A.; Bawendi, M. G., The Dominant Role of Exciton Quenching in PbS Quantum-Dot-Based Photovoltaic Devices. *Nano Lett.* **2013,** *13*, 5907-5912.

86. Zhitomirsky, D.; Voznyy, O.; Hoogland, S.; Sargent, E. H., Measuring Charge Carrier Diffusion in Coupled Colloidal Quantum Dot Solids. *ACS Nano* **2013,** *7*, 5282-5290.

87. Bakulin, A. A.; Neutzner, S.; Bakker, H. J.; Ottaviani, L.; Barakel, D.; Chen, Z. Y., Charge Trapping Dynamics in PbS Colloidal Quantum Dot Photovoltaic Devices. *ACS Nano* **2013,** *7*, 8771-8779.

88. Bozyigit, D.; Volk, S.; Yarema, O.; Wood, V., Quantification of Deep Traps in Nanocrystal Solids, Their Electronic Properties, and Their Influence on Device Behavior. *Nano Lett.* **2013,** *13*, 5284-5288.

89. Mooney, J.; Krause, M. M.; Saari, J. I.; Kambhampati, P., Challenge to the Deep-Trap Model of the Surface in Semiconductor Nanocrystals. *Phys. Rev. B* **2013,** *87*, 081201.

90. Saari, J. I.; Dias, E. A.; Reifsnyder, D.; Krause, M. M.; Walsh, B. R.; Murray, C. B.; Kambhampati, P., Ultrafast Electron Trapping at the Surface of Semiconductor Nanocrystals: Excitonic and Biexcitonic Processes. *J. Phys. Chem. B* **2013,** *117*, 4412-4421.

91. Park, B.; Whitham, K.; Bian, K. F.; Lim, Y. F.; Hanrath, T., Probing Surface States in PbS Nanocrystal Films Using Pentacene Field Effect Transistors: Controlling Carrier Concentration and Charge Transport in Pentacene. *Phys. Chem. Chem. Phys.* **2014,** *16*, 25729-25733.

92. Mooney, J.; Krause, M. M.; Kambhampati, P., Connecting the Dots: The Kinetics and Thermodynamics of Hot, Cold, and Surface-Trapped Excitons in Semiconductor Nanocrystals. *J. Phys. Chem. C* **2014,** *118*, 7730-7739.

93. Bozyigit, D.; Lin, W. M. M.; Yazdani, N.; Yarema, O.; Wood, V., A Quantitative Model for Charge Carrier Transport, Trapping and Recombination in Nanocrystal-Based Solar Cells. *Nat. Commun.* **2015,** *6*, 6180.

94. Hwang, G. W.; Kim, D.; Cordero, J. M.; Wilson, M. W. B.; Chuang, C. H. M.; Grossman, J. C.; Bawendi, M. G., Identifying and Eliminating Emissive Sub-Bandgap States in Thin Films of PbS Nanocrystals. *Adv. Mater.* **2015,** *27*, 4481-4486.

95. Speirs, M. J.; Balazs, D. M.; Fang, H. H.; Lai, L. H.; Protesescu, L.; Kovalenko, M. V.; Loi, M. A., Origin of the Increased Open Circuit Voltage in PbS-CdS Core-Shell Quantum Dot Solar Cells. *J. Mater. Chem. A* **2015,** *3*, 1450-1457.

96. Nagpal, P.; Klimov, V. I., Role of Mid-Gap States in Charge Transport and Photoconductivity in Semiconductor Nanocrystal Films. *Nat. Commun.* **2011,** *2*, 486.

97. Chuang, C. H. M.; Maurano, A.; Brandt, R. E.; Hwang, G. W.; Jean, J.; Buonassisi, T.; Bulovic, V.; Bawendi, M. G., Open-Circuit Voltage Deficit, Radiative Sub-Bandgap States, and Prospects in Quantum Dot Solar Cells. *Nano Lett.* **2015,** *15*, 3286-3294.

98. Zhitomirsky, D.; Voznyy, O.; Levina, L.; Hoogland, S.; Kemp, K. W.; Ip, A. H.; Thon, S. M.; Sargent, E. H., Engineering Colloidal Quantum Dot Solids within and Beyond the Mobility-Invariant Regime. *Nat. Commun.* **2014,** *5*, 3803.

99. Zhang, Y. J.; Zherebetskyy, D.; Bronstein, N. D.; Barja, S.; Lichtenstein, L.; Schuppisser, D.; Wang, L. W.; Alivisatos, A. P.; Sameron, M., Charge Percolation Pathways Guided by Defects in Quantum Dot Solids. *Nano Lett.* **2015,** *15*, 3249-3253.

100. Erslev, P. T.; Chen, H. Y.; Gao, J. B.; Beard, M. C.; Frank, A. J.; van de Lagemaat, J.; Johnson, J. C.; Luther, J. M., Sharp Exponential Band Tails in Highly Disordered Lead Sulfide Quantum Dot Arrays. *Phys. Rev. B* **2012,** *86*, 155313.

101. Schaller, R. D.; Pietryga, J. M.; Goupalov, S. V.; Petruska, M. A.; Ivanov, S. A.; Klimov, V. I., Breaking the Phonon Bottleneck in Semiconductor Nanocrystals Via Multiphonon Emission Induced by Intrinsic Nonadiabatic Interactions. *Phys. Rev. Lett.* **2005,** *95*.

102. Trinh, M. T.; Sfeir, M. Y.; Choi, J. J.; Owen, J. S.; Zhu, X. Y., A Hot Electron-Hole Pair Breaks the Symmetry of a Semiconductor Quantum Dot. *Nano Lett.* **2013,** *13*, 6091-6097.

103. Kambhampati, P., Hot Exciton Relaxation Dynamics in Semiconductor Quantum Dots: Radiationless Transitions on the Nanoscale. *J. Phys. Chem. C* **2011,** *115*, 22089-22109.

104. Stewart, J. T.; Padilha, L. A.; Qazilbash, M. M.; Pietryga, J. M.; Midgett, A. G.; Luther, J. M.; Beard, M. C.; Nozik, A. J.; Klimov, V. I., Comparison of Carrier Multiplication Yields in PbS and PbSe Nanocrystals: The Role of Competing Energy-Loss Processes. *Nano Lett.* **2012,** *12*, 622-628.

105. Stewart, J. T.; Padilha, L. A.; Bae, W. K.; Koh, W. K.; Pietryga, J. M.; Klimov, V. I., Carrier Multiplication in Quantum Dots within the Framework of Two Competing Energy Relaxation Mechanisms. *J. Phys. Chem. Lett.* **2013,** *4*, 2061-2068.

106. Beard, M. C., Multiple Exciton Generation in Semiconductor Quantum Dots. *J. Phys. Chem. Lett.* **2011,** *2*, 1282-1288.

107. Midgett, A. G.; Hillhouse, H. W.; Hughes, B. K.; Nozik, A. J.; Beard, M. C., Flowing Versus Static Conditions for Measuring Multiple Exciton Generation in PbSe Quantum Dots. *J. Phys. Chem. C* **2010,** *114*, 17486-17500.

108. Binks, D. J., Multiple Exciton Generation in Nanocrystal Quantum Dots - Controversy, Current Status and Future Prospects. *Phys. Chem. Chem. Phys.* **2011,** *13*, 12693-12704.

109. Padilha, L. A.; Stewart, J. T.; Sandberg, R. L.; Bae, W. K.; Koh, W. K.; Pietryga, J. M.; Klimov, V. I., Carrier Multiplication in Semiconductor Nanocrystals: Influence of Size, Shape, and Composition. *Acc. Chem. Res.* **2013,** *46*, 1261-1269.

110. Klimov, V. I., Spectral and Dynamical Properties of Multilexcitons in Semiconductor Nanocrystals. *Annu. Rev. Phys. Chem.* **2007,** *58*, 635-673.

111. Kim, J. H.; Kyhm, K.; Kim, S. M.; Yang, H. S., Auger Recombination and State Filling of Resonantly Excited Ground State in CdSe Quantum Dots. *J. Appl. Phys.* **2007,** *101*.

112. Gao, Y. A.; Sandeep, C. S. S.; Schins, J. M.; Houtepen, A. J.; Siebbeles, L. D. A., Disorder Strongly Enhances Auger Recombination in Conductive Quantum-Dot Solids. *Nat. Commun.* **2013,** *4*, 2329.

113. Tessler, N.; Preezant, Y.; Rappaport, N.; Roichman, Y., Charge Transport in Disordered Organic Materials and Its Relevance to Thin-Film Devices: A Tutorial Review. *Adv. Mater.* **2009,** *21*, 2741-2761.

114. Bassler, H., Charge Transport in Disordered Organic Photoconductors - a Monte-Carlo Simulation Study. *Phys. Status Solidi B* **1993,** *175*, 15-56.

115. Lee, E. M. Y.; Tisdale, W. A.; Willard, A. P., Can Disorder Enhance Incoherent Exciton Diffusion? *J. Phys. Chem. B* **2015,** *119*, 9501-9509.

116. Akselrod, G. M.; Prins, F.; Poulikakos, L. V.; Lee, E. M. Y.; Weidman, M. C.; Mork, A. J.; Willard, A. P.; Bulovic, V.; Tisdale, W. A., Subdiffusive Exciton Transport in Quantum Dot Solids. *Nano Lett.* **2014,** *14*, 3556-3562.

117. Zhitomirsky, D.; Kramer, I. J.; Labelle, A. J.; Fischer, A.; Debnath, R.; Pan, J.; Bakr, O. M.; Sargent, E. H., Colloidal Quantum Dot Photovoltaics: The Effect of Polydispersity. *Nano Lett.* **2012,** *12*, 1007-1012.

118. Cui, J.; Beyler, A. P.; Marshall, L. F.; Chen, O.; Harris, D. K.; Wanger, D. D.; Brokmann, X.; Bawendi, M. G., Direct Probe of Spectral Inhomogeneity Reveals Synthetic Tunability of Single-Nanocrystal Spectral Linewidths. *Nat. Chem.* **2013,** *5*, 602-606.

119. Wang, R. L.; Shang, Y. Q.; Kanjanaboos, P.; Zhou, W. J.; Ning, Z. J.; Sargent, E. H., Colloidal Quantum Dot Ligand Engineering for High Performance Solar Cells. *Energy Environ. Sci.* **2016,** *9*, 1130-1143.

120. Shabaev, A.; Efros, A. L.; Efros, A. L., Dark and Photo-Conductivity in Ordered Array of Nanocrystals. *Nano Lett.* **2013,** *13*, 5454-5461.

121. Miller, A.; Abrahams, E., Impurity Conduction at Low Concentrations. *Phys. Rev.* **1960,** *120*, 745-755.

122. Lee, S.; Zhitomirsky, D.; Grossman, J. C., Manipulating Electronic Energy Disorder in Colloidal Quantum Dot Solids for Enhanced Charge Carrier Transport. *Adv. Funct. Mater.* **2016,** *26*, 1554-1562.

123. Lee, C. K.; Shi, L.; Willard, A. P., A Model of Charge-Transfer Excitons: Diffusion, Spin Dynamics, and Magnetic Field Effects. *J. Phys. Chem. Lett.* **2016,** *7*, 2246-2251.

124. Voter, A. F., Introduction to the Kinetic Monte Carlo Method. In *Radiation Effects in Solids*, Sickafus, K. E.; Kotomin, E. A.; Uberuaga, B. P., Eds.; Nato Science Series Ii 235; Springer: Dordrecht, The Netherlands, 2007; pp 1-23.

125. Park, S. D.; Baranov, D.; Ryu, J.; Cho, B.; Halder, A.; Seifert, S.; Vajda, S.; Jonas, D. M., Bandgap Inhomogeneity of a PbSe Quantum Dot Ensemble from Two-Dimensional Spectroscopy and Comparison to Size Inhomogeneity from Electron Microscopy. *Nano Lett.* **2017,** *17*, 762-771.

126. Peterson, J. J.; Krauss, T. D., Fluorescence Spectroscopy of Single Lead Sulfide Quantum Dots. *Nano Lett.* **2006,** *6*, 510-514.

127. Fernee, M. J.; Jensen, P.; Rubinsztein-Dunlop, H., Origin of the Large Homogeneous Line Widths Obtained from Strongly Quantum Confined PbS Nanocrystals at Room Temperature. *J. Phys. Chem. C* **2007,** *111*, 4984-4989.

128. Takagahara, T., Electron-Phonon Interactions and Excitonic Dephasing in Semiconductor Nanocrystals. *Phys. Rev. Lett.* **1993,** *71*, 3577-3580.

129. Kamisaka, H.; Kilina, S. V.; Yamashita, K.; Prezhdo, O. V., Ultrafast Vibrationally-Induced Dephasing of Electronic Excitations in PbSe Quantum Dot. *Nano Lett.* **2006,** *6*, 2295-2300.

130. Kagan, C. R.; Murray, C. B.; Bawendi, M. G., Long-Range Resonance Transfer of Electronic Excitations in Close-Packed CdSe Quantum-Dot Solids. *Phys. Rev. B* **1996,** *54*, 8633-8643.

131. Fernee, M. J.; Thomsen, E.; Jensen, P.; Rubinsztein-Dunlop, H., Highly Efficient Luminescence from a Hybrid State Found in Strongly Quantum Confined PbS Nanocrystals. *Nanotechnology* **2006,** *17*, 956-962.

132. Brown, P. R.; Kim, D.; Lunt, R. R.; Zhao, N.; Bawendi, M. G.; Grossman, J. C.; Bulovic, V., Energy Level Modification in Lead Sulfide Quantum Dot Thin Films through Ligand Exchange. *ACS Nano* **2014,** *8*, 5863-5872.

133. Gasser, U., Crystallization in Three- and Two-Dimensional Colloidal Suspensions. *J. Phys.: Condens. Matter* **2009,** *21*, 203101.

134. Zarghami, M. H.; Liu, Y.; Gibbs, M.; Gebremichael, E.; Webster, C.; Law, M., P-Type PbSe and PbS Quantum Dot Solids Prepared with Short-Chain Acids and Diacids. *ACS Nano* **2010,** *4*, 2475-2485.

135. Andre, A.; Zherebetskyy, D.; Hanifi, D.; He, B.; Khoshkhoo, M. S.; Jankowski, M.; Chasse, T.; Wang, L. W.; Schreiber, F.; Salleo, A.; Liu, Y.; Scheele, M., Toward Conductive Mesocrystalline Assemblies: PbS Nanocrystals Cross-Linked with Tetrathiafulvalene Dicarboxylate. *Chem. Mater.* **2015,** *27*, 8105-8115.

136. Reich, K. V.; Shklovskii, B. I., Dielectric Constant and Charging Energy in Array of Touching Nanocrystals. *Appl. Phys. Lett.* **2016,** *108*, 113104.

137. Jones, E.; Oliphant, E.; Peterson, P.; al., e. Scipy: Open Source Scientific Tools for Python. (accessed 2016-08-11).

138. Koole, R.; Allan, G.; Delerue, C.; Meijerink, A.; Vanmaekelbergh, D.; Houtepen, A. J., Optical Investigation of Quantum Confinement in PbSe Nanocrystals at Different Points in the Brillouin Zone. *Small* **2008,** *4*, 127-133.

139. Wise, F. W., Lead Salt Quantum Dots: The Limit of Strong Quantum Confinement. *Acc. Chem. Res.* **2000,** *33*, 773-780.

140. Bian, K. F.; Choi, J. J.; Kaushik, A.; Clancy, P.; Smilgies, D. M.; Hanrath, T., Shape-Anisotropy Driven Symmetry Transformations in Nanocrystal Superlattice Polymorphs. *ACS Nano* **2011,** *5*, 2815-2823.

141. Plimpton, S., Fast Parallel Algorithms for Short-Range Molecular-Dynamics. *J. Comput. Phys.* **1995,** *117*, 1-19.

142. Xu, X. M.; Yao, Y. F.; Shan, B. W.; Gu, X.; Liu, D. Q.; Liu, J. Y.; Xu, J. B.; Zhao, N.; Hu, W. P.; Miao, Q., Electron Mobility Exceeding 10 cm^2 V^{-1} s^{-1} and Band-Like Charge Transport in Solution-Processed N-Channel Organic Thin-Film Transistors. *Adv. Mater.* **2016,** *28*, 5276-5283.

143. Kafer, D.; Bashir, A.; Dou, X.; Witte, G.; Mullen, K.; Woll, C., Evidence for Band-Like Transport in Graphene-Based Organic Monolayers. *Adv. Mater.* **2010,** *22*, 384-388.

144. Cho, J.; Higashino, T.; Mori, T., Band-Like Transport Down to 20 K in Organic Single-Crystal Transistors Based on Dioctylbenzothienobenzothiophene. *Appl. Phys. Lett.* **2015,** *106*.

145. Sakanoue, T.; Sirringhaus, H., Band-Like Temperature Dependence of Mobility in a Solution-Processed Organic Semiconductor. *Nat. Mater.* **2010,** *9*, 736-740.

146. Markov, D. E.; Tanase, C.; Blom, P. W. M.; Wildeman, J., Simultaneous Enhancement of Charge Transport and Exciton Diffusion in Poly(p-Phenylene Vinylene) Derivatives. *Phys. Rev. B* **2005,** *72.*

147. Devizis, A.; Meerholz, K.; Hertel, D.; Gulbinas, V., Ultrafast Charge Carrier Mobility Dynamics in Poly(Spirobifluorene-Co-Benzothiadiazole): Influence of Temperature on Initial Transport. *Phys. Rev. B* **2010,** *82.*

148. Savenije, T. J.; Ponseca, C. S.; Kunneman, L.; Abdellah, M.; Zheng, K. B.; Tian, Y. X.; Zhu, Q. S.; Canton, S. E.; Scheblykin, I. G.; Pullerits, T.; Yartsev, A.; Sundstrom, V., Thermally Activated Exciton Dissociation and Recombination Control the Carrier Dynamics in Organometal Halide Perovskite. *J. Phys. Chem. Lett.* **2014,** *5,* 2189-2194.

149. Milot, R. L.; Eperon, G. E.; Snaith, H. J.; Johnston, M. B.; Herz, L. M., Temperature-Dependent Charge-Carrier Dynamics in $CH_3NH_3PbI_3$ Perovskite Thin Films. *Adv. Funct. Mater.* **2015,** *25,* 6218-6227.

150. Jariwala, D.; Sangwan, V. K.; Late, D. J.; Johns, J. E.; Dravid, V. P.; Marks, T. J.; Lauhon, L. J.; Hersam, M. C., Band-Like Transport in High Mobility Unencapsulated Single-Layer MoS2 Transistors. *Appl. Phys. Lett.* **2013,** *102,* 173107.

151. Gilmore, R. H.; Lee, E. M. Y.; Weidman, M. C.; Willard, A. P.; Tisdale, W. A., Charge Carrier Hopping Dynamics in Homogeneously Broadened PbS Quantum Dot Solids. *Nano Lett.* **2017,** *17,* 893-901.

152. Olkhovets, A.; Hsu, R. C.; Lipovskii, A.; Wise, F. W., Size-Dependent Temperature Variation of the Energy Gap in Lead-Salt Quantum Dots. *Phys. Rev. Lett.* **1998,** *81,* 3539-3542.

153. Claudio, G. C.; Bittner, E. R., Excitation Transfer in Aggregated and Linearly Confined Poly(p-Phenylene Vinylene) Chains. *J. Phys. Chem. A* **2003,** *107,* 7092-7100.

154. Yu, Y. X.; Guillaussier, A.; Voggu, V. R.; Pineros, W.; Truskett, T. M.; Smilgies, D. M.; Korgel, B. A., Cooling Dodecanethiol-Capped 2 nm Diameter Gold Nanocrystal Superlattices Below Room Temperature Induces a Reversible Order-Disorder Structure Transition. *J. Phys. Chem. C* **2016,** *120,* 27682-27687.

155. Dalven, R., A Review of Semiconductor Properties of PbTe, PbSe, PbS and PbO. *Infrared Phys.* **1969,** *9,* 141-184.

156. Smilgies, D. M.; Blasini, D. R., Indexation Scheme for Oriented Molecular Thin Films Studied with Grazing-Incidence Reciprocal-Space Mapping. *J. Appl. Crystallogr.* **2007,** *40,* 716-718.

157. Sandeep, C. S. S.; Azpiroz, J. M.; Evers, W. H.; Boehme, S. C.; Moreels, I.; Kinge, S.; Siebbeles, L. D. A.; Infante, I.; Houtepen, A. J., Epitaxially Connected PbSe Quantum-Dot Films: Controlled Neck Formation and Optoelectronic Properties. *ACS Nano* **2014,** *8,* 11499-11511.

158. Baumgardner, W. J.; Whitham, K.; Hanrath, T., Confined-but-Connected Quantum Solids *via* Controlled Ligand Displacement. *Nano Lett.* **2013,** *13,* 3225-3231.

159. Busch, P.; Rauscher, M.; Smilgies, D. M.; Posselt, D.; Papadakis, C. M., Grazing-Incidence Small-Angle X-Ray Scattering from Thin Polymer Films with Lamellar Structures-the Scattering Cross Section in the Distorted-Wave Born Approximation. *J. Appl. Crystallogr.* **2006,** *39,* 433-442.

160. Ip, A. H.; Thon, S. M.; Hoogland, S.; Voznyy, O.; Zhitomirsky, D.; Debnath, R.; Levina, L.; Rollny, L. R.; Carey, G. H.; Fischer, A.; Kemp, K. W.; Kramer, I. J.; Ning, Z. J.; Labelle, A. J.; Chou, K. W.; Amassian, A.; Sargent, E. H., Hybrid Passivated Colloidal Quantum Dot Solids. *Nat. Nanotechnol.* **2012,** *7,* 577-582.

161. Cademartiri, L.; Montanari, E.; Calestani, G.; Migliori, A.; Guagliardi, A.; Ozin, G. A., Size-Dependent Extinction Coefficients of PbS Quantum Dots. *J. Am. Chem. Soc.* **2006,** *128,* 10337-10346.

162. Hughes, B. K.; Blackburn, J. L.; Kroupa, D.; Shabaev, A.; Erwin, S. C.; Efros, A. L.; Nozik, A. J.; Luther, J. M.; Beard, M. C., Synthesis and Spectroscopy of PbSe Fused Quantum-Dot Dimers. *J. Am. Chem. Soc.* **2014,** *136,* 4670-4679.

163. Geuchies, J. J.; van Overbeek, C.; Evers, W. H.; Goris, B.; de Backer, A.; Gantapara, A. P.; Rabouw, F. T.; Hilhorst, J.; Peters, J. L.; Konovalov, O.; Petukhov, A. V.; Dijkstra, M.; Siebbeles, L. D. A.; van Aert, S.; Bals, S.; Vanmaekelbergh, D., In Situ Study of the Formation Mechanism of Two-Dimensional Superlattices from PbSe Nanocrystals. *Nat. Mater.* **2016,** *15,* 1248-1254.

164. Zhang, H. T.; Hu, B.; Sun, L. F.; Hovden, R.; Wise, F. W.; Muller, D. A.; Robinson, R. D., Surfactant Ligand Removal and Rational Fabrication of Inorganically Connected Quantum Dots. *Nano Lett.* **2011,** *11,* 5356-5361.

165. Choi, J. J.; Bealing, C. R.; Bian, K. F.; Hughes, K. J.; Zhang, W. Y.; Smilgies, D. M.; Hennig, R. G.; Engstrom, J. R.; Hanrath, T., Controlling Nanocrystal Superlattice Symmetry and Shape-Anisotropic Interactions through Variable Ligand Surface Coverage. *J. Am. Chem. Soc.* **2011,** *133,* 3131-3138.

166. Chen, T.; Reich, K. V.; Kramer, N. J.; Fu, H.; Kortshagen, U. R.; Shklovskii, B. I., Metal-Insulator Transition in Films of Doped Semiconductor Nanocrystals. *Nat. Mater.* **2016,** *15,* 299-303.

167. Liljeroth, P.; Overgaag, K.; Urbieta, A.; Grandider, B.; Hickey, S. G.; Vanmaekelbergh, D., Variable Orbital Coupling in a Two-Dimensional Quantum-Dot Solid Probed on a Local Scale. *Phys. Rev. Lett.* **2006,** *97,* 096803.

168. Li, H. S.; Zhitomirsky, D.; Dave, S.; Grossman, J. C., Toward the Ultimate Limit of Connectivity in Quantum Dots with High Mobility and Clean Gaps. *ACS Nano* **2016,** *10,* 606-614.

169. Lin, Q. L.; Yun, H. J.; Liu, W. Y.; Song, H. J.; Makarov, N. S.; Isaienko, O.; Nakotte, T.; Chen, G.; Luo, H. M.; Klimov, V. I.; Pietryga, J. M., Phase-Transfer Ligand Exchange of Lead Chalcogenide Quantum Dots for Direct Deposition of Thick, Highly Conductive Films. *J. Am. Chem. Soc.* **2017,** *139,* 6644-6653.

170. Giannozzi, P.; Baroni, S.; Bonini, N.; Calandra, M.; Car, R.; Cavazzoni, C.; Ceresoli, D.; Chiarotti, G. L.; Cococcioni, M.; Dabo, I.; Dal Corso, A.; de Gironcoli, S.; Fabris, S.; Fratesi, G.; Gebauer, R.; Gerstmann, U.; Gougoussis, C.; Kokalj, A.; Lazzeri, M.; Martin-Samos, L.; Marzari, N.; Mauri, F.; Mazzarello, R.; Paolini, S.; Pasquarello, A.; Paulatto, L.; Sbraccia, C.; Scandolo, S.; Sclauzero, G.; Seitsonen, A. P.; Smogunov, A.; Umari, P.; Wentzcovitch, R. M., Quantum Espresso: A Modular and Open-Source Software Project for Quantum Simulations of Materials. *J. Phys.: Condens. Matter* **2009,** *21,* 395502.

171. Perdew, J. P.; Burke, K.; Ernzerhof, M., Generalized Gradient Approximation Made Simple. *Phys. Rev. Lett.* **1996,** *77*, 3865-3868.

172. Krack, M., Pseudopotentials for H to Kr Optimized for Gradient-Corrected Exchange-Correlation Functionals. *Theor. Chem. Acc.* **2005,** *114*, 145-152.

173. Deslippe, J.; Samsonidze, G.; Strubbe, D. A.; Jain, M.; Cohen, M. L.; Louie, S. G., Berkeleygw: A Massively Parallel Computer Package for the Calculation of the Quasiparticle and Optical Properties of Materials and Nanostructures. *Comput. Phys. Commun.* **2012,** *183*, 1269-1289.

174. Xu, X. X.; Stottinger, S.; Battagliarin, G.; Hinze, G.; Mugnaioli, E.; Li, C.; Mullen, K.; Basche, T., Assembly and Separation of Semiconductor Quantum Dot Dimers and Trimers. *J. Am. Chem. Soc.* **2011,** *133*, 18062-18065.

175. Shen, Y.; Gee, M. Y.; Greytak, A. B., Purification Technologies for Colloidal Nanocrystals. *Chem. Commun.* **2017,** *53*, 827-841.